Dynamic and Geometric Control of Electronic Spins in Diamond for Quantum Sensing and Quantum Information Science

by

Junghyun Lee

B.A., B.S., University of Chicago (2011)

Submitted to the Department of Physics
in partial fulfillment of the requirements for the degree of

Doctor of Philosophy in Physics

at the

MASSACHUSETTS INSTITUTE OF TECHNOLOGY

June 2018

Author . . . .
Department of Physics
May 29, 2018

Certified by. . . . .
Ronald Walsworth
Senior Lecturer, Harvard University
Thesis Supervisor

Certified by. . . . .
Vladan Vuletic
Professor of Physics
Thesis Co-Supervisor

Accepted by . . . .
Scott A. Hughes
Professor of Physics
Interim Associate Department Head

Dynamic and Geometric Control of Electronic Spins in Diamond for Quantum Sensing and Quantum Information Science

by

Junghyun Lee

Submitted to the Department of Physics
on May 29, 2018, in partial fulfillment of the
requirements for the degree of
Doctor of Philosophy in Physics

Abstract

In recent years, the nitrogen-vacancy (NV) color center in diamond, electronic spin defects embedded in a solid-state system, has emerged as a promising platform for quantum sensing and quantum information science in ambient temperature. Its capability of robust but high-precision spin control allows the NV center to be not only a useful atomic-scale magnetic field sensor but also an attractive building block for quantum processors.

In this dissertation, I present novel schemes to dynamically and geometrically control NV spins for improved magnetic field sensing and studies of spin dynamics. First, dynamic NV phase control is synchronized with an external oscillating magnetic field, enabling single and ensemble NV AC magnetometry spectral resolution approaching sub-mHz. This protocol allows NV spins to sense an AC field spectral resolution beyond the inverse of NV spin lifetime. Also, dynamic control via dressed states of the NV spin is shown to provide effective tuning of the dipolar coupling between spins. In strongly interacting NV spin ensembles, this robust tool can be used to change the interaction dynamics. Second, geometric phase control is used to sense an external static magnetic field, improving detection sensitivity and field range. Especially, geometric phase magnetometry provides a 100-fold improvement of field range compared to conventional Ramsey magnetometry. Moreover, geometric phase control is used to observe the change of a topological state via measuring the Chern number, showing that an NV spin can serve as a tool for simple quantum simulations. Finally, I discuss the possibilities of combining the presented schemes with other quantum techniques to realize further interesting applications in future work.

Thesis Supervisor: Ronald Walsworth
Title: Senior Lecturer, Harvard University

Acknowledgments

When I reflect back my past 7 year life as a doctoral student, I realize how tremendously I was gifted to have all the people around me. Before I acknowledge people, I want to thank my external fellowship institution, ILJU foundation, for their trust in my research and financial support throughout my doctoral years.

First, I want to express sincere gratitude to my research advisor, Dr. Ronald Walsworth. Ron was a truly caring advisor who always tried to help me grow in every aspect as a successful scientist. His guidance and wisdom had a significant positive impact not just in the direction of research but also in my personal life. Even at the time when my performance was not great, he always encouraged me with all the resources that he could provide and directed me to solve the problems by myself to become an independent researcher. Without his support, none of today's achievements were possible.

I also want to thank my thesis committee members, professor Wolfgang Ketterle, Vladan Vuletic and Liang Fu. Their sincere advice not just on research directions but also on academic career path helped me to make better decisions. Especially, Wolfgang served as both academic advisor and thesis committee member, which is unusual, and I really appreciate his warmhearted guidance on everything.

I should also mention how thankful I am for Catherine Modica in MIT physics administration office. Her wholehearted care on my life as a graduate student at MIT, allowed me to overcome many obstacles that I had to face, and I am thankful for her help.

Being part of the Walsworth group was an exceptional experience, and I truly enjoyed the collaborative environment where we are always willing to help each other. I am sincerely grateful for the senior members in the group whom I worked together closely. Keigo Arai, whom I consider as my mentor, is an inspiring physicist, and was a supportive leader of the project. My skills as an experimental physicist was solidified through his guidance, and I really appreciate his mentorship. I wish we could work together again in the future. Huiliang Zhang never hesitated to provide

Lastly, I want to thank God for granting me strength to get through this journey (Philippians 4:13). His everlasting love was what made me endure all my failures, and all of the glory today belongs to him.

Citations to Previously Published Work

A large portion of Chapter 2 has been published in the following paper:

> D. R. Glenn*, D. B. Bucher*, **J. Lee**, M. D. Lukin, H. Park, R. L. Walsworth. High-resolution magnetic resonance spectroscopy using a solid-state spin sensor. *Nature*, volume **555**, pages 351-354 (2018).

A large portion of Chapter 4 has been published in the following paper:

> K. Arai*, **J. Lee***, C. Belthangady, D. R. Glenn, H. Zhang, and R. L. Walsworth. Geometric phase magnetometry using a solid-state spin. arXiv:1803.07176 (2018).

*These authors contributed equally to this work.

Contents

List of Figures

List of Tables

Chapter 1

Introduction

Coherent quantum control to initialize, manipulate, and read out the quantum state of single or multiple interacting atom systems have been studied in different types of physical systems, including ultracold atoms in optical lattices [1, 2], trapped ions [3, 4], superconducting circuits [5, 6], quantum dots [7, 8], electron donors in semiconductors [9], and spin defects in solid-state materials [10, 11]. In particular, recent studies [12, 13, 14] have shown that spin defects in solid-state materials are promising platform for quantum sensing and quantum information applications. Among different types of spin defects, the Nitrogen-Vacancy (NV) color center in diamond has many advantages in the field of quantum science due to its (i) easy optical initialization with green laser light (ii) easy control of spin states via applying resonant microwave signals and (iii) operation under ambient conditions. There has been significant contributions from NV centers to the quantum science field, ranging from quantum sensing [15, 16, 17, 18], quantum metrology [19, 20, 21] to quantum information processing [22, 23, 24].

This thesis explores novel experimental schemes to manipulate single or multiple NV center spins via dynamic and geometric phase control to achieve high-performance magnetic field sensing and important demonstrations for quantum information applications.

1.1 NV Center Basics

The NV center is one of many diamond defects [25, 26, 27] consisting of a nearest-neighbor pair of a substitutional nitrogen atom and a lattice vacancy. Depending on the relative positions of the nitrogen atom with respect to the vacancy, there are four possible crystallographic orientations within the diamond lattice. This is called the quantization axis of the spin states. The NV center exists in either of the neutral (NV^0) or negatively-charged (NV^-) states. Three nearest-neighbor carbon atoms and the nitrogen host atom provide a total of five electrons to form the NV^0 state. If the NV center captures one more electron, a total of six electrons, from another defect in the lattice, it becomes NV^- charge state, which has the useful properties discussed in this thesis.

Spin State Initialization and Readout

Under optical illumination of 532 nm, the NV center undergoes spin-state-preserving transitions between the electronic ground ($^3A_2$) and excited states (^3E), and emits fluorescence in 640 to 800 nm band with a life time of $\sim$ 13 ns. There also exists a non-radiative decay path from the $|\pm 1\rangle$ excited states to the $|0\rangle$ ground state via metastable singlet states ($^1A_1$ and ^1E) with lifetime of $\sim$ 300 ns [28, 29]. The splitting between the two metastable states is about 1043 nm (Zero Phonon Line). When a green laser continuously illuminates the diamond, the NV spin state is polarized into the $|0\rangle$ state with a probability of $\sim$ 80% or better [30]. When the NV spin is in the $|\pm 1\rangle$ ground state, we measure diminished fluorescence, and this is how we readout the spin state of the NV spin. For more detailed discussion on this topic, please see [31, 32].

Spin State Control

We find the single NV^- ground state Hamiltonian from the $^3A_2$ manifold to be

$$H_{\mathrm{NV}} = H_{\mathrm{ZFS}} + H_{\mathrm{Zeeman}} + H_{\mathrm{HF}} + H_{\mathrm{N}}, \qquad (1.1)$$
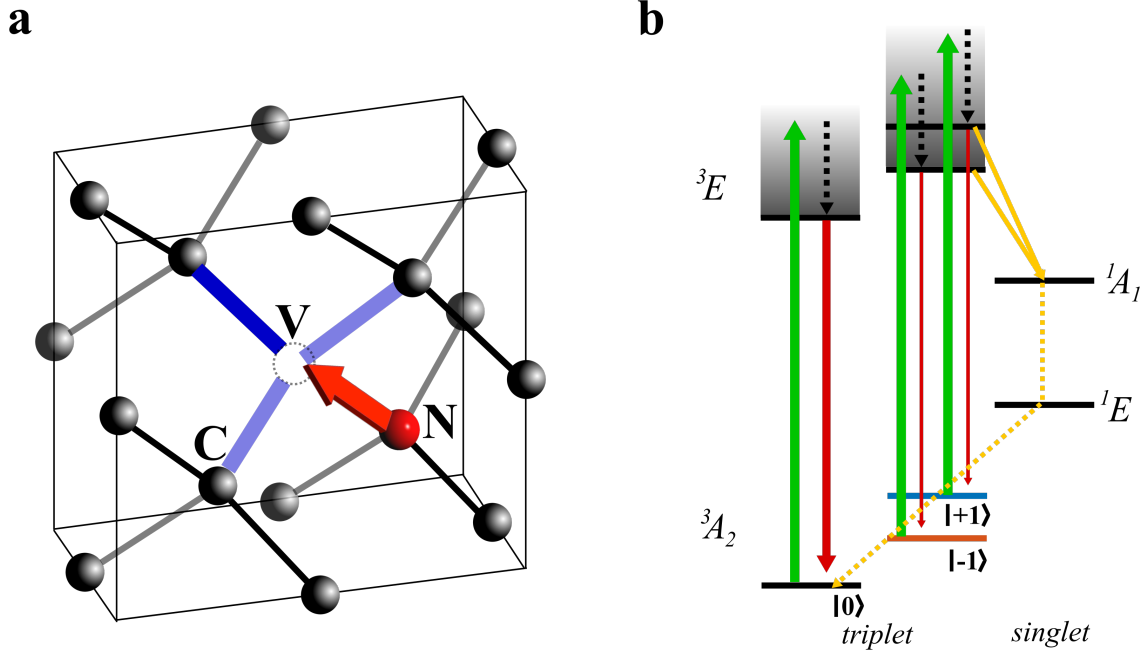
Figure 1-1: **NV spin basics. a**, The structure of diamond crystal with an NV center. NV center consists of a substitutional nitrogen atom (N) adjacent to a vacancy (V) in the diamond lattice. The direction along the nitrogen atom and the vacancy (red arrow) defines the quantization axis of the NV center. Blue rod indicates four possible orientations for different class of NV centers. **b**, NV center energy level diagram. Under optical illumination of 532 nm (green arrows), the NV center undergoes spin-state-preserving transitions between the electronic ground ($^3A_2$) and excited states (^3E), emitting fluorescence in the 640-800 nm band (red arrows) with a life time of $\sim$ 13 ns. There is also a non-radiative decay pathway (yellow arrows) from the $|0\rangle$ and $|\pm\rangle$ excited states to the $|0\rangle$ ground state via metastable singlet states (^1E and $^1A_1$) with a lifetime of $\sim$ 300 ns [28, 29]. Under continuous illumination of green laser, NV spin is eventually initialized to the $|0\rangle$ state with probability of $\sim$ 80 %. When NV spin is in $|\pm 1\rangle$ ground state, we measure diminished fluorescence, and this is how we readout the spin state of NV spin.

where H_{ZFS} is the zero-field splitting (ZFS), H_{Zeeman} is the Zeeman splitting, H_{HF} is the hyperfine interaction, and H_{N} is the quadrupole interaction. Recall that since the NV$^-$ consists of two unpaired electrons, the electronic interaction splits the energy levels into the singlet and triplet states.

Now, let us look at the each terms in above Hamiltonian. The zero-field splitting exists even in the presence of zero external magnetic field, and this comes from spin-spin interaction of NV$^-$. The negatively charged NV$^-$ state possesses six electrons, of which two unpaired electrons form a ground state spin-triplet. Due to each electron's magnetic moment, the dipole-dipole interaction causes a splitting in this triplet state [33].

$$H_{\text{ZFS}} = \hbar D \left(S_z^2 - \frac{1}{3}S(S+1) \right) + E(S_x^2 - S_y^2)) \tag{1.2}$$

where $\mathbf{S} = (S_x, S_y, S_z)$ are the Pauli spin-1 operators, $D = 2\pi \times 2.87$ GHz is the zero-field splitting, and $E \leq 10$ MHz is the strain splitting.

The Zeeman splitting comes spin subject to an external bias magnetic field, $\mathbf{B} = (B_x, B_y, B_z)$, and is written as

$$H_{\text{Zeeman}} = \hbar\gamma_e \mathbf{B} \cdot \mathbf{S} - \hbar\gamma_N \mathbf{B} \cdot \mathbf{I} \tag{1.3}$$

where $\gamma_e = 2\pi \times 2.8$ MHz/G is the gyromagnetic ratio of electron, γ_N is the gyromagnetic ratio of host nitrogen nuclear spin and $\mathbf{I} = (I_x, I_y, I_z)$ is nuclear spin vector. The hyperfine interaction of NV$^-$ electron spin and the host nitrogen nuclear spin is given as

$$H_{\text{HF}} = \hbar A_{\parallel}S_z I_z + \hbar A_{\perp}(S_x I_x + S_y I_y) \tag{1.4}$$

where $A_{\parallel}$ ($A_{\perp}$) is the axially symmetric (non-axial) hyperfine coupling parameter. For ^{14}N nuclear spin, $A_{\parallel} = 2\pi \times 2.3$ MHz and $A_{\perp} = 2\pi \times 2.1$ MHz [34, 35]. Finally,
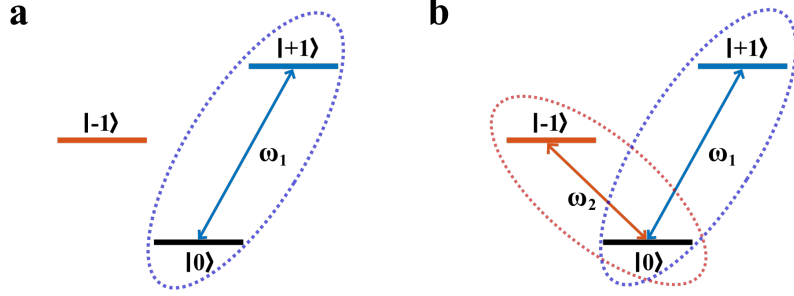
Figure 1-2: **NV spin ground state energy level. a**, $|m_s = 0\rangle$ and $|m_s = +1\rangle$ states chosen as qubit two level system, and transition of qubit state can be controlled by applying microwave with resonant frequency of ω_1. We call this Single Quantum (SQ) basis. **b**, Spin state can also be manipulated by inducing both transitions and with the basis of $|B\rangle = (|+1\rangle + |-1\rangle)/\sqrt{2}$ and $|D\rangle = (|+1\rangle - |-1\rangle)/\sqrt{2}$ states. We call this Double Quantum (DQ) basis.

the quadrupole interaction is given by

$$H_N = \hbar P \frac{1}{2} \left(3I_z^2 - I(I+1) \right) \tag{1.5}$$

where P $= 2\pi \times -5.04$ MHz is nuclear quadrupole coupling with I $= 1$ for ^{14}N nuclear spin [35]. As described in the *Prawer and Aharonovich et.al.* [36], since we align our magnetic field along the quantization axis of NV spin, we can drop some small terms and get the simplified Hamiltonian through secular approximations.

$$H_{NV}/\hbar \approx DS_z^2 + E(S_x^2 - S_y^2) + \gamma_e B_z S_z + A_{||} S_z I_z + \frac{3}{2} P I_z^2 \tag{1.6}$$

Just to focus on the dynamics of electronic spins only, let us ignore the hyperfine and quadrupole interactions for now.

When the bias field B_z is large and NV triplet sub-levels $m_s = 0$ and $m_s = \pm 1$ are split far enough, we can choose two level, transitions between $|m_s = 0\rangle$ and $|m_s = +1\rangle$ or between $|m_s = 0\rangle$ and $|m_s = -1\rangle$ as a qubit two level. With large B_z field, population leakage into unwanted state is highly suppressed. We can induce Rabi nutation between two levels by applying oscillating magnetic fields (with microwaves) with

23

resonant frequency. From now on, let us assume $\hbar = 1$.

$$H = DS_z^2 + \gamma_e B_z S_z + \Omega_1 \cos(\omega_1 t) S_x + \Omega_2 \cos(\omega_2 t) S_x \qquad (1.7)$$

where we neglected strain and hyperfine terms. $\omega_1(\omega_2)$ refers to the frequency of oscillating field and $\Omega_1(\Omega_2)$ refers to the Rabi frequency. When we operate spin manipulation between two levels (either $\Omega_1 = 0$ or $\Omega_2 = 0$), we are in Single Quantum (SQ) basis (Figure 1-1 a). We can also operate the spin control between bright state, $|B\rangle = (|+1\rangle + |-1\rangle)/\sqrt{2}$, and dark state, $|D\rangle = (|+1\rangle - |-1\rangle)/\sqrt{2}$ by applying microwaves with two different resonant frequencies of ω_1 and ω_2. We call this control scheme as Double Quantum (DQ) basis (Figure 1-1 b).

1.2 Dynamic and Geometric Phase Control Protocols

In this thesis, we introduce two different types of spin control schemes; dynamic and geometric phase control. In the rotating frame of the single quantum basis, the total Hamiltonian can be rewritten as

$$H = (\gamma_e B_z - \omega_1) S_z + \Omega_1 S_x \qquad (1.8)$$

where $(\gamma_e B_z - \omega_1)$ is the detuning, Δ, from the resonance between $|0\rangle$ and $|+1\rangle$ states, and Ω_1 is the Rabi frequency. The dynamic phase control protocol is to apply the time-independent Hamiltonian to allow the NV spin to acquire dynamic phase on the Bloch sphere, precessing around the fixed Larmor vector $\mathbf{R} = (\Omega_1, 0, \Delta)$ (Figure 1-3 a, b). Geometric phase control employs a time varying Hamiltonian, and now the Larmor vector $\mathbf{R}(t) = (\Delta, \Omega_1 \cos \phi(t), \Omega_1 \sin \phi(t))$ geometrically travels around the Hamiltonian parameter space (Figure 1-3 c).

$$H = \Delta S_z + \Omega_1 \cos \phi(t) S_x + \Omega_1 \sin \phi(t) S_y \qquad (1.9)$$

On the Bloch sphere, the NV spin will precess around the moving Larmor vector, and thus it acquires both dynamic and geometric phases. More details on geometric phase control is discussed in Chapter 4 and Chapter 5.
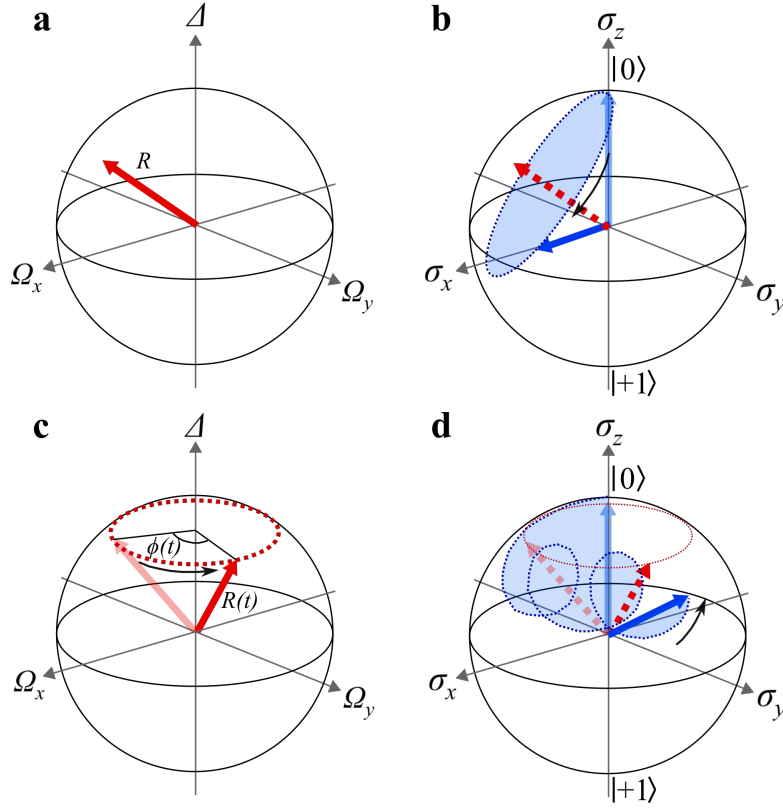
Figure 1-3: **Dynamic and geometric phase control of NV spin. a**, In Hamiltonian parameter space, which consists of detuning in z-axis, and Rabi frequencies on x and y axis, dynamic phase control refers to the control with fixed Larmor vector (red arrow) **R** in rotating frame. **b**, On the Bloch sphere, for fixed Larmor vector (dahsed red arrow), spin (blue arrow) will precess around the Larmor vector and acquire a dynamic phase. **c**, Geometric phase control refers to manipulation with a time varying Larmor vector (red arrow) **R**(t) in the rotating frame. **d**, On the Bloch sphere, for a moving Larmor vector (dahsed red arrow), the spin (blue arrow) will acquire both dynamic and geometric phase.

1.3 Thesis Outline

This thesis is divided into two parts. First, Chapter 2 and Chapter 3 use *Dynamic phase control* of NV spins to address the problem of poor spectral resolution in NV AC magnetometry and to introduce a novel scheme to control the dipolar coupling between spins. Second, Chapter 4 and Chapter 5 use *Geometric phase control* of NV spins to address the problem of poor sensitivity and detectable magnetic field range in NV DC magnetometry, and to introduce simple quantum simulation of topological transition using a single qubit.

Chapter 2 introduces the Synchronized Readout method [37], which is a new approach to to coherently or incoherently sense external oscillating magnetic signals for an arbitrary duration, not limited by the finite coherence time of an NV spin, and to demonstrate single NV and ensemble NV detection of a coil-produced artificial AC signal with high spectral resolution (millihertz).

Chapter 3 presents a novel scheme to control the effective dipolar coupling strength between spins. As a proof-of-principle demonstration, we use two strongly coupled NV spins with different quantization axes as a test bed of this scheme. We use Ramsey spectroscopy to observe the change of coupling dynamics by dressing one of the spins into a different types of basis.

Chapter 4 introduces a new way to do DC magnetometry through the measurement of geometric phase evolution. Unlike conventional NV Ramsey magnetometry, where the detectable field range is inversely proportional to the sensitivity, geometric phase magnetometry shows that we can decouple sensitivity and field range, and achieve arbitrarily large field range with high sensitivity. We also measure the NV geometric phase coherence time, which turns out to depend on how fast we control the Larmor vector. Finally, in the non-adiabatic control regime, we observe NV magnetometry sensitivity surpassing the sensitivity of typical Ramsey magnetometry.

Chapter 5 presents a simple quantum simulation using a single NV qubit to measure a topological transition. A topologically invariant number, the Chern number, is measured by varying the topology of the system. Taking advantage of a lifted degen-

eracy due to hyperfine interactions, we show that with a single qubit, measurement of topological phase dynamics of three interacting qubit system becomes possible.

Finally, Chapter 6 discusses further directions of measurements, which can be made to achieve better quantum sensing and quantum information applications.

Chapter 2

High-Resolution Magnetic Resonance Spectroscopy

2.1 Introduction

In recent years, nano-scale nuclear magnetic resonance (NMR) sensing using a single NV center [38, 39, 40] has been successfully demonstrated. These results have opened up a possibility of a single molecule NMR for its chemical structural studies or multi-nuclear spin spectroscopy for quantum information science [41]. However, to date, there is a key challenge, which limited the spectral resolution of NMR detection using NV centers; the interrogation duration for NV-NMR detection technique has been limited by the spin state lifetime of the NV ($T_1 \sim 3$ ms), which is orders of magnitude shorter than the coherence times of nuclear spins in bulk liquid samples ($T_2 \sim 1$ s) or intrinsic to diamond such as ^{13}C nuclear spins. Recent studies have shown that quantum memory techniques can significantly extend the NV spin lifetime [42, 43]. However, such techniques have unfavorable sensitivity (η) scaling with spectral resolution (δf), $\eta \sim (\delta f)^{-1/2}$, because the NV probe must be in a non-interacting state while the memory is active [44]. In this chapter, we present a new scheme called Synchronized Readout (SR) protocol to Coherently or Incoherently sense external oscillating magnetic signal.

Using quantum lock-in detection, this scheme allows quantum sensing with ar-
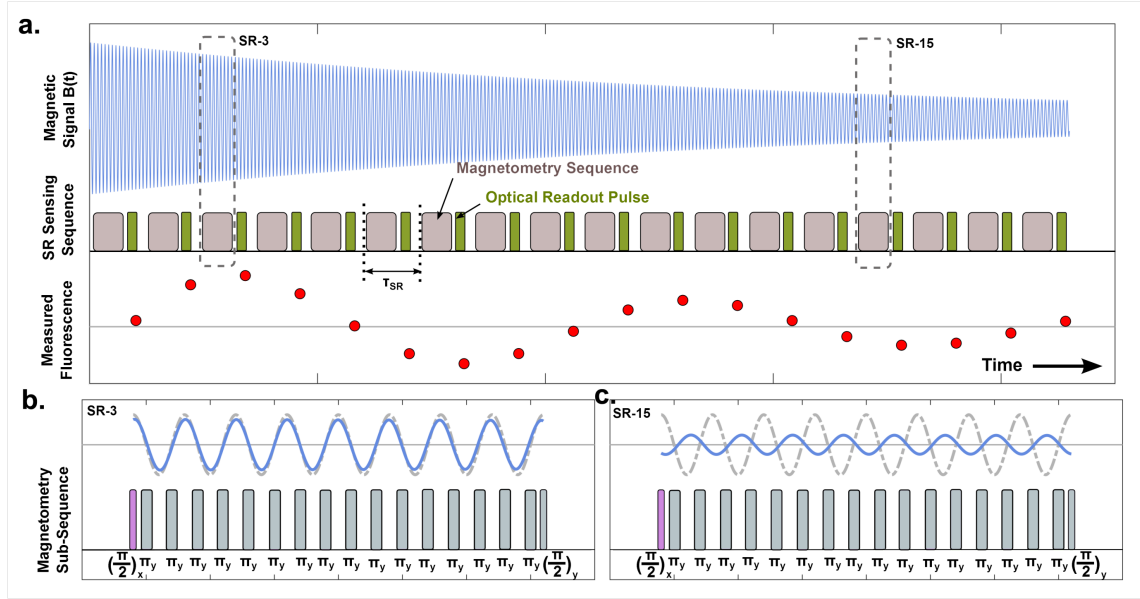
Figure 2-1: **Principle of Synchronized Readout (SR) protocol**. **(a)**, Numerical simulation of SR detection of a free induction decay (FID) signal, $B(t)$ (blue), which oscillates at frequency f and has finite decay lifetime τ. The SR sequence consists of interspersed blocks of identical NV magnetometry sub-sequences (gray boxes) and optical NV spin state readouts (green boxes). Using magnetometry sub-sequences with maximum response at frequency f_0, the duration τ_{SR} of each SR iteration is chosen to be $\tau_{SR} = \mathrm{k}/f_0$, for integer k. The NV fluorescence time series over successive SR readouts oscillates at frequency $\delta f = f - f_0$, because the FID signal phase advances incrementally relative to the magnetometry sub-sequence. **(b)**, Detail of calculated magnetic signal and magnetometry subsequence at the third SR iteration (denoted SR-3). The signal (blue line) is nearly in phase with a sinusoid at f_0 (gray dashed line). The magnetometry subsequence (here implemented as an CPMG8-2 dynamical decoupling sequence) consists of a series of π-pulses timed to coincide with the zero-crossings of the sinusoid at f_0, resulting in a detected fluoresce maximum because the FID is in phase. **(c)**, Detail of magnetic signal and magnetometry subsequence at SR-15. The signal (blue line) has advanced and is now $\sim$180 degree out of phase with the sinusoid at the central frequency (gray dashed line). This gives rise to a detected fluorescence minimum at SR-15

bitrary duration beyond the lifetime of qubit probe, and gives single NV-detected artificial signal with spectral resolution approaching ~ 3 mHz. Furthermore, by increasing the sensor spin volume size, which gives higher magnetic field sensitivity with improved signal-to-noise ratio, we measure ensemble NV detected water NMR signal with spectral resolution approaching to ~ 1 Hz.

2.2 Synchronized Readout Measurement

2.2.1 Concept of Synchronized Readout Protocol

The idea of the synchronized readout (SR) NMR signal detection protocol is based on signal mixing between an external oscillating magnetic field - nuclear Larmor oscillation signal or other AC magnetic signal - and periodic readout of sensor spin magnetometry response, all synchronized to an external clock. Each block of sensor spin response readout consists of an NV AC magnetometry pulse sequence and optical readout/initialization pulses. This block of identical pulse sequence is equidistantly positioned with the frequency of f_0. (Here, f_0 is the center frequency of the AC magnetometry spectral response function see below for details.) Given that the external oscillating magnetic field has frequency of f_{ac}, if $f_{ac} = f_0$, then the NV fluorescence readout from each block will have the same signal amplitude. However, if $f_{ac} \neq f_0$, then the NV fluorescence signal will oscillate at $\Delta f = |f_{ac} - f_0|$ (Figure 2-1). For the maximum contrast in SR NV fluorescence signal oscillation, NV AC magnetometry pulse is tuned with the external oscillating magnetic field frequency f_{ac}.

2.2.2 AC Sine Magnetometry for Synchronized Readout

NV AC-magnetometry is performed by using a dynamical decoupling pulse sequence such as CPMG (Carr-Purcell-Meiboom-Gill) pulse sequence or XY pulse sequence (Figure 2-2). These dynamical decoupling sequences consist of equally spaced consecutive pulses, providing an AC signal filter, which makes spin only to accumulate
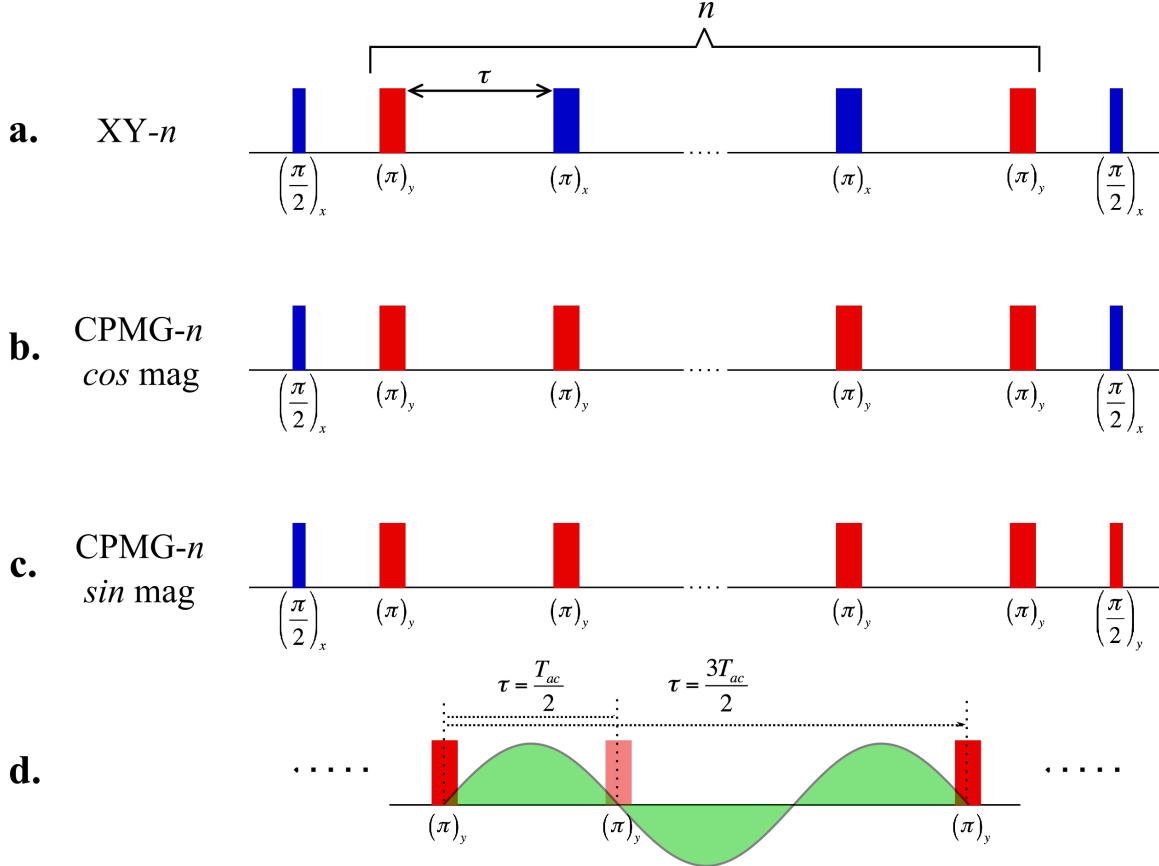
Figure 2-2: **Pulse diagrams of different types of dynamical decoupling sequences.** **(a)** n-pulse XY, **(b)** n-pulse CPMG with same phase for initial $\pi/2$ and final $\pi/2$ pulses, which is called cosine magnetometry pulse sequence and **(c)** n-pulse CPMG with 90 degree phase shift on a final $\pi/2$ pulse, compared to an initial $\pi/2$ pulse, which is called sine magnetometry pulse sequence. **(d)** For the dynamical decoupling schemes with periodic pulse spacing, the optimal time spacing $\tau = (2n + 1)T_{ac}/2$ to sense AC magnetic field of frequency $f_{ac} = 1/(2T_{ac})$ (green) is shown.

net phase at a specific AC signal frequency. In this work, for demonstrating SR measurement on a single NV center, we used CPMG-n pulse sequence as a basic building block for the SR pulse train. n-pulse CPMG sequence is widely used in the field of NMR [45, 46], and it is just an extension of Hahn-echo sequence where there are n-repeated, equally spaced refocusing π pulses between two Hadamard gate rotation, $\pi/2$ pulses, which prepares NV spin into superposition state between $|m_s = 0\rangle$ and $|m_s = -1\rangle$ or $|m_s = +1\rangle$. Moreover, by modulating the phase of the MW signal, the spin rotation axis of π pulse train is chosen to be 90 degree rotated from the first $\pi/2$

pulse. (Figure 2-1 c) shows CPMG pulse sequence where the $\pi/2$ pulse is around the x-axis and the π pulses are around the y-axis. Switching rotation axis by 90 degree and having an even number of π pulses can compensate possible pulses errors, which could accumulate along one spin rotation axis. This makes CPMG pulse sequence one of the most robust AC-magnetometry pulse sequences. Depending on the phase of the last $\pi/2$ pulse, there are two types of AC-magnetometry protocols; when the last $\pi/2$ pulse has the same phase as the initial $\pi/2$ pulse, it is called AC cosine magnetometry and when the last $\pi/2$ pulse has 90 degree out of phase from the initial $\pi/2$ pulse, it is called AC sine magnetometry. Each magnetometry protocol has different response to an external AC magnetic field. When the nuclear Larmor frequency, or an external AC signal matches the center frequency of the AC-magnetometry pulse sequence, $f_{ac} = f_0$, the coherent component of the signal is constant in time over periodic NV readouts, while the noise component is slowly time-varying on timescale τ_c, the correlation time of the nuclear spin bath. In Synchronized Readout measurements, AC sine magnetometry protocol is chosen, such that the final NV spin population is *linearly* dependent on the amplitude of the total oscillating magnetic field signal. This is a key difference from previous NV-detected NMR protocols, where AC cosine magnetometry pulse sequences have a *quadratic* dependence of the final NV spin population on the magnetic field signal in order to rectify the zero-mean noise component and sense its variance. Because we do not carry out this rectification step, the mean amplitude of the noise component in our fluorescence signal is zero, and its standard deviation increases only as the square root of the number of NV fluorescence readouts. Moreover, the amplitude of the coherent component in the fluorescence signal increases linearly with the number of NV readouts. Therefore, over many synchronized readout cycles, the measurement is sensitive primarily to the coherent component of the signal, and insensitive to the noise component.
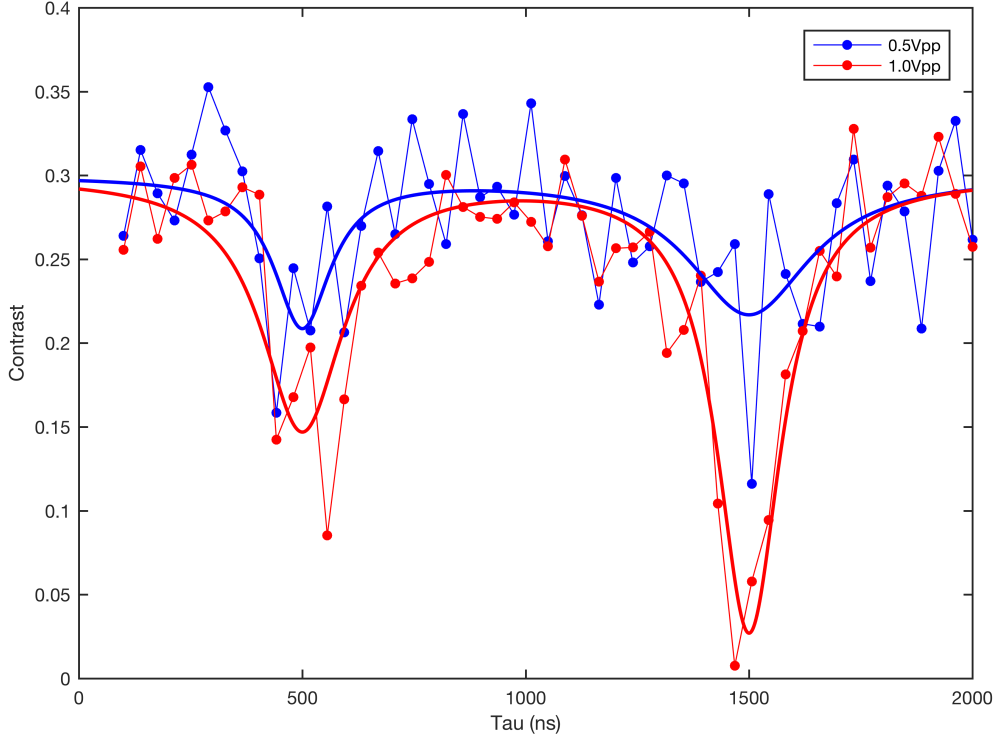
Figure 2-3: **AC Sine magnetometry using a CPMG-8 sequence**. When an external oscillating signal of $f_{ac} = 1$ MHz ($T_{ac} = 1$ μs) is applied. τ, the spacing between π pulses, is swept from 100 ns to 2 μs with steps of 40 ns. We can observe that when $\tau = (2n+1)T_{ac}/2$, the NV loses its fluorescence due to the phase accumulation caused by a coherent external AC signal.

NV Diamond Sample

For all single NV measurements, we used low NV density diamond chip. The diamond was a 4mm×4mm×0.5mm high-purity CVD diamond chip, with 99.99% ^{12}C isotopic purity near the surface, which contained preferentially oriented NV centers with nitrogen concentration $[^{14}N] \approx 1\times10^{15}$cm^{-3} and NV concentration $[NV] \approx 3\times10^{12}$cm^{-3}. The approximate coherence times for the single NV center used in our experiments were $T_1 \approx 1$ ms, $T_2 \approx 500$ μs, and $T_2^* \approx 50$ μs.

AC Sine Magnetometry Measurement

First, AC sine magnetometry was performed using a simple block of CPMG-8 pulse sequences. All π and $\pi/2$ pulse durations are determined by using 10 MHz Rabi nutation. While an oscillating coherent magnetic field, $b(t) = b_{ac}\sin(2\pi f_{ac} + \phi)$, with frequency f_{ac} (period $T_{ac} = 1/f_{ac}$) is applied using a coil antenna, the free precession time between π pulses in CPMG pulse sequence, τ, is varied to detect that oscillating magnetic field. Once τ matches to $T_{ac}/2$, in which π pulses are placed at every zeros of $b(t)$ field, at each τ duration, NV spin gains phase due to external $b(t)$ field. This phase is accumulated throughout whole CPMG pulse sequence as NV spin is flipped by π pulses whenever $b(t)$ field flips its sign. This appears as dips in spin coherence plots (Figure 2-3). Furthermore, phase accumulation happens in the following harmonics,

$$\tau = \frac{(2n+1)}{2} T_{ac} \tag{2.1}$$

where n = 0 yields the first phase accumulation time and n = 2 yields the second.

2.3 Synchronized Readout with Single NV spin

2.3.1 Coherently Averaged Synchronized Readout (CASR)

Synchronized readout consists of concatenated NV magnetometry pulse sequences, interspersed with projective NV spin state readouts and initialization pulses, all synchronized to an external clock. This makes SR protocol to be a quantum lock-in measurement, where the qubit probe is periodically active on sensing an external field. When the oscillating external magnetic fields initial phase is locked to SR sequence, we can coherently average the signal, which we call Coherently Averaged Synchronized Readout (CASR).

As a proof-of-principle demonstration of CASR, we used CPMG-8 magnetometry sub-sequences with $\tau = 0.5$ μs, which set the center frequency of SR measurement, $f_0 = 1/(2\tau) = 1$ MHz; single cycle period was $\tau_{SR} = 15$ μs and the total experiment duration was $T = N\tau_{SR} = 0.03$ s, for $N = 2000$, where N is a number of readouts. The coil antenna-generated external AC signal frequency was set to $f_{ac} = 999$ kHz, and phase of an external AC signal was locked to the first CPMG-8 sub-sequence so that the SR signal can be coherently time averaged over the repeated measurements. To achieve reasonably good signal-to-noise ratio (SNR > 3), we coherently averaged over 5×10^5 times. From the CASR measurement result (Figure 2-4), we can observe coherent oscillations, and the discrete Fourier transform of the CASR signal (inset Figure 2-4) reveals harmonics of beating signal, which appears at

$$\Delta f_h = (2n+1)\Delta f = (2n+1)|f_0 - f_{ac}| \tag{2.2}$$

,where Δf is the first order beating. Higher harmonics are due to a strong AC signal amplitude, by which NV spin accumulates more than $\pi/2$ phase during each CPMG subsequence. More details on calculating phase accumulation are presented in a later section. Importantly, we observed the full width half maximum (FWHM) linewidth of 33 ± 2 Hz (uncertainty from the fit) from the FFT signal, which will further improved by extending the total length of SR sequence.
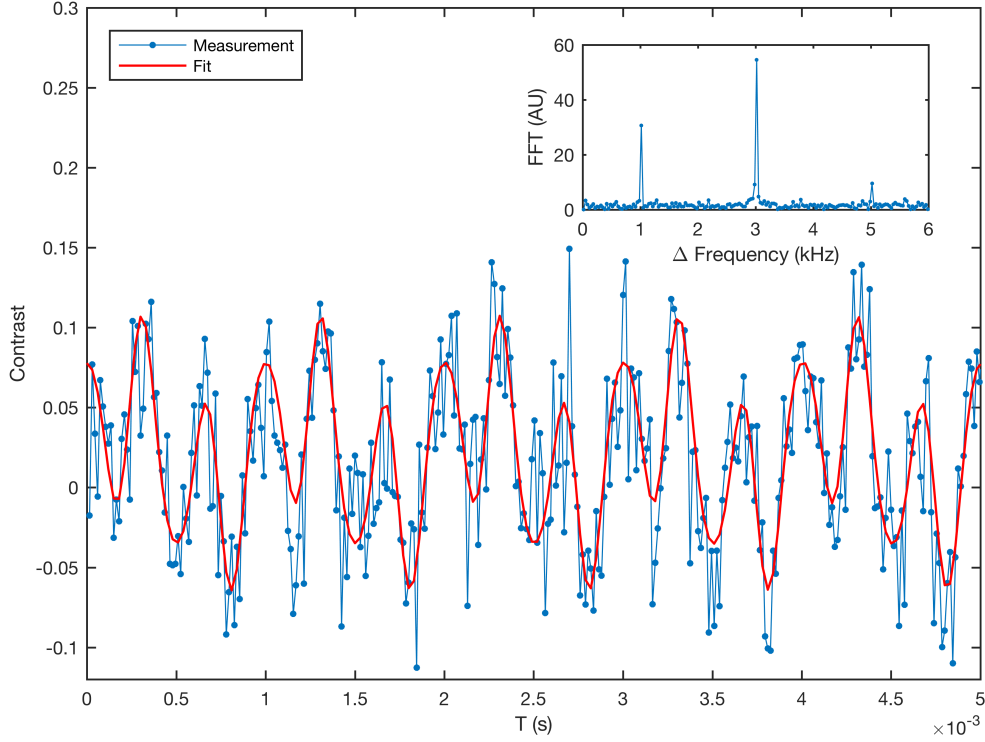
Figure 2-4: **Coherently Averaged Synchronized Readout (CASR) time-series signal of a single NV sensor**. Here, we used CPMG-8 as a magnetometry subsequence with $\tau = 0.5$ μs, which is a frequency of $f_0 = 1$ MHz. Total length of single block measurement was set to $\tau_{SR} = 15$ μs, and a single CASR consisted of 2000 blocks of measurements with duration of $T = 0.03$ s. External AC signal of $f_{ac} = 999$ kHz was applied, and for each CASR measurement, initial phase of AC signal was locked to 0. The time series data was measured by averaging over 5×10^5 times. Inset figure indicates FFT of the time series signal, which shows peaks at expected positions where $\Delta f = |f_{ac} - f_0|$. Higher harmonics are due to strong AC signal amplitude.
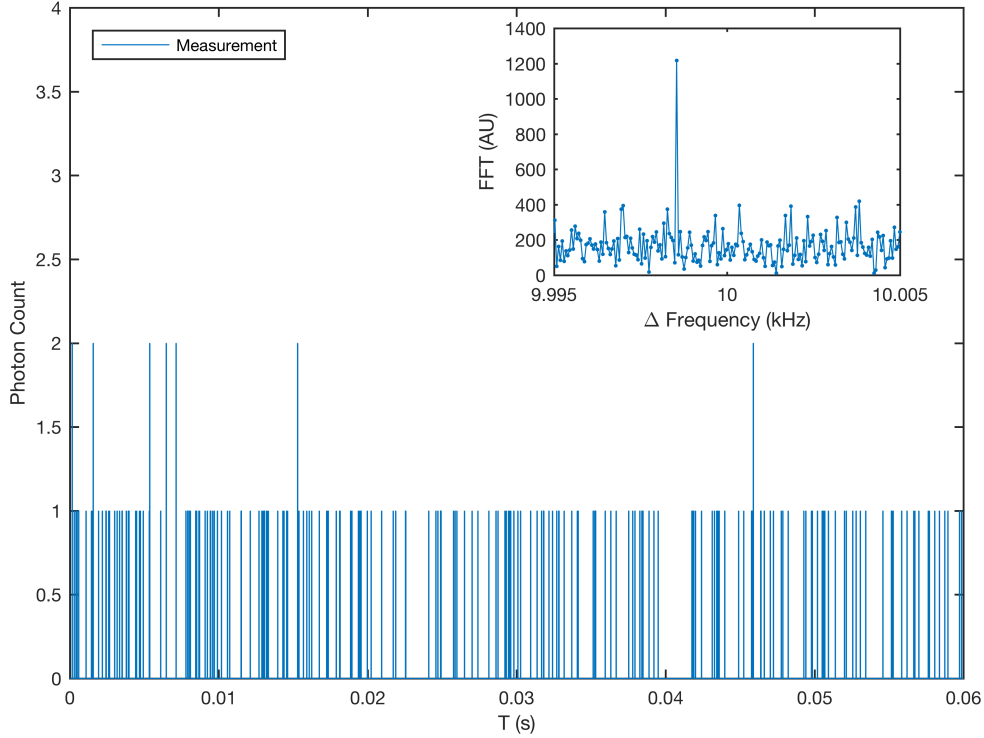
Figure 2-5: **Incoherently Averaged Synchronized Readout (IASR) time-series signal of a single NV sensor**. Again, we used CPMG-8 as a magnetometry subsequence with $\tau = 0.5$ μs, which is a frequency of $f_0 = 1$ MHz. Length of a single block measurement was set to $\tau_{SR} = 15$ μs, and a single IASR consisted of 1.25×10^6 blocks of measurements with duration of $T = 18.75$ s. External AC signal of $f_{ac} = 990$ kHz was applied, and for each IASR measurement, initial phase of AC signal was set to random. The time series data was only measured once. Inset figure indicates FFT of this time series signal, which shows peaks at expected positions where $\Delta f = |f_{ac} - f_0| = 10$ kHz.

2.3.2 Incoherently Averaged Synchronized Readout (IASR)

Synchronized readout (SR) protocol is applicable to sensors of any size, and does not require coherent averaging. In particular, synchronized readout may be applied to signals with random phase, providing spectral resolution proportional to the inverse correlation time of the signal τ_c^{-1}, by incoherent averaging using periodogram techniques [47], which we call Incoherently Averaged Synchronized Readout (IASR) scheme. As a proof-of-principle demonstration of IASR, we used CPMG-8 magnetometry sub-sequences with $\tau = 0.5$ μs, which set the central frequency of SR mea-

surement, $f_0 = 1/(2\tau) = 1$ MHz; single cycle period was $\tau_{SR} = 15$ μs and the total experiment duration was $T = N\tau_{SR} = 18.75$ s, for $N = 1250000$, where N is a number of readouts. Large number for N was chosen to have single measurement SNR to be larger than 1. In IASR measurement, coil antenna was excited continuously (without gating or triggering of the sources) to produce a magnetic signal of $f_{ac} = 990$ kHz and initial phase was set to be random.

Figure 2-4 shows typical time series data for a single set of IASR measurement (with no averaging). Because of finite optical collection efficiency for a single NV spin, each fluorescence readout detected only a mean of 0.03 photon, which degrades the SNR of each IASR measurement. Despite its randomly dispersed time series data, discrete Fourier transform reveals clear peak at around $\Delta f = |f_{ac} - f_0| = 10$ kHz, where f_{ac} is frequency of oscillating magnetic field and f_0 is SR protocol readout frequency (inset Figure 2-4). FWHM linewidth of observed FFT signal is 53 mHz, which is sufficient to resolve an oscillating field frequency within the precision of sub 100 mHz.

To confirm that IASR spectral resolution can be improved further down to ~ 1 mHz level, we extended total length of IASR sequence and measured the signal response. Detecting an external AC signal via IASR, spectral resolution should only be limited by the total length of entire pulse block, or the stability of an external clock. Change of spectral resolution by varying total time of SR sequence, T is shown in Figure 2-6. As T is increased, improved spectral resolution of the IASR signal is clearly observed. For $T = 225$ s, measured spectral resolution is reaching the Fourier limit ~ 3.7 mHz (FWHM).

Finally, to mimic NMR signal with chemical shifts, the coil antenna was excited continuously to produce a magnetic signal consisting of three closely-spaced frequencies around 3.7325 MHz. We tuned the antenna-generated signal strength such that magnetic field amplitude at the NV sensor was ~ 3 μT, corresponding to maximum fluorescence contrast for a single CPMG-32 sequence. Cycle period was chosen as $\tau_{SR} = 75.04$ μs with SR protocol central frequency $f_0 = 3.7313$ MHz; and the total SR sequence duration was $T = N\tau_{SR} = 112.5$ s, for $N = 1.5 \times 10^6$. To overcome
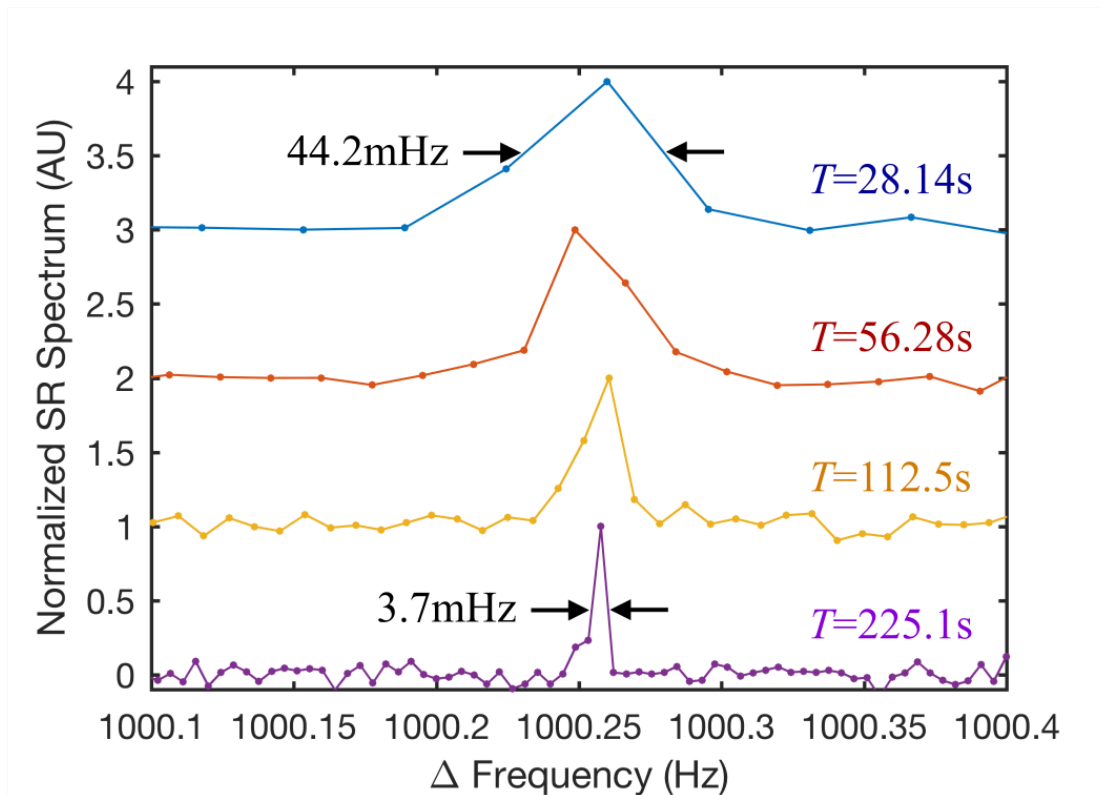
Figure 2-6: **IASR signal by increasing** T. Improved spectral resolution of an external AC signal measured via IASR by increasing total length of SR measurement T. At $T = 225.1$ s, we measure FWHM of 3.7 mHz.
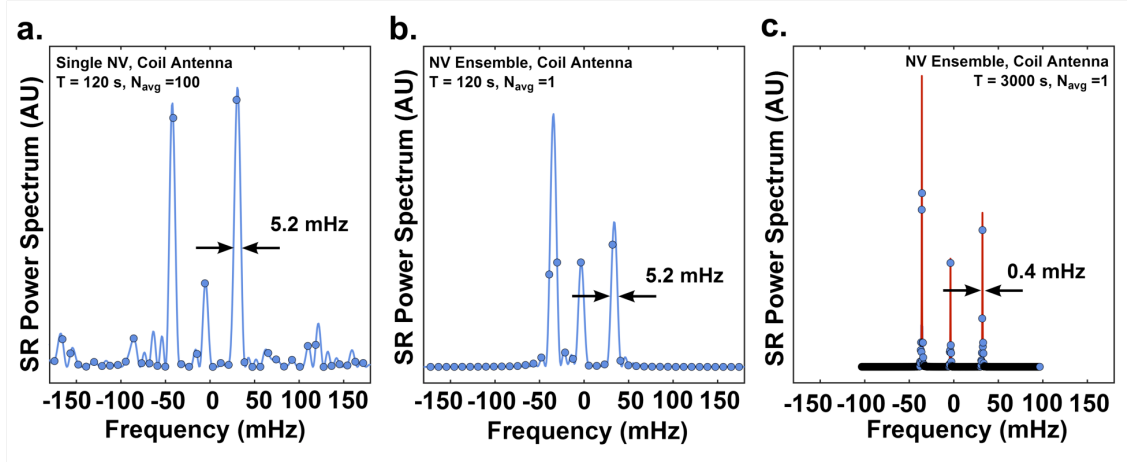
Figure 2-7: **SR spectral resolution measured using signals from a coil antenna**. **(a)** Power spectrum of IASR signal obtained with a single-NV magnetic sensor in a confocal microscope. The SR protocol used iteration time $\tau_{SR} = 75$ μs, and the total experiment duration was $T = N\tau_{SR} = 112.5$ s, for $N = 1.5 \times 10^6$ iterations. Data shown are the average of 100 experiments. The observed spectral width was 5.2 mHz (FWHM). Independent, spectrally narrow signal sources were used to drive each of the three detected frequencies. **(b)** Power spectrum of SR signal obtained with an NV ensemble magnetic sensor. The SR protocol used iteration time $\tau_{SR} = 75$ μs, and the total experiment duration was $T = N\tau_{SR} = 112.5$ s, for $N = 1.5 \times 10^6$ iterations. The spectrum shown is for a single average. The observed spectral width was again 5.2 mHz (FWHM). **(c)** Power spectrum of SR signal obtained with an NV ensemble magnetic sensor. The SR protocol used iteration time $\tau_{SR} = 1.2$ ms, and the total experiment duration was $T = N\tau_{SR} = 3000$ s, for $N = 2.5 \times 10^6$ iterations. The observed spectral width was 0.4 mHz (FWHM), substantially broader than the Fourier limit. The measured linewidths for the three signals were consistent to within 10%, suggesting that the spectral resolution in this measurement was limited by the stability of the timing source used to control the SR protocol.

poor single measurement SNR due to finite optical collection efficiency, SR protocol was repeated 100 times, and a Bartlett periodogram (converting time domain into frequency domain, and averaged frequency power spectrum over multiple sets of measurements) from the full data set was constructed. In the resulting power spectrum (Figure 2-7 a), the three signal peaks were clearly distinguishable, with spectral resolution of 5.2 mHz (FWHM). The averages in this experiment were *incoherent*, in that the phase of the detected signal relative to the start of the first magnetometry sub-sequence was randomized every average. Such an incoherent averaging procedure could, in principle, be used for noise spectroscopy of a statistically-polarized nuclear spin ensemble, with the synchronized readout measurement duration matched to the noise correlation time $n\tau_{SR} \approx \tau_c$.

2.3.3 Sensitivity Estimation using IASR

To measure the sensitivity of a single NV magnetometer using the IASR protocol, we performed a calibration in two steps: (i) We first determined the amplitude of an oscillating magnetic field, applied with a nearby coil antenna, using known physical properties of the NV sensor. (ii) We then used that calibration to apply a weak oscillating field of known amplitude, detected it using the SR protocol, and observed the signal-to-noise ratio (SNR) as a function of averaging time. First, the magnitude of an applied oscillating magnetic field is varied by,

$$b(t) = b_{ac}\sin(2\pi f_{ac} + \phi_R) \tag{2.3}$$

,where b_{ac} is field amplitude which requires to be calibrated; $f_{ac} = 3.7325$ MHz is the drive frequency on the coil antenna, which is within a few kHz away from the central magnetometry frequency f_0; ϕ_R is a fixed random phase with respect to the first NV AC-magnetometry sub-sequence. SR time series signal is recorded by varying the AC current supplied to the coil antenna. Instead of current, here it is parameterized with control voltage V_c to set the output of the current supply, where b_{ac} is linearly proportional to V_c.
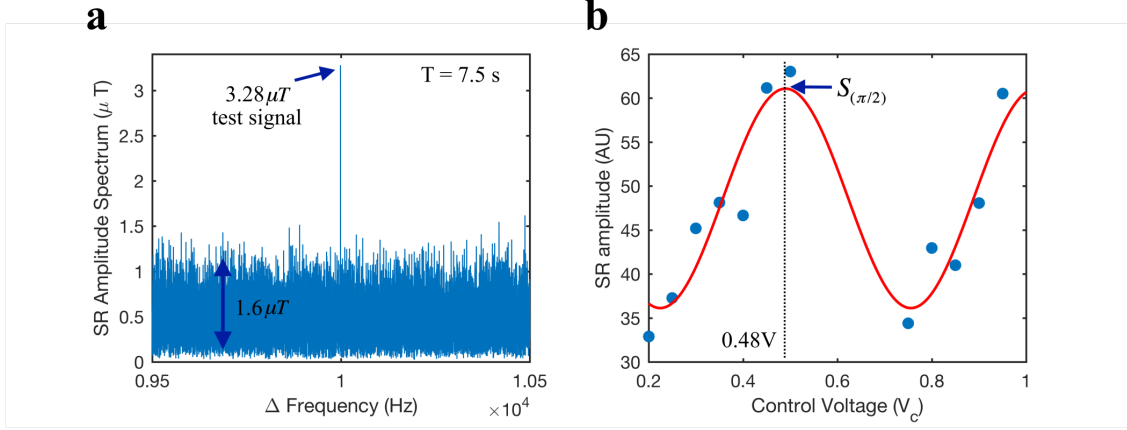
Figure 2-8: **Sensitivity of a single NV sensor**. **(a)** Incoherently averaged synchronized readout amplitude spectrum of a 3.28 μT test signal ($f_{coil} = 3.7325$ MHz), recorded in 7.5 s. The calibrated signal amplitude defines the vertical axis of the plot. The noise amplitude is determined by comparison with the calibrated test signal. **(b)** Synchronized readout FFT amplitude data (blue points) as a function of control voltage V_c. Red line is a sine-function fit to the data, from which we obtain the control voltage, $V_c = 0.48$ V that produces a $\pi/2$ NV phase accumulation in a single magnetometry sub-sequence. This provides a calibration for the amplitude of the applied test signal.

The value of b_{ac} can be calculated directly from the FFT of SR time series data, using the NV magnetic moment and timing properties of magnetometry sub-sequences. For an oscillating magnetic field of frequency f_{ac}, SR signal will be oscillating with beating frequency $\Delta f = |f_{ac} - f_0|$, and its oscillation amplitude appears as amplitude of FFT with linear dependence. Therefore, FFT amplitude of SR signal depends on b_{ac}, which determines the phase accumulation by the NV during a single magnetometry sub-sequence. When this phase accumulation is $\pi/2$, signal amplitude is maximized and higher harmonics of Δf in FFT can be highly suppressed. The oscillating magnetic signal amplitude that produces $\pi/2$ phase accumulation is given by below formula

$$b_{ac,(\pi/2)} = \frac{\hbar \pi^2 f_0}{2g\mu_B n} = \frac{\pi^2 f_0}{2n\gamma_e} = \frac{\pi^2}{4\tau n\gamma_e} \tag{2.4}$$

where $g = 2$ is the Lande g-factor, ν_B the Bohr magneton, γ_e gyromagnetic ratio of NV, τ free precession time between each π pulses, and n the number of π-pulses in
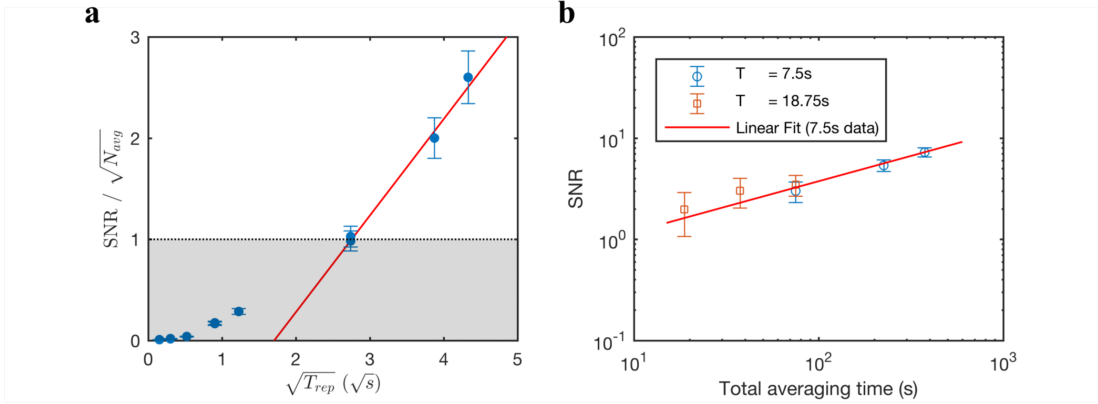
Figure 2-9: **SNR scaling of IASR measurement**. **(a)** Square root of total length of SR sequence vs. Normalized signal-to-noise ratio per single measurement. Blue dots are measurements, and red solid line is a linear fit to the measurement with normalized SNR $\geq$ 1. Gray shaded area indicates region where normalized SNR < 1. For SNR per measurement approaching to 1 or larger, SNR increases linearly as a function square root of total SR time T. From the slope, sensitivity is calculated as $\eta_B = 3.72 \pm 1.51$ μT Hz$^{-1/2}$. However, for normalized SNR < 1, SNR scales much slower than the square root of number of averages. **(b)** SR SNR measurements as a function of total averaging time for acquisitions of $T = 7.5$ s (blue circles) and $T = 18.75$ s (red boxes) duration. A power law fit to the 7.5 s data (red line) indicates square root scaling with time. Sensitivity does not depend on the SR measurement time T.

the magnetometry subsequence at central frequency f_0. For CPMG-32 sub-sequences at $f_0 = 3.7325$ MHz, the oscillating field amplitude required to produce a $\pi/2$ phase accumulation on the NV is $b_{ac,(\pi/2)} = 3.28$ μT. The FFT amplitude of the SR signal against the current-supply control voltage V_c is plotted in Figure 2-8 b. The maximum FFT SR amplitude, $S_{(\pi/2)}$ occurs for $V_c = 0.48$ Vpp, giving a magnetic signal calibration of $b_{ac}/V_c = 6.83$ μT/V.

Next, by applying $V_c = 0.48$ V to generate an oscillating magnetic field of 3.28 μT, we measured a single NV magnetometer SR signal with the duration of $T = 7.5$ s (Figure 2-8 a). Observed signal-to-noise ratio in the FFT spectrum was SNR = 2.51 ± 1.02 (Uncertainly is a standard deviation of the signal peak height over 50 measurements). This yields, a single NV magnetic field sensitivity of $\eta_B = 3.57 \pm 1.11$ μT Hz$^{-1/2}$.

Moreover, normalized single IASR measurement signal-to-noise ratio (total accu-

mulated SNR divided by square root of the number of averages) by varying the square root of total SR sequence time T is presented in Figure 2-9 a. Multiple data points overlapping at the same square root number of samples are for different number of averages with fixed time T. As shown in Figure 2-9 a, there is a linear dependence between normalized SNR and square root of T, where a single SR measurement SNR is equal or larger than 1. However, when single average SR SNR is less than 1, accumulated SNR no longer scales as square root of number of averages, but scales much slower than the square root scaling. This means that unlike coherent NV SR measurement, for an efficient incoherent SR measurement, it is important to achieve a single average SNR ~ 1, so that the accumulated SNR is proportional to square root of total measurement time. This means that unlike coherent NV SR measurement, for an efficient incoherent SR measurement, it is important to achieve a single average SNR ~ 1, so that the accumulated SNR is proportional to square root of total measurement time. From the linear fit in Figure 2-9, sensitivity of a single NV magnetometer is calculated by

$$\frac{SNR}{\sqrt{N_{avg}}} = \frac{B_{sig}}{\eta_B}\sqrt{T} \tag{2.5}$$

,where the slope is expressed as B_{sig}/η_B. Calculated sensitivity is $\eta_B = 3.72 \pm 1.51$ μT Hz$^{-1/2}$, which is consistent with previously estimated sensitivity.

Finally, cumulated signal-to-noise ratio of the IASR FFT signal as a function of total averaging time for fixed $T = 7.5$ s is plotted in Figure 2-9 b and shows that sensitivity improves with the square root of time for t $\leq 1 \times 10^3$ s. We repeated this measurement using a SR measurement duration $T = 18.75$ s and found almost the same sensitivity, demonstrating that SR magnetic field sensitivity is independent of spectral resolution. This is in contrast to NV-NMR detection using correlation spectroscopy techniques, for which magnetic field sensitivity varies as the inverse square root of spectral resolution [44]. Observed sensitivity depends on details of fluorescence collection and spin coherence properties of a specific NV.

2.4 CASR NMR measurement using Ensemble of NV spins

For nano-NMR applications to resolve chemical shifts using a single-NV synchronized readout scheme, the requirement of weak sample-sensor coupling, the presence of fast spin diffusion in nanometer-scale, and the imperfect spin state readout of single-NV experiments [48], all combine to impose a significant technical challenge. To overcome these challenges, here we used a large ensemble of NV spins and achieved NV-detected NMR signal spectral resolution ~ 1 Hz. An ensemble NV sensor enables: (i) probing micrometre-scale measurement volumes to obtain a signal dominated by the thermal spin polarization, which is not limited by diffusion; and (ii) employing a coherently averaged synchronized readout protocol to coherently sense NMR signals for an arbitrary duration (up to $\sim 10^3$ s), which gives better SNR.

Our NV ensemble instrument designed to detect NMR signals has a sensor volume that consists of the overlap region between a 13 μm NV-doped layer (NV concentration [NV] $\approx 3 \times 10^{17}$ cm^{-3}) at the diamond surface, and a 20 μm diameter optical excitation beam. Number of NV spins involved in sensing was $\sim 1.2 \times 10^9$, and measured ensemble sensor magnetic field sensitivity was $\eta_B = 30$ pT Hz$^{-1/2}$.

Interrogation of the NV ensemble sensor using a CASR scheme provides the spectral selectivity needed for molecular NMR spectroscopy. In the limit of weak coupling between NV centers and the signal source, the NV measurement back action is small and does not lead to direct dephasing of the sample spins. The detector linewidth is then limited only by technical effects (e.g., gradients in B_0), or the stability of the clock. Crucially, because our sensor is optimized to detect the thermal spin polarization, the phase of the NMR signal can be made identical over repeated NV measurements by the application of an initial $\pi/2$-pulse to the nuclear spins at $t = 0$, in order to enable coherent signal averaging. To characterize the spectral resolution limit of synchronized readout pulse sequences due to our timing source, we applied an oscillating magnetic signal consisting of three closely-spaced frequencies using a nearby coil antenna, and measured it with CASR. We observed linewidths of 0.4 mHz
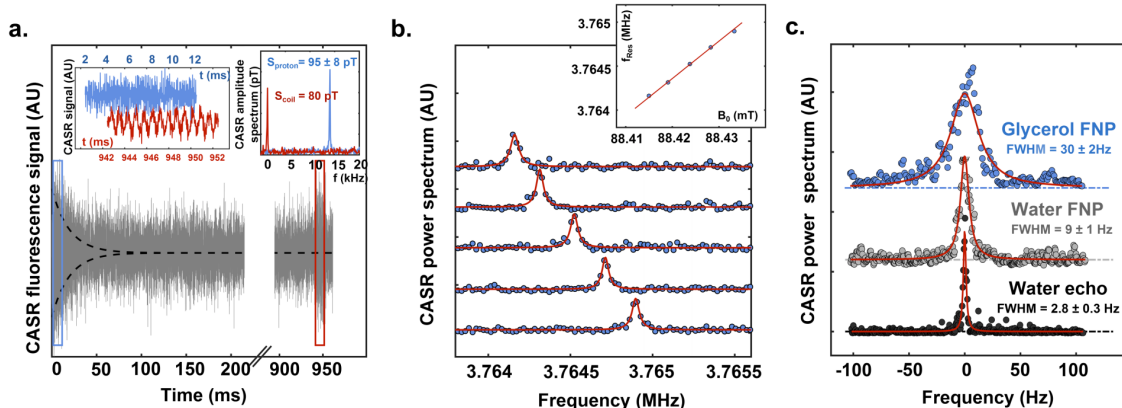
Figure 2-10: **Ensemble NV NMR detection using CASR**. **(a)** CASR time-series signal (gray trace) produced by NMR free nuclear precession (FNP) of glycerol proton spins above the diamond, with decay time $T_2^* = 10 \pm 1$ ms (dashed line). Calibrated (80 pT amplitude) magnetic field from a coil antenna is turned on at $t = 950$ ms. Comparison of FNP (blue box, blue trace inset) and antenna (red box, red trace inset) signals in the frequency domain (second inset) yields an initial FNP amplitude of 95 $\pm$ 8 pT. Total signal averaging time was 7.2×10^4 s. **(b)** Power spectra of proton NMR signals obtained from glycerol CASR-FNP data (blue circles) for varying B_0, fit to Lorentzian lineshapes (solid red lines). Linear fit of NMR resonance frequency vs. B_0 (inset) gives correct proton gyromagnetic ratio, $\gamma_p = (42.574 \pm 0.002)$ MHz/T. Signal averaging time was 2.8×10^3 s per trace. **(c)** Power spectra of measured CASR-FNP from protons in glycerol (blue circles) and pure water (gray circles), as well as CASR-spin-echo from pure water (black circles). Spectral resolution obtained with CASR-FNP of glycerol is 30 ± 2 Hz (FWHM), determined by least-squares fitting to a Lorentzian line shape (red line). Spectral resolution obtained from pure water is 9 $\pm$ 1 Hz (FWHM) with CASR-FNP, and 2.8 ± 0.3 Hz (FWHM) with CASR-spin-echo. Signal averaging times were 7.2×10^4 s (glycerol FNP), 3.1×10^4 s (water FNP), and 3.9×10^4 s (water spin echo).

(Figure 2-7 c), which is several orders of magnitude better resolution than needed for identification of molecular NMR signatures such as J-couplings and chemical shifts.

We performed CASR NMR measurements using a sample of glycerol ($C_3H_8O_3$) molecules (Figure 2-10 a). The NV-diamond sensor was placed in a cuvette filled with glycerol, and aligned in the bias field ($B_0 = 88$ mT) of a feedback-stabilized electromagnet. A resonant $\pi/2$ pulse was applied to tip the samples thermally-polarized proton spins into the transverse plane of the Bloch sphere. The proton free-nuclear-precession signal (FNP, equivalent to free-induction-decay in conventional NMR) was then measured with a CASR sequence. Near the end of this measurement, after the

sample spins were fully dephased, we used a coil antenna to apply a calibrated oscillating magnetic field pulse. Comparison of integrated peak intensities of the glycerol NMR and coil pulse signals in the CASR amplitude spectrum (Figure 2-10 a, inset) yielded an initial glycerol proton FNP amplitude of 95 ± 8 pT (1σ, for $n = 3$ measurements), approximately consistent with calculations. To exclude the possibility of spurious detection associated with room noise or sensor imperfections, we swept B_0 over 0.02 mT and repeated the CASR-FNP experiment at each value. A linear fit to the resulting NMR frequencies gave the correct value for the proton gyromagnetic ratio (Figure 2-10 b).

To assess the spectral resolution limits of NMR detection using CASR spectroscopy, we measured a sample of pure water (T_2, $T_1 > 2$ s [49]). The resulting NMR signal linewidth was 9 ± 1 Hz FWHM (Figure 9 c), which we attribute to micronscale magnetic gradients from susceptibility differences between sensor components. Gradient-induced spectral broadening is commonly observed in sub-μL volume NMR spectroscopy with microcoils [50, 51], and can be mitigated by improved susceptibility matching in the sensor design [52]. Applying π-pulses to the protons to refocus gradient-induced dephasing (CASR-spin-echo) narrowed the NMR signal linewidth to 2.8 Hz FWHM (Figure 2-10 c), in agreement with the distribution of temporal fluctuations in B_0 recorded during the experiment.

2.5   Summary and Outlook

We demonstrated that NV spin sensor with any size could achieve a frequency resolution beyond its limit of spin lifetime, only limited by the stability of an external synchronized clock or the sample spin coherence time. Single-NV synchronized readout can be useful for spectrally addressing a large-scale quantum registers in solid-state quantum simulators [53], investigating two dimensional nuclear magnetic resonance spectroscopy of intrinsic defect molecules inside a diamond [54, 55], or, combined with external magnetic field gradient [56, 57], measuring spatial information on nuclear spin quantum registers. Unfortunately, for nano-scale NMR applications using

48

single-NV synchronized readout, the requirement of weak sample-sensor coupling, combined with imperfect spin state readout of single-NV experiments, presents a significant technical challenge. Furthermore, the challenge of short signal correlation times from nanoscale liquid-state NMR samples due to molecular diffusion is not yet solved, limiting the advantages of a spectrally-selective nanoscale sensor. Until translational diffusion can be reliably restricted at these length scales (e.g., by gel media [58] or nanofabricated encapsulation chambers [59]) without increased dipolar broadening, NV ensemble SR NMR techniques will likely be of greatest utility.

Chapter 3

Control of Effective Dipolar Coupling via Manipulation of Dressed-States

3.1 Introduction

Understanding the dynamics of macroscopic quantum systems with strong interaction is a challenging topic. In recent years, several studies have reported using an ensemble of interacting NV spins to study such dynamics; from the observation of critical thermalization in a three dimensional ensemble [60] to Discrete Time Crystal (DTC) state subject to a periodic drive in a disordered spin ensemble [61]. However, unlike cold atom systems, where a Feshbach resonance [62, 63] is used as a tool to control the interaction between atoms, solid state atomic defect system faces intrinsic challenge of controlling the interactions, since defect atoms are spatially fixed inside the host lattice. In this chapter, we present a novel scheme to effectively control the dipolar coupling between strongly coupled spins through manipulation of dressed states through microwaves and test this with two strongly coupled NV spins. Inducing dressing terms into the system Hamiltonian via spin Rabi driving, we could turn on/off or tune the effective dipolar coupling between two spins. Through Ramsey

spectroscopy, we observed the change of coupling dynamics under the presence of different dressing terms in our control Hamiltonian.

3.2 Strongly Coupled Two Spin-1 System

3.2.1 System Hamiltonian with No Dressing

The system of two off-axis NV center spins is described by the given Hamiltonian

$$\mathcal{H} = H_A + H_B + H_{int} \tag{3.1}$$

where H_A and H_B are individual Hamiltonians for NV_A and NV_B respectively, and H_{int} is the interaction Hamiltonian term between two NV spins. Individual Hamiltonians can be expanded as

$$H_A = D(S_A^z)^2 + \gamma \vec{B} \cdot \vec{S}_A$$
$$H_B = D(S_B^z)^2 + \gamma \vec{B} \cdot \vec{S}_B \tag{3.2}$$

where $D = 2.87$ GHz, zero-field splitting due to NV electronic spin-spin interaction, γ, NV electronic gyromagnetic ratio, $\vec{B}$ external bias magnetic field and $\vec{S}_A$ and $\vec{S}_B$ NV spin-1 vectors. Strain term and hyperfine interaction between NV electronic spins and nitrogen nuclear spin term are excluded. Let us assume that the external bias magnetic field, B is aligned with NV_A. Then the magnetic quantum number m_s^A is a good quantum number, and the Hamiltonian can be expressed in the basis of $|m_s^A = 0\rangle$ and $|m_s^A = \pm 1\rangle$. For the off-axis NV_B, misaligned magnetic field causes state mixing, however, for the small magnetic field strength (B $\sim$ 40 G $\ll D/\gamma$), this effect is small [23], therefore, we can still use the $|m_s^B = 0\rangle$ and $|m_s^B = \pm 1\rangle$ as set of basis. Interaction Hamiltonian is given as dipole-dipole interaction between two NV spins

$$H_{int} = -\frac{J_0}{r^3} \left(3(\vec{S}_A \cdot \hat{r})(\vec{S}_B \cdot \hat{r}) - \vec{S}_A \cdot \vec{S}_B \right) \tag{3.3}$$

where $J_0 = (2\pi)$ 52MHz·nm^3 and $\vec{r}$ is a relative displacement vector between two spins. Since we are interested in the interaction in the basis of each NV spin's own quantization axis, we can in terms of $\vec{S}_{A,B}$ in terms of $(S_{A,B}^x, S_{A,B}^y, S_{A,B}^z)$ coordinate system where $z^{A,B}$ is a quantization axis for each NV spins. For two off axis NV spins, flip-flop terms $(S_A^x S_B^x + S_A^y S_B^y)$, $(S_A^x S_B^y - S_A^y S_B^x)$ enter as fast oscillating terms, which average out, therefore only the Ising interaction $S_A^z S_B^z$ remains [21].

$$H_{int} \approx -\frac{J_0 q_{A,B}}{r^3} S_A^z S_B^z = \nu S_A^z S_B^z \qquad (3.4)$$

where $q_{A,B} = -(1 - 3\cos^2\theta)$ with $\cos\theta = \hat{z} \cdot \hat{r}$ and let the effective dipolar coupling term to be expressed as ν, which is the real observable that we measure as a coupling strength. Note that other mixing terms (e.g. $S_A^x S_B^z$) can be neglected due to the strong magnetic field alignment to NV$_A$ along its z-axis and the zero field splitting [23].

3.2.2 System Hamiltonian with Dressing

Introducing dressing Hamiltonian in spin$-1/2$ system to decouple dipolar interactions (also refer as motional narrowing) has already been extensively studied in NMR community [64, 65], or observed in super conducting qubit system [66]. However, in spin-1 system, due to increased number of sub-levels to control, more complicated dynamics arise. Detailed discussion on dressed spin$-1/2$ system is presented in Appendix D. Here we work on three-level, two NV spins and discuss how driving Hamiltonian effectively changes spin coupling dynamics. Let us label a sensing NV spin as NV$_A$ and driving NV spin as NV$_B$. Total Hamiltonian of the system is

$$H(t) = D(S_A^z)^2 + \gamma B_A S_A^z + \left(\Omega_1^A \cos(\omega_1^A t) + \Omega_2^A \cos(\omega_2^A t)\right) S_A^x \qquad (3.5)$$
$$+ D(S_B^z)^2 + \gamma B_B S_B^z + \left(\Omega_1^B \cos(\omega_1^B t) + \Omega_2^B \cos(\omega_2^B t)\right) S_B^x + \nu S_A^z \otimes S_B^z$$

where D denotes zero-field splitting, ν denotes dipolar coupling between two NV spins, $\Omega_1^{A,B}$ and $\Omega_2^{A,B}$ terms correspond to Rabi frequencies of $|m_s = 0\rangle \leftrightarrow |m_s = -1\rangle$ and $|m_s = 0\rangle \leftrightarrow |m_s = +1\rangle$ transitions for NV$_A$ and NV$_B$ respectively. S_A^x and S_B^x

terms are the dressing terms in the Hamiltonian which transform the eigenstates into dressed states. Pauli matrices for spin-1 is given as,

$$
S_x = \frac{1}{\sqrt{2}}\begin{pmatrix} 0 & 1 & 0 \\ 1 & 0 & 1 \\ 0 & 1 & 0 \end{pmatrix}, \quad S_y = \frac{1}{\sqrt{2}}\begin{pmatrix} 0 & -i & 0 \\ i & 0 & -i \\ 0 & i & 0 \end{pmatrix}, \quad S_z = \begin{pmatrix} 1 & 0 & 0 \\ 0 & 0 & 0 \\ 0 & 0 & -1 \end{pmatrix} \tag{3.6}
$$

Note that when we are in single quantum basis, we consider only $|m_s = 0\rangle \leftrightarrow |m_s = +1\rangle$ transition, where $\omega_1 = 0$ and $\Omega_1 = 0$. Here, we ignore additional the flip-flop and the strain terms. In order to go to the doubly rotating frame, we apply a unitary operator

$$
V = \begin{pmatrix} e^{i\omega_1^A t} & 0 & 0 \\ 0 & 1 & 0 \\ 0 & 0 & e^{i\omega_2^A t} \end{pmatrix} \otimes \begin{pmatrix} e^{i\omega_1^B t} & 0 & 0 \\ 0 & 1 & 0 \\ 0 & 0 & e^{i\omega_2^B t} \end{pmatrix}, \tag{3.7}
$$

which commutes with $S_z^{A,B}$. Then the Hamiltonian becomes

$$
\tilde{H} = V H(t) V^\dagger - iV \frac{dV^\dagger}{dt} \tag{3.8}
$$

$$
= \frac{\Omega_1^A \cos(\omega_1^A t) + \Omega_2^A \cos(\omega_2^A t)}{\sqrt{2}} \begin{pmatrix} 0 & e^{i\omega_1^A t} & 0 \\ e^{-i\omega_1^A t} & 0 & e^{-i\omega_2^A t} \\ 0 & e^{i\omega_2^A t} & 0 \end{pmatrix} \otimes \mathbb{1}
$$

$$
+ \gamma B_A S_A^z \otimes \mathbb{1} + D(S_A^z)^2 \otimes \mathbb{1} + \left(-\omega_1^A |+1\rangle_A \langle +1|_A - \omega_2^A |-1\rangle_A \langle -1|_A \right) \otimes \mathbb{1} \tag{3.9}
$$

$$
+ \mathbb{1} \otimes \frac{\Omega_1^B \cos(\omega_1^B t) + \Omega_2^B \cos(\omega_2^B t)}{\sqrt{2}} \begin{pmatrix} 0 & e^{i\omega_1^B t} & 0 \\ e^{-i\omega_1^B t} & 0 & e^{-i\omega_2^B t} \\ 0 & e^{i\omega_2^B t} & 0 \end{pmatrix}
$$

$$
+ \mathbb{1} \otimes \gamma B_B S_B^z + D \mathbb{1} \otimes (S_B^z)^2 + \mathbb{1} \otimes \left(-\omega_1^B |+1\rangle_B \langle +1|_B - \omega_2^B |-1\rangle_B \langle -1|_B \right) + \nu S_A^z \otimes S_B^z
$$

$$
\tag{3.10}
$$

$$
\simeq \begin{pmatrix} -\omega_1^A + D + \gamma B_A & \frac{\Omega_1^A}{2\sqrt{2}} & 0 \\ \frac{\Omega_1^A}{2\sqrt{2}} & 0 & \frac{\Omega_2^A}{2\sqrt{2}} \\ 0 & \frac{\Omega_2^A}{2\sqrt{2}} & -\omega_2^A + D - \gamma B_A \end{pmatrix} \otimes \mathbb{1}
$$

$$
+ \mathbb{1} \otimes \begin{pmatrix} -\omega_1^B + D + \gamma B_B & \frac{\Omega_1^B}{2\sqrt{2}} & 0 \\ \frac{\Omega_1^B}{2\sqrt{2}} & 0 & \frac{\Omega_2^B}{2\sqrt{2}} \\ 0 & \frac{\Omega_2^B}{2\sqrt{2}} & -\omega_2^B + D - \gamma B_B \end{pmatrix} + \nu S_A^z \otimes S_A^z \qquad (3.11)
$$

where rotating-wave approximation is used to simplify the equation. To observe the change of interaction dynamics in dressed states, we use Ramsey spectroscopy. Detailed discussion on how Ramsey spectroscopy reveals coupling dynamics can be found in Appendix D. By setting $\omega_1^A = D + \gamma B_A - \delta\omega_A$, $\omega_2^A = D - \gamma B_A$, which is for single quantum Ramsey in the basis of $|m_s = 0\rangle, |m_s = +1\rangle$, $\Omega_1^A = \Omega_2^A = 0$, assuming no spin driving for NV_A, and finally, letting $\omega_1^B = D + \gamma B_B$, $\omega_2^B = D - \gamma B_B$, we have

$$
\tilde{H} = \begin{pmatrix} \delta\omega_A & 0 & 0 \\ 0 & 0 & 0 \\ 0 & 0 & 0 \end{pmatrix} \otimes \mathbb{1} + \mathbb{1} \otimes \begin{pmatrix} 0 & \frac{\Omega_1^B}{2\sqrt{2}} & 0 \\ \frac{\Omega_1^B}{2\sqrt{2}} & 0 & \frac{\Omega_2^B}{2\sqrt{2}} \\ 0 & \frac{\Omega_2^B}{2\sqrt{2}} & 0 \end{pmatrix} + \nu S_A^z \otimes S_B^z \qquad (3.12)
$$

Using this generalized Hamiltonian (3.12), we can analytically calculate eigenstates and eigenvalues, where eigenstates are expressed in the NV spin σ_z basis in doubly rotating frame. Depending on which initial state NV_B is prepared in, which basis we operate Ramsey spectroscopy, and between which basis we drive Rabi, observed transition resonances (which contains information about the interactions) via Ramsey sequence are varied. Detailed discussion on different conditions is presented in Section 3.4.

3.3 Characterization of the System

3.3.1 Individual Spin Characterization

To realize isolated system of two NV spins that are strongly coupled ($\nu_{dip} \gg \Delta$, where Δ is coupling strength between NV spin and other electronic spin bath), we used molecular implantation technique. ^{12}C isotopic purified to 99.99% diamond was used as a substrate, and 6 keV of $^{+28}$N molecular ion beam was applied with implantation dosage of $1 \times 10^9/\text{cm}^2$. After the implantation, diamond was annealed at 800 °C for 8 hours and at 1000 °C for 10 hours. More details on the sample is discussed in Appendix C.

From the confocal fluorescence scan of the molecular implanted sample, we can do robust statistical study of rate of creating double NV spins from single NV spins. From Double Electron-Electron Resonance (DEER) measurement between two NV spins, we measured dipolar coupling strength of ~0.2 MHz on average, which agrees pretty well with the estimate derived from simulated average distance between two NV spins with given implantation energy [67].

Before applying any driving Hamiltonian into the system, we first need to reconstruct the full time-independent Hamiltonian of the given two spin system. Since two NV spins have different quantization axis, it is possible to spectrally distinguish them via applying external magnetic field on one of the NV axis. From the ODMR (Optically Detected Magnetic Resonance) measurement, we set the magnet position to generate external magnetic field of B = 38.5G. In Figure 3-1 b, outer two resonance peaks correspond to $|m_s = 0\rangle$ to $|m_s = -1\rangle$ and $|m_s = 0\rangle$ to $|m_s = +1\rangle$ transitions of NV$_A$, and inner two resonance peaks correspond to $|m_s = 0\rangle$ to $|m_s = -1\rangle$ and $|m_s = 0\rangle$ to $|m_s = +1\rangle$ transitions of off-axis NV$_B$, respectively. By applying microwaves with different resonances frequencies, we can individually control and readout the spin state of each of NV spins. To characterize spin coherence properties of each of NV spins, we employed Hahn-echo sequence to measure T_2 and Ramsey spectroscopy to measure T_2^*. During each selective spin coherence measurements, uncontrolled NV is prepared in $|m_s = 0\rangle$ state. Overall measured spin coherence time is summarized in
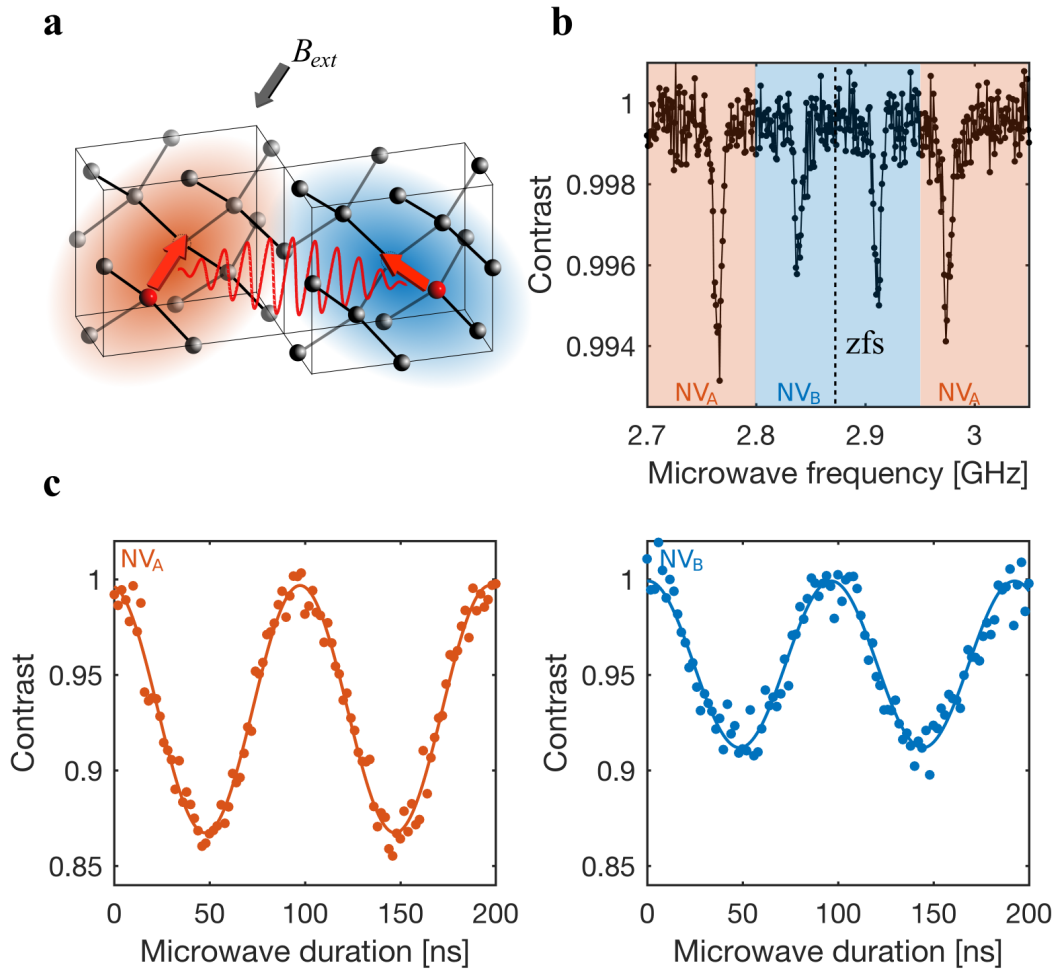
Figure 3-1: **Basic characterization measurement for two NV spin system. a**, Schematic of two NV spins inside the diamond lattice. External bias magnetic field, B_{ext} is applied to the sensor spin, NV_A (red), and the control spin, NV_B (blue) is off-quantization axis to NV_A. **b**, ODMR measurement of two NV system. Under the different Zeeman splitting due to different amount of B_{ext} field projected onto each quantization axis, we can spectrally resolve both NV spins. **c**, By applying different microwave frequencies the two NV each resonances, we can selectively induce Rabi nutation on both NV spins. This means that we can selectively control and readout the state of individual NV spins

Table 3.1.

	NV_A	NV_B
T_1	$|0\rangle$	$|0\rangle$
T_2	$\frac{|0\rangle - i|1\rangle}{\sqrt{2}}$	$|0\rangle$
T_2^*	$\frac{|0\rangle - i|1\rangle}{\sqrt{2}}$	$|0\rangle$

Table 3.1: Spin coherence times for coupled two off-axis NV system

Spin coherence times of NV_A are much longer than that of NV_B, which indicates NV_B has more noisy environment. This might be the case where NV_B has shallower depth from the surface than NV_A, therefore, subject to more surface noise [68]. To test this hypothesis, one can try to measure the depth of individual NV spins by using the surface proton NMR signal [69]. However, in this work, we didn't investigate further since NV_A already had long enough T_2^* to study interaction dynamics.

3.3.2 Coupling Strength Characterization

Double Electron Electron Resonance (DEER) Measurement

Double Electron-Electron Resonance (DEER) is a pulse scheme to measure the coupling strength between interacting spins. In two spin interacting picture, DEER measures dynamic phase accumulated by a sensor spin due to magnetic dipolar field created by an external coupled spin. First, let us consider DEER in the basis of $|m_s = 0\rangle$ and $|m_s = -1\rangle$ states of two off-axis interacting NV spins. Interaction is given as an Ising interaction with dipolar coupling strength of ν (Equation (3.4)).

DEER is based on applying spin Hahn-echo sequence on sensor spin, and applying π pulse flip on the coupled spin simultaneously when the sensor spin is flipped. Total duration of Echo pulse τ is swept to measure the phase accumulation on the sensing spin due to the dipolar field from the other spin projected onto the quantization axis of the sensing spin. In details, we first initialize two NV spins in $|00\rangle$, apply $\pi/2$ pulse on NV_A, let the system evolve for time $\tau/2$ with H_{int}, apply π pulse on both NV_A and NV_B, let the system evolve again for time $\tau/2$ with H_{int}, apply $\pi/2$ pulse on NV_A, and finally measure the population of $|0\rangle$ for NV_A. Population measurement of $|0\rangle$

for NV_A can be expressed as

$$P_{SQ} = \frac{1 - \cos(\nu\tau/2)}{2}. \tag{3.13}$$

DEER measurement can be done in different basis of NV spins. Now let us consider DEER using $|B\rangle = \frac{|+1\rangle + |-1\rangle}{\sqrt{2}}$ and $|D\rangle = \frac{|+1\rangle - |-1\rangle}{\sqrt{2}}$ of NV_A, and $|-1\rangle$, $|+1\rangle$ states for NV_B. The interaction Hamiltonian is the same. In this basis, we first initialize two NV spins in $|0-\rangle$, apply double quantum $\pi/2$ pulse on NV_A, let the system evolve for time $\tau/2$ with H_{int}, apply double quantum π pulse on NV_A and NV_B, let the system evolve for time $\tau/2$ with H_{int}, apply double quantum $\pi/2$ pulse on NV_A, and measure the population of $|0\rangle$ for NV_A (3-2 a). Population measurement of $|0\rangle$ for NV_A can be expressed as

$$P_{DQ} = \frac{1 + \cos(2\nu T)}{4}. \tag{3.14}$$

Figure 3-2 is the result of DEER measurement of our two NV spin system. In single quantum basis of sensor spin with other spin flipped between $|0\rangle$ and $|-1\rangle$ states, we measured coupling oscillation of $\nu/2 \sim 0.125 \pm 0.01$ MHz. In double quantum basis of sensor spin with other spin flipped between $|-1\rangle$ and $|+1\rangle$ states, we measured coupling oscillation of $2\nu \sim 0.495 \pm 0.031$ MHz. From both measurements, we could extract $\nu \sim 0.250 \pm 0.015$ MHz.
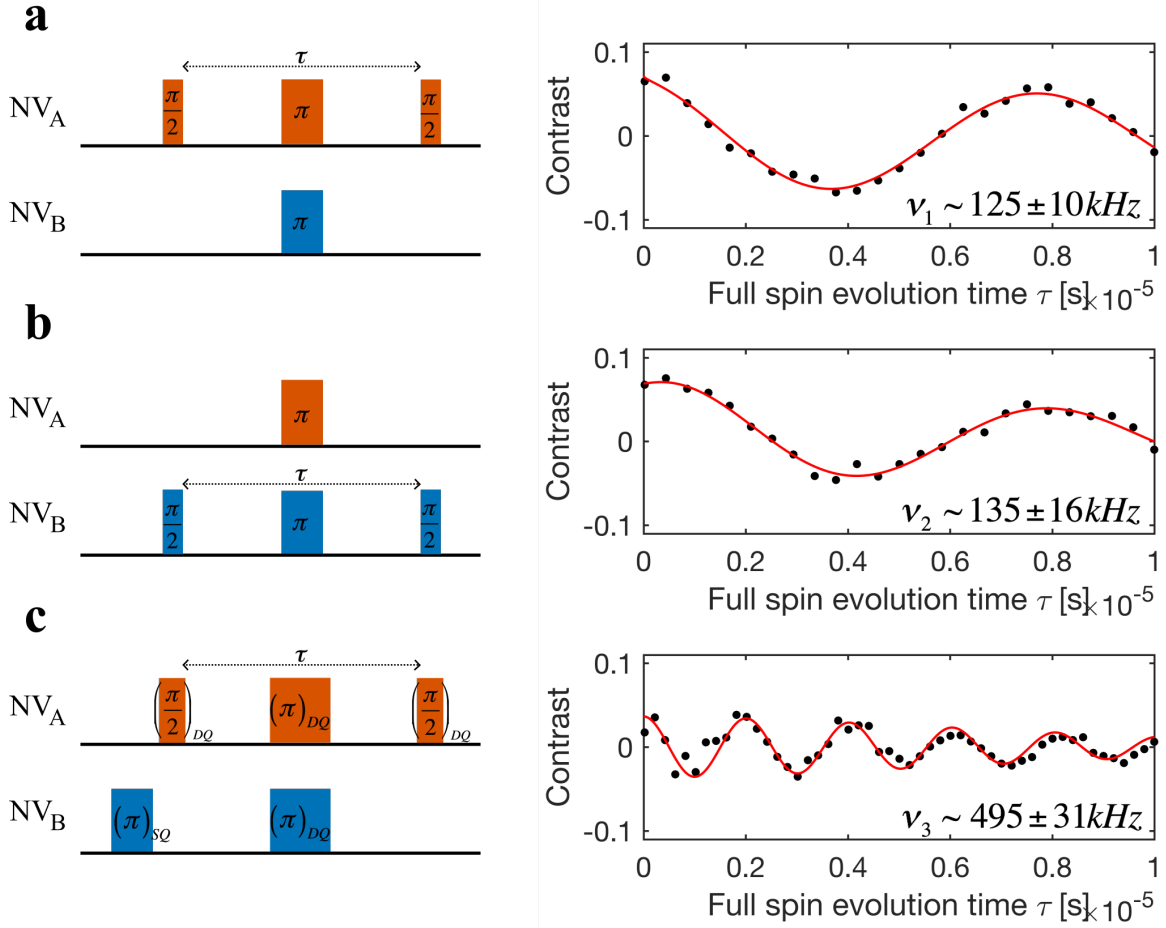
Figure 3-2: **Double Electron Electron Resonance measurement on two NV spin system. a**, DEER measurement pulse sequence and DEER signal measurement by sweeping total spin evolution time τ in single quantum basis (between $|0\rangle$ and $|-1\rangle$) of NV_A as a sensing spin, and NV_B as a control spin. NV_B is initially prepared in $|0\rangle$ and flipped to $|-1\rangle$ state when NV_A is flipped. During initial half of the τ evolution, there is no phase accumulation on NV_A, and only during the second half NV_A accumulates phase due to dipolar field of NV_B projected on the quantization axis of NV_A. This results in measuring $\nu_1 = \nu/2 \approx 0.125 \pm 0.01$ MHz. Uncertainty is calculated from the fit **b**, We repeated same measurements, but now used NV_B as a sensing spin, and NV_A as a control spin. Since the interaction Hamiltonian is symmetric over two spins, we should get the same result, and we measure $\nu_2 = \nu/2 \approx 0.135 \pm 0.016$ MHz. **c**, DEER measurement now in double quantum basis of sensing spin NV_A, and control spin NV_B is initially prepared in $|-1\rangle$. Double quantum π pulse is applied to NV_B when NV_A is flipped in double quantum basis. Since in double quantum basis, effective magnetic moment of NV_A become twice of the moment in single quantum basis, we measure twice faster phase accumulation, $\nu_3 = 2\nu \approx 0.495 \pm 0.031$ MHz. Reduction of the contrast by half is also due to the measurement in DQ basis.

Ramsey Spectroscopy Measurement

Similar mechanism as DEER, Ramsey sequence allows sensing spin, NV_A to accumulate dynamic phase due to the static dipolar field from the spin NV_B. Unlike DEER, there is no π pulse applied to NV_B, therefore, depending on which m_s state that NV_B is prepared, generated dipolar field will be varied. Let us assume that Ramsey on NV_A is done in a single quantum basis of $|0\rangle$ and $|+1\rangle$. If NV_B spin is prepared in $|m_s^B = 0\rangle$, then there is no phase accumulation on NV_A, and for $|m_s^B = \pm1\rangle$, phase of $\pm\gamma\nu\tau$ will be accumulated on NV_A. Switching the state of NV_B, we can turn on/off the coupling between two spins. We can repeat the same Ramsey measurement in a double quantum basis of $|0\rangle$ and $|B\rangle$ on NV_A. In double quantum basis, overall magnetic moment of NV_A spin becomes twice the moment in single quantum basis, therefore we measure twice larger dipolar coupling strength in double quantum basis.

First, $|-1\rangle$ and $|0\rangle$ basis of NV_A were used for Single Quantum (SQ) Ramsey. $\pi/2$ pulses for Ramsey sequence were detuned by -3 MHz, therefore, we observed three peaks with separation of hyperfine coupling $h_f = 2.16$ MHz in FFT of Ramsey signal. In Figure 3-3 a, we focused on one of three hyperfine peaks, and plotted FFT peak position change in frequency domain by preparing NV_B in $|0\rangle$ or $|\pm1\rangle$ states. As NV_B spin state is prepared in $|\pm1\rangle$, position of the resonance peak moves to $\mp\nu \approx 0.26 \pm 0.02$ MHz, relative to the peak with no-interaction turned on (NV_B in $|0\rangle$).

Next, $|B\rangle$ and $|D\rangle$ basis of NV_A were used for double quantum (DQ) Ramsey. DQ $\pi/2$ pulses for Ramsey sequence were detuned by ∓3 MHz, therefore, we observed three peaks with separation of twice of hyperfine coupling $2h_f = 4.32$ MHz in FFT of Ramsey signal, because in DQ basis, magnetic moment becomes twice. In Figure 3-3 b, we again focused on one of three hyperfine peaks, and plotted FFT peak position change in frequency domain by preparing NV_B in $|0\rangle$ or $|\pm1\rangle$ states. As NV_B spin state is prepared in $|\pm1\rangle$, position of the resonance peak moves to $\mp2\nu \approx 0.52 \pm 0.02$ MHz, relative to the peak with no-interaction turned on. Uncertainty is given by the frequency resolution of the FFT. We confirmed that Ramsey spectroscopy
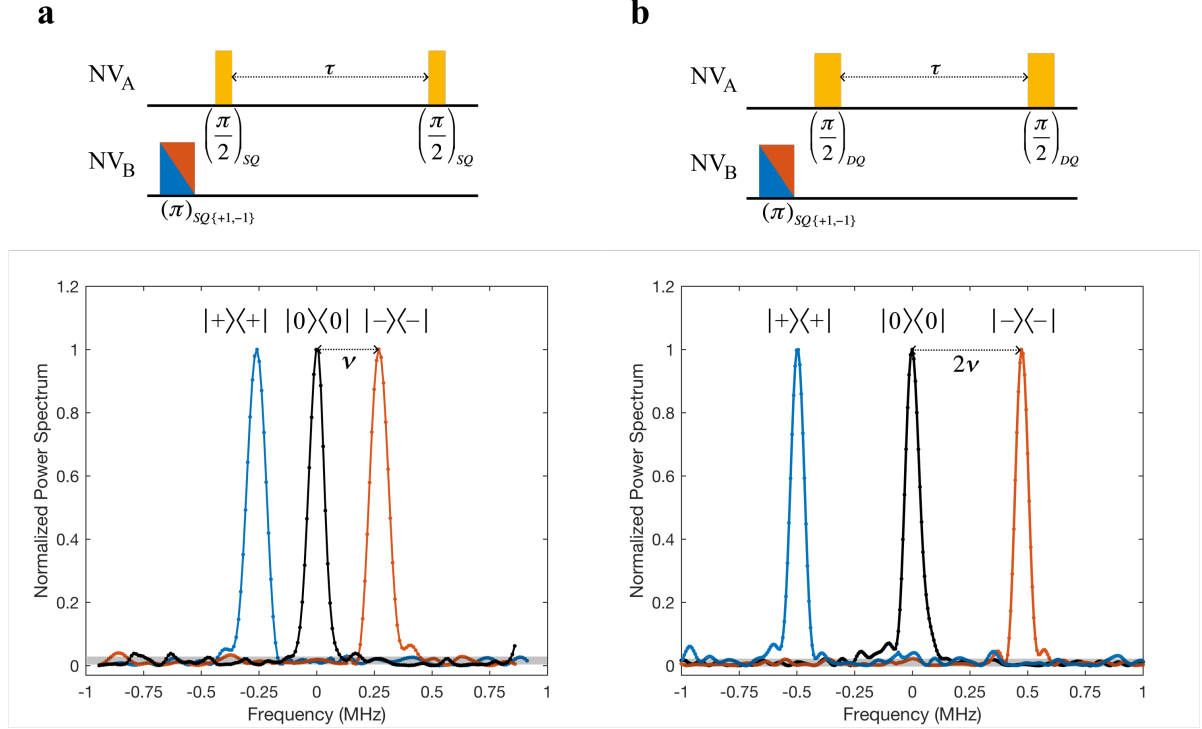
Figure 3-3: **Ramsey spectroscopy with no spin driving. a**, Ramsey spectroscopy pulse sequence and the discrete Fourier transform power spectrum from the Ramsey time series measurement. Here, Ramsey with sensing spin, NV_A, was performed in SQ basis with control spin, NV_B initialized in $|0\rangle$ (black), $|+1\rangle$ (blue) and $|-1\rangle$ (red) states. By varying total spin evolution time τ, we measured Ramsey time series signal and converted this signal into FFT power spectrum ($|\text{FFT}|^2$). Gray shaded area is indicating 1σ noise floor. Depending on the initial state of NV_B, we observed shift of the peaks in FFT, which corresponded to the dipolar coupling strength $\nu \approx 0.26 \pm 0.02$ MHz. **b**, we repeated same measurement, but now in DQ basis of sensing spin NV_A. Due to the twice of magnetic moment of spin NV_A in DQ basis, we observed twice larger shift of the peaks in FFT, $2\nu \approx 0.52 \pm 0.02$ MHz.

measurement gives consistent result as DEER, and now we can start to drive the control spin, NV_B.

3.4 Ramsey Spectroscopy on Driven Spin System

3.4.1 Ramsey with Single Quantum Drive

Analytical Calculation

For the Ramsey on NV_A in $|0\rangle$, $|-1\rangle$ single quantum basis, initial state of NV_B is prepared in $|-1\rangle$ state, and NV_B is driven by $\Omega_2^B = 0$, i.e., Rabi driving NV_B in single quantum basis, between $|0\rangle$ and $|-1\rangle$ states, the population of $m_s = 0$ state of NV_A can be calculated using Equation 3.12

$$P_A^{|0\rangle} = \frac{1}{2} + \frac{1}{2\sqrt{\Omega_1^2 + 2\nu^2}} \left(\frac{\Omega_1 + \sqrt{2}\nu - \sqrt{\Omega_1^2 + 2\nu^2}}{4} \cos\left(\delta\omega_A t + \frac{\nu}{2}t - \frac{\Omega_1}{2\sqrt{2}}t - \frac{\sqrt{\Omega_1^2 + 2\nu^2}}{2\sqrt{2}}t \right) \right.$$

$$-\frac{\Omega_1 - \sqrt{2}\nu + \sqrt{\Omega_1^2 + 2\nu^2}}{4} \cos\left(\delta\omega_A t + \frac{\nu}{2}t + \frac{\Omega_1}{2\sqrt{2}}t - \frac{\sqrt{\Omega_1^2 + 2\nu^2}}{2\sqrt{2}}t \right)$$

$$-\frac{\Omega_1 + \sqrt{2}\nu + \sqrt{\Omega_1^2 + 2\nu^2}}{4} \cos\left(\delta\omega_A t + \frac{\nu}{2}t - \frac{\Omega_1}{2\sqrt{2}}t + \frac{\sqrt{\Omega_1^2 + 2\nu^2}}{2\sqrt{2}}t \right)$$

$$\left. +\frac{\Omega_1 - \sqrt{2}\nu - \sqrt{\Omega_1^2 + 2\nu^2}}{4} \cos\left(\delta\omega_A t + \frac{\nu}{2}t + \frac{\Omega_1}{2\sqrt{2}}t + \frac{\sqrt{\Omega_1^2 + 2\nu^2}}{2\sqrt{2}}t \right) \right)$$

$$(3.15)$$

where we rewrote Ω_1^B as Ω_1. This implies that in this Ramsey measurement, there are four peaks in the FFT frequency domain, of which two on the far right and left loose amplitudes and pushed further away as we increase Ω_1, while the inner two peaks converge to $\delta\omega_A + \nu/2$. Position of the peaks in frequency domain correspond to eigenvalue differences between eigenstates where NV_A spin flips between $|0\rangle$ and $|-1\rangle$. When $\nu \ll \Omega_1$, only the peaks merged at $\delta\omega_A + \nu/2$ survive, and an effective dipolar coupling of the system becomes $\nu_{eff} = |\nu/2|$. In classical spin picture, this could be understood as effective spin population, when driven between $|0\rangle$ and $|-1\rangle$ would time averaged to $|m_s^{eff} = -1/2\rangle$ (Figure 3-4 a).

Figure 3-4: **Ramsey spectroscopy with single quantum driving. a**, Inside box shows the energy level diagram of the control spin NV_B. Only resonance of ω_2 between $|-1\rangle$ and $|0\rangle$ states is driven with Rabi frequency of Ω_2. In classical spin picture, if single quantum drive $\Omega_2 \gg \nu$, then the time-averaged effective spin state will be $m_s^{eff} \sim -1/2$, therefore, effective coupling between NV_A and NV_B becomes $\nu_{eff} = -\nu/2$. **b**, Pulse sequence for Ramsey spectroscopy with NV_B spin driven by Ω_2. NV_B spin state was initialized to $|-1\rangle$. **c**, Normalized discrete Fourier transform power spectrum of Ramsey signal. Black solid lines with red shades are the measurement, and red solid peaks are numerically calculated resonances (not including hyperfine splittings). For NV_B with no driving, resonance peak appears at ν. As we gradually increase Ω_2, multiple resonance peaks arise, and inner two peaks eventually converge into one peak ($\Omega_2 = 9$ MHz $\gg \nu$) at $\nu_{eff} = \nu/2$. Numerical simulation matched well with the measurement, except for the case of $\Omega_2 = 0.25$ MHz. This is due to the detuning in the Rabi drive (ω_2), which was induced by the temperature drift of the system. Not all of the resonances were visible due to limited signal-to-noise ratio of the measurement.

64

Results

For the measurement, we detuned $\pi/2$ pulses on Ramsey sequence by -3 MHz, and resolved all three hyperfine peaks in FFT. We focused on one hyperfine peak, and traced position of the peak in frequency domain as we changed Ω_1. Due to limited signal-to-noise ratio, we couldn't resolve all four peaks predicted in our analytical calculation in Equation 3.15, however, trace of main two inner peaks were visible. As we increased Ω_1, FFT peaks indeed merged at $\nu_{eff} = \nu/2 \approx 0.13$ MHz.

3.4.2 Ramsey with Double Quantum Even Drive

Analytical Calculation

Now, for the Ramsey on NV_A between $|0\rangle$ and $|+1\rangle$ single quantum basis, initial state of NV_B is $|+1\rangle$ state, and when $\Omega_2^B = \Omega_1^B = \Omega$, i.e., double quantum even driving NV_B between $|0\rangle$ and $|B\rangle$ state, the population of $m_s = 0$ state of NV_A can be calculated as following

$$
\begin{aligned}
P = &\frac{7}{8} + \frac{1}{8(\Omega^2 + 4\nu^2)} \left(-4\Omega^2 \cos(\delta\omega_A t) + 2\Omega\nu \cos\left(\delta\omega_A t - \frac{\Omega t}{2}\right) - 2\Omega\nu \cos\left(\delta\omega_A t + \frac{\Omega t}{2}\right) \right. \\
&+ \left(-8\nu^2 + 4\nu\sqrt{\Omega^2 + 4\nu^2}\right) \cos\left(\delta\omega_A t - \frac{\sqrt{\Omega^2 + 4\nu^2}}{2}t\right) \\
&+ \left(-8\nu^2 - 4\nu\sqrt{\Omega^2 + 4\nu^2}\right) \cos\left(\delta\omega_A t + \frac{\sqrt{\Omega^2 + 4\nu^2}}{2}t\right) \\
&- \left(\frac{\Omega^2}{2} + \Omega\nu + 2\nu^2 - \frac{\Omega\sqrt{\Omega^2 + 4\nu^2}}{2} - \nu\sqrt{\Omega^2 + 4\nu^2}\right) \cos\left(\delta\omega_A t - \frac{\Omega}{2}t - \frac{\sqrt{\Omega^2 + 4\nu^2}}{2}t\right) \\
&- \left(\frac{\Omega^2}{2} - \Omega\nu + 2\nu^2 + \frac{\Omega\sqrt{\Omega^2 + 4\nu^2}}{2} - \nu\sqrt{\Omega^2 + 4\nu^2}\right) \cos\left(\delta\omega_A t + \frac{\Omega}{2}t - \frac{\sqrt{\Omega^2 + 4\nu^2}}{2}t\right) \\
&- \left(\frac{\Omega^2}{2} + \Omega\nu + 2\nu^2 + \frac{\Omega\sqrt{\Omega^2 + 4\nu^2}}{2} + \nu\sqrt{\Omega^2 + 4\nu^2}\right) \cos\left(\delta\omega_A t - \frac{\Omega}{2}t + \frac{\sqrt{\Omega^2 + 4\nu^2}}{2}t\right) \\
&\left. - \left(\frac{\Omega^2}{2} - \Omega\nu + 2\nu^2 - \frac{\Omega\sqrt{\Omega^2 + 4\nu^2}}{2} + \nu\sqrt{\Omega^2 + 4\nu^2}\right) \cos\left(\delta\omega_A t + \frac{\Omega}{2}t + \frac{\sqrt{\Omega^2 + 4\nu^2}}{2}t\right) \right)
\end{aligned}
$$

$$(3.16)$$

This implies that in this Ramsey spectroscopy, there are total nine peaks, of which six peaks loose their amplitudes and pushed further away as we increase Ω, while the inner three peaks converge to $\delta\omega_A$. Position of the peaks in frequency domain correspond to eigenvalue differences between eigenstates of the Hamiltonian in (3.12), where NV_A spin flips between $|0\rangle$ and $|+1\rangle$. When $\nu \ll \Omega$, only the peaks merged at $\delta\omega_A$ survive, and an effective dipolar coupling of the system becomes $\nu_{eff} = 0$. In classical spin picture, this could be understood as effective spin population, when driven between $|0\rangle$ and $|B\rangle$ would time averaged to $|0\rangle$.

Results

For the measurement, we performed Ramsey sequence in double quantum basis, to enhance the effective magnetic moment of a sensor spin NV_A. We detuned double quantum $\pi/2$ pulses on Ramsey sequence by ∓ 3 MHz, and resolved all three hyperfine peaks in FFT. We focused on one hyperfine peak, and traced position of the peak in frequency domain as we changed Ω. Due to limited signal-to-noise ratio, we couldn't resolve all nine peaks predicted in our analytical calculation in Equation 3.16, however, trace of few main peaks were visible. As we increased Ω, FFT peaks indeed merged at $\nu_{eff} = 0$.

3.4.3 Ramsey with Double Quantum Uneven Drive

Analytical Calculation

Finally, for the Ramsey on NV_A between $|0\rangle$ and $|+1\rangle$ single quantum basis, initial state of NV_B prepared in $|0\rangle$, driven with $\Omega_1^B \neq \Omega_2^B \neq 0$, which is double quantum uneven drive, we can still analytically solve the general Hamiltonian (Equation (3.12)) to extract resonances. Let $\Omega_1^B = \Omega_1$ and $\Omega_2^B = \Omega_2$. If we focus on the case where $\nu \ll \Omega_1, \Omega_2$, then under this condition, peaks merge at an arbitrary position in frequency domain, which is not $\delta\omega_A$ anymore. We can analytically calculate this resonance position where peaks converge, which corresponds to new effective dipolar coupling ν_{eff} with unevenly driven Hamiltonian.
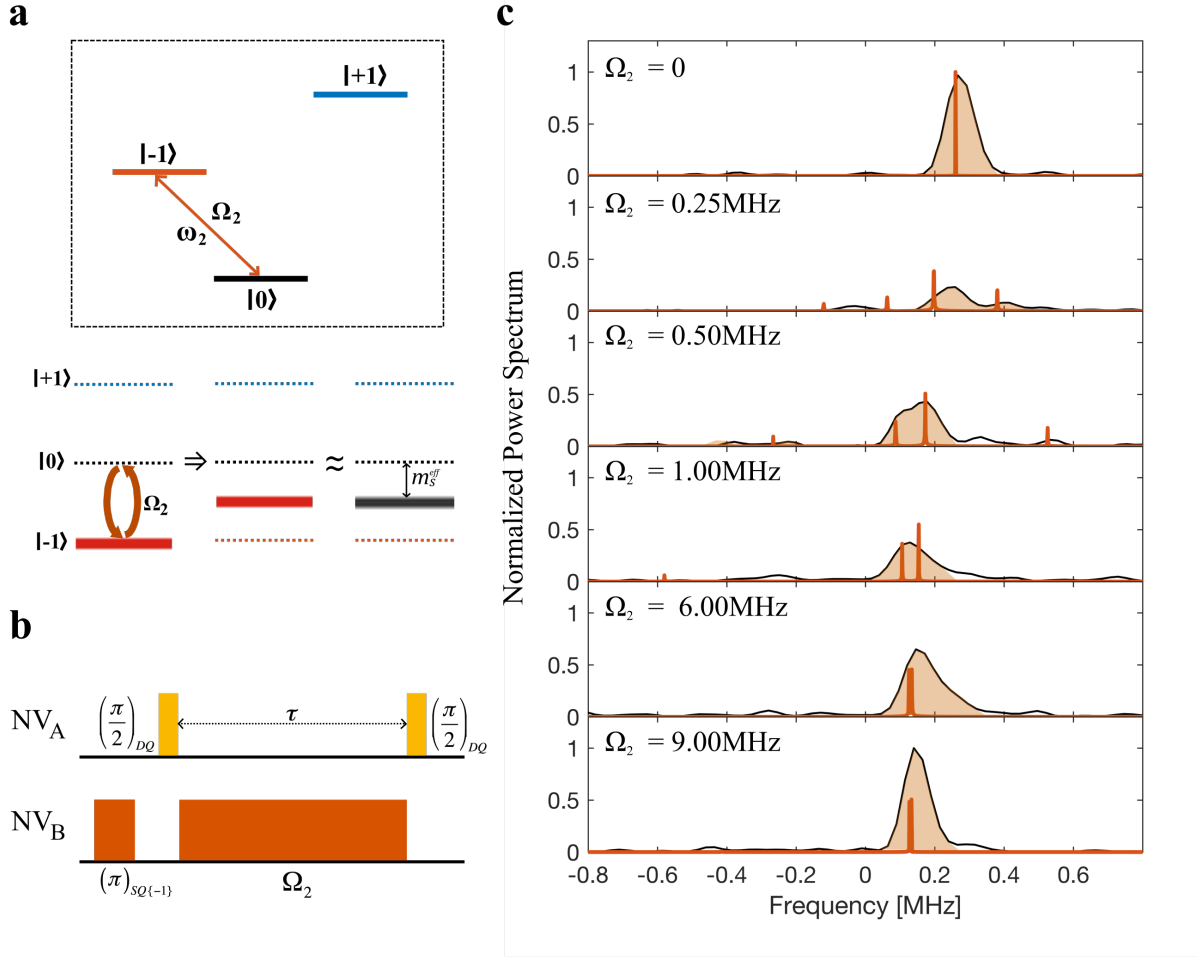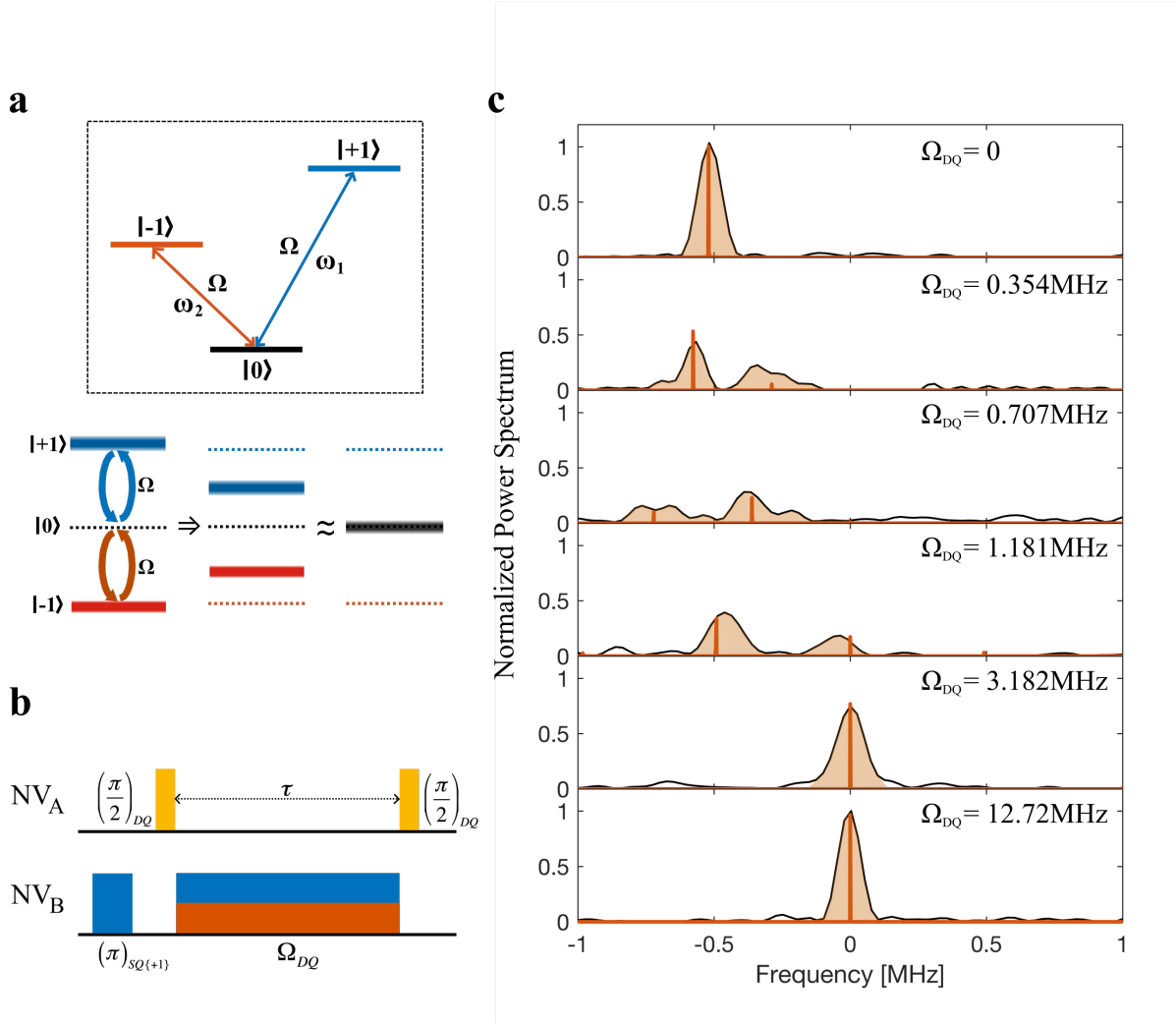
Figure 3-5: **Ramsey spectroscopy with double quantum even driving. a**, Inside box shows the energy level diagram of the control spin NV_B. Resonances of ω_1 (between $|+1\rangle$ and $|0\rangle$ states) and ω_2 (between $|-1\rangle$ and $|0\rangle$ states) are driven with same Rabi frequencies of $\Omega_1 = \Omega_2 = \Omega$. In classical spin picture, if double quantum even drive $\Omega \gg \nu$, then the time-averaged effective spin state will be $m_s^{eff} \sim 0$, therefore, effective coupling between NV_A and NV_B becomes $\nu_{eff} = 0$. **b**, Pulse sequence for Ramsey spectroscopy with NV_B spin driven by double quantum $\Omega = \Omega_{DQ}$. NV_B spin state was initialized to $|+1\rangle$. **c**, Normalized discrete Fourier transform power spectrum of Ramsey signal. Black solid lines with red shades are the measurement, and red solid peaks are numerically calculated resonances (not including hyperfine splittings). For NV_B with no driving, $\Omega_{DQ} = 0$, resonance peak appears at -2ν, because NV_A is in DQ basis. As we gradually increase Ω_{DQ}, multiple resonance peaks arise, and eventually one peak at $\nu_{eff} = 0$ remains ($\Omega_{DQ} = 12.72$ MHz). Numerical simulation matched well with the measurement. Broadened linewidth observed in $\Omega_{DQ} = 0.354$ MHz and $\Omega_{DQ} = 0.707$ MHz are due to the imperfect double quantum drive of all three hyperfine states. Not all of the resonances were visible due to limited signal-to-noise ratio of the measurement.

$$\nu_{eff} = \Re[\frac{(1+i\sqrt{3})(-24\Omega_1^2 - 24\Omega_2^2)}{24 \times 2^{2/3}\left(-1728\nu\Omega_1^2 + 1728\nu\Omega_2^2 + \sqrt{4(-24\Omega_1^2 - 24\Omega_2^2)^3}\right)^{1/3}} + \tag{3.17}$$

$$\frac{(1-i\sqrt{3})\left(-1728\nu\Omega_1^2 + 1728\nu\Omega_2^2 + \sqrt{4(-24\Omega_1^2 - 24\Omega_2^2)^3}\right)^{1/3}}{48 \times 2^{1/3}}] + \frac{\sqrt{\Omega_1^2 + \Omega_2^2}}{2\sqrt{2}}$$

$$\approx \frac{1}{2}\frac{(\Omega_1^2 - \Omega_2^2)}{(\Omega_1^2 + \Omega_2^2)}\nu \tag{3.18}$$

for $\nu \ll \Omega_1, \Omega_2$. This simple analytical formula infers that by tuning Ω_1, Ω_2, we can set an effective dipolar coupling strength to be continuously varied between $-\nu/2$ and $+\nu/2$. This result could also be explained by the classical spin driving picture. For uneven double quantum driving with Ω_1 and Ω_2, each spin state $|+1\rangle$ and $|-1\rangle$ will have spin population proportional to Ω_1^2 and Ω_2^2, respectively. For fast driving limit, each population is averaged into half, and the overall net spin is $\frac{1}{2}(\Omega_1^2 - \Omega_2^2)$ (Figure 3-6 a). By normalizing with total population $\Omega_1^2 + \Omega_2^2$, we also get the same result as equation (3.18). Furthermore, equation (3.18) is a generalized formula which satisfies different driving conditions; when $\Omega_1 = \Omega_2$, then we get $\nu_{eff} = 0$, and when $\Omega_2 = 0$, then we get $\nu_{eff} = \nu/2$ as positions where Ramsey FFT peaks converge.

Results

For the measurement, again we performed Ramsey sequence in double quantum basis, to enhance the effective magnetic moment of a sensor spin NV_A. We detuned double quantum $\pi/2$ pulses on Ramsey sequence by ∓ 3 MHz, and resolved all three hyperfine peaks in FFT. We focused on one hyperfine peak, and traced position of the peak in frequency domain as we changed Ω_1 and Ω_2. To satisfy the $\nu \ll \Omega_1, \Omega_2$ condition, all the measurements are done with $2MHz < \Omega_1, \Omega_2$. We define $\alpha = \frac{(\Omega_1 - \Omega_2)}{(\Omega_1 + \Omega_2)}$ as a control parameter, and measured peak converging points. As α is swept from -1 to +1, we observed FFT peak transition from $+\nu = +0.26$ MHz to $-\nu = -0.26$ MHz (Figure 3-6 c, Figure 3-7 b).

Figure 3-6: **Ramsey spectroscopy with double quantum uneven driving. a**, Inside box shows the energy level diagram of the control spin NV_B. Resonances of ω_1 (between $|+1\rangle$ and $|0\rangle$ states) and ω_2 (between $|-1\rangle$ and $|0\rangle$ states) are driven with different SQ Rabi frequencies of $\Omega_1 > \Omega_2$. In classical spin picture, if double quantum uneven drive $\Omega_1 > \Omega_2 \gg \nu$, then the time-averaged effective spin state will be $m_s^{eff} \sim (\Omega_1^2 - \Omega_2^2)/2(\Omega_1^2 + \Omega_2^2)$, therefore, effective coupling between NV_A and NV_B becomes $\nu_{eff} = m_s^{eff}\nu$. **b**, Pulse sequence for DQ Ramsey spectroscopy with NV_B spin driven by double quantum uneven drive $\Omega_{1,2}$. NV_B spin state was initialized to $|0\rangle$. **c**, Normalized discrete Fourier transform power spectrum of Ramsey signal. Black dots are the measurement, and red solid lines are Lorentzian fits to the data. Control parameter $\alpha = (\Omega_1 - \Omega_2)/(\Omega_1 + \Omega_2)$. For NV_B with SQ driving, $\alpha = \pm1$, resonance peak appears at $\pm\nu$, because NV_A is in DQ basis. For NV_B with DQ even driving, $\alpha = 0$, resonance peak appears at 0. As we gradually sweep α from -1 to +1 with $\Omega_1, \Omega_2 \gg \nu$, single resonance peak smoothly shifted from $\nu_{eff} = \nu$ to $\nu_{eff} = -\nu$. All the measurements are done with $\Omega_1, \Omega_2 > 2$ MHz

69

Figure 3-7: **Control of effective dipolar coupling via double quantum uneven driving.** **a**, Numerically calculated values for ν_{eff} by varying SQ Rabi frequencies for both transitions. Ω_1 and Ω_2 are normalized by the maximum SQ Rabi frequencies, and here we assumed for $\Omega_1, \Omega_2 \ll \nu$. White dotted diagonal line reveals transition of ν_{eff} from $+\nu$ to $-\nu$ by sweeping relative SQ Rabi frequencies. **b**, Cross sectional plot of ν_{eff} transition by varying $\alpha = (\Omega_1 - \Omega_2)/(\Omega_1 + \Omega_2)$. Black hallow circles are the measurements, blue crosses are the numerical simulation and red solid line is the formula from Equation 3.18. Black dashed lines are indicating $\pm\nu$ limits. Error bars are calculated from the spectral resolution of the FFT.

3.5   Summary and Outlook

We measured the change of the effective dipolar coupling in a coupled two spin system, when one of the spins is driven into a dressed state. Dressing with uneven Rabi driving between different ground state sub-levels ($|0\rangle \leftrightarrow |\pm1\rangle$), we could tune the effective coupling strength between $-\nu/2 < \nu_{eff} < +\nu/2$, and the transition was observed via Ramsey spectroscopy. The dressing scheme is a robust way to tune the effective coupling. Unlike other complicated pulse schemes [70] to manipulate effective couplings, where the duration and fidelity of the engineered Hamiltonian are limited by pulse errors, our scheme is effective as long as the dressing pulse is applied. The dressing scheme has already been applied to nitrogen electronic spin defect, P1s , to suppress overall dipolar field noise on NV spins [71, 72]. Ramsey spectroscopy by varying the spin driving parameters can be used as a spectroscopic tool to measure overall effective coupling strengths between NV spins and the P1 spin bath (for high [N] density samples). Furthermore, recent studies have reported dense

ensemble NV diamond samples with high conversion ratio from N to NV, resulting in NV-NV couplings as a dominant source of spin interactions [21]. In this regime, our scheme can be directly applied as a tuning knob to change the coupling dynamics or the local disorder amplitude to study transition of non-equilibrium phases in strongly correlated many body system.

Chapter 4

Geometric Phase Magnetometry

4.1   Introduction

The geometric phase [73, 74] plays a fundamental role in a broad range of physical phenomena [75, 76, 77]. Although it has been observed in many quantum platforms [78, 79, 80, 81] and is known to be robust against certain types of noise [82, 83], geometric phase applications are somewhat limited, including certain protocols for quantum simulation [84, 85] and computation [86, 3, 87, 88]. However, when applied to quantum sensing, e.g., of magnetic fields, unique aspects of the geometric phase can be exploited to allow realization of both good magnetic field sensitivity and large field range in one measurement protocol. This capability is in contrast to conventional dynamic-phase DC magnetometry, where there is a trade-off between sensitivity and field range. In this chapter, we use a single NV electronic spin in diamond to demonstrate key advantages of geometric-phase DC magnetometry: it resolves the 2π phase ambiguity limiting dynamic-phase magnetometry, and also decouples magnetic field range and sensitivity, leading to a 400-fold enhancement in field range at constant sensitivity in our experiment. We also present additional improvement of magnetic field sensitivity in the non-adiabatic regime of mixed geometric and dynamic phase evolution. By employing a power spectral density analysis [89], we find that adiabaticity plays an important role in controlling the degree of coupling to environmental noise and hence the spin coherence timescale.

4.2 Dynamic-Phase magnetometry

4.2.1 Dynamic-Phase DC magnetometry Protocol

Before discussing about geometric-phase magnetometry, let us first revisit conventional dynamic-phase magnetometry, i.e. Ramsey interferometry. In magnetometry using a two-level system (e.g., two spin states), the amplitude of an unknown magnetic field B can be estimated by determining the relative shift between two energy levels induced by that field. A commonly used approach is to measure the dynamic phase accumulated in a Ramsey interferometry protocol as illustrated in Figure 4-1 a. An initial resonant $\pi/2$ pulse prepares the system in a superposition of the two levels. In the presence of an external static magnetic field B along the quantization axis, the system evolves under the Hamiltonian $H = \hbar\gamma B\sigma_z/2$, where γ denotes the gyromagnetic ratio and σ_z is the z-component of the Pauli spin vector. During the interaction time T (limited by the spin dephasing time T_2^*), the Bloch vector $\vec{s}(t)$ depicted on the Bloch sphere precesses around the fixed Larmor vector $\vec{R} = (0, 0, \gamma B)$, and acquires a dynamic phase $\Phi_d = \gamma BT$. The next $\pi/2$ pulse maps this phase onto a population difference $P = \cos\phi_d$, which can be measured to determine ϕ_d and hence the magnetic field B. Such dynamic-phase magnetometry possesses two well-known shortcomings. First, the sinusoidal variation of the population difference with magnetic field leads to a 2π phase ambiguity in interpretation of the measurement signal and hence determination of B. Second, there is a trade-off between magnetic field sensitivity and field range, as the interaction time also restricts the shot-noise-limited magnetic field sensitivity: $\eta \propto 1/T^{1/2}$. Use of a quantum phase estimation algorithm [90, 91] or non-classical states [92, 93] can alleviate these disadvantages; however, they require either large resource overhead (additional experimental time) or realization of long-lived entangled or squeezed states.

4.2.2 2π Phase Ambiguity in Dynamic-Phase Magnetometry

In general, dynamic-phase magnetometry signal and its derivative are expressed as

$$P_d(B) = \cos(\gamma BT) \ , \ \frac{dP_d(B)}{dB} = \gamma T \sin(\gamma BT) \qquad (4.1)$$

For any measured signal P_d, there are infinite degenerate magnetic field values, which are related by $B_m = B + 2\pi m(\gamma T)^{-1}$, where $m = 0, \pm 1, \pm 2 \ldots, \infty$ is an integer. This degeneracy cannot be resolved by measuring the slope or adding a magnetic field offset, leading to a fundamental limit in magnetic field range. In Figure 4-2 a, the dynamic-phase signal is plotted in 3D as a function of magnetic field B, signal P_d, and derivative dP_d/dB. When the dynamic-phase magnetometry curve is projected onto the $(P_d, dP_d/dB)$ plane, all data points lie on a closed 1D curve, given by $P_d^2 + (\gamma T)^{-2} (dP_d/dB)^{-2} = 1$. Even if a magnetic field offset is added, one encounters another set of infinite degeneracies. For this reason, the degeneracy of dynamic-phase magnetometry signal can be resolved only if the interaction time T is changed (for example, via a quantum phase estimation algorithm). On the $(P_d, dP_d/dB)$ plane, this approach is understood as changing the area of the closed curve. However, changing T imposes an inevitable trade-off of magnetic field range with sensitivity. Accounting for the three NV hyperfine transitions, the dynamic phase magnetometry signal becomes:

$$P_d(B) = \frac{1}{3} \sum_{m_I = -1, 0, +1} \cos\left[(\gamma B + m_I \omega_{HF})T\right] = \cos(\gamma BT)[1 + 2\cos(\omega_{HF}T)] \quad (4.2)$$

where $\omega_{HF} = 2.16$ MHz, the hyperfine splitting due to ^{14}N nuclear spin. The hyperfine transitions introduce an envelope modulation to P_d, which changes the area of the closed curve in $(P_d, dP_d/dB)$, but all data points still lie on the same curve. Thus, it is still not possible to resolve the degeneracy either by measuring the slope or moving to other magnetic field values.

4.2.3 Sensitivity and Field Range of Dynamic-Phase Magnetometry

To calculate the sensitivity and field range, the average change of fluorescence per measurement is recast as $\Delta\mathrm{FL} = \alpha\beta$, where $\alpha \sim 10\%$ is the NV spin-state-dependent fluorescence contrast, and $\beta \sim 0.015$ is the average number of photons collected per measurement. The sensitivity is given by $\eta \approx (\mathrm{SNR})^{-1}|dP/dB|_{max}^{-1}\sqrt{t_m}$, where $\mathrm{SNR} = \Delta\mathrm{FL}/\sqrt{\beta} = \alpha\sqrt{\beta}$ represents the signal-to-noise ratio of a single measurement, $|dP/dB|_{max}$ is the maximum slope of the magnetometry curve, and $t_m \approx T$ is the measurement time. For dynamic phase magnetometry, the maximum slope is $|dP_d/dB|_{max} = \gamma T$, and then the sensitivity is

$$\eta \approx \frac{1}{\gamma\alpha\sqrt{\beta}}\frac{1}{\sqrt{T}} \tag{4.3}$$

The maximum field-range is defined as the half cycle of one magnetometry oscillation:

$$B_{max} \approx \frac{\pi}{\gamma T} \tag{4.4}$$

Thus, the range of magnetic field amplitudes that one can determine without modulo 2π phase ambiguity is limited to one cycle of oscillation. Consequently, an improvement in field range via shorter T comes at the cost of a degradation in sensitivity.
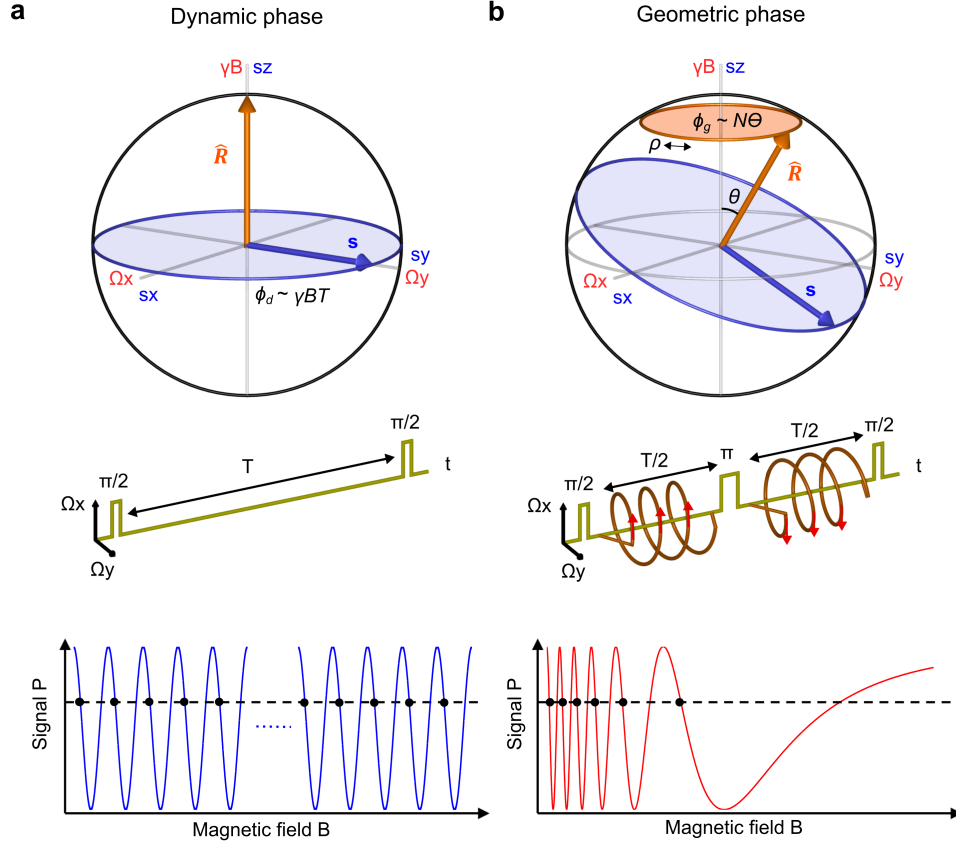
Figure 4-1: **Concepts of dynamic and geometric-phase magnetometry**. **a**, For dynamic-phase magnetometry with an NV spin, the Bloch vector $\vec{s} = (s_x, s_y, s_z)$ (blue arrow), initially prepared by a $\pi/2$ pulse in a superposition state between two levels, precesses about the fixed Larmor vector $\vec{R} = (0, 0, \gamma B)$ (red arrow). During the interaction time T between the two $\pi/2$ pulses, the spin coherence accumulates a dynamic-phase $\phi_d = \gamma BT$, equivalent to the angle swept by the Bloch vector on the equator. The phase is then mapped by a second $\pi/2$ pulse to a population difference signal $P = \cos \phi_d$, which is measured optically. Due to a 2π phase periodicity, an infinite number of magnetic field values (black dots) give the same signal, leading to an ambiguity. **b**, For geometric-phase magnetometry with an NV spin, a Berry sequence is employed. The Bloch vector is first prepared by a $\pi/2$ pulse in a superposition state between two levels. An additional off-resonant driving is then used to rotate the Larmor vector about the z-axis N times, $\vec{R}(t) = (\Omega \cos \rho(t), \Omega \sin \rho(t), \gamma B)$, where $\rho(t) = 4\pi Nt/T$. The spin coherence acquires a geometric-phase $\phi_g = N\Theta$, proportional to the number of rotations N and the solid angle $\Theta = 2\pi(1 - \cos \theta)$ subtended by the trajectory of the Larmor vector. To cancel the dynamic-phase and double the geometric-phase, the direction of rotation is alternated before and after a π pulse at the midpoint of the interaction time. At the end of the Berry sequence, the phase is mapped by a second $\pi/2$ pulse to a population difference signal $P = \cos \phi_g$, which is measured optically. The signal exhibits chirped oscillation with magnetic field amplitude, which yields at most finite magnetic field degeneracies (black dots). The signal vs. field slope resolves this ambiguity.
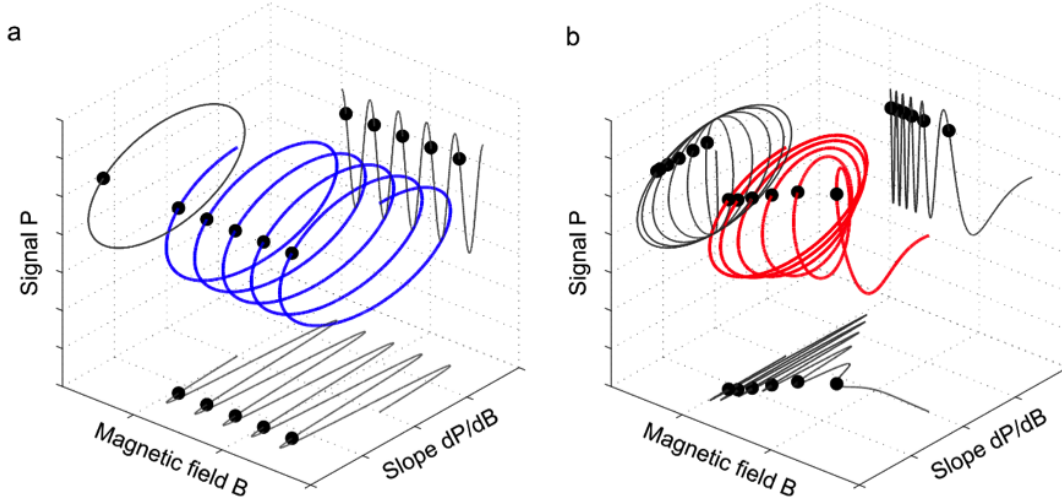
Figure 4-2: **Graphical representation of 2π phase ambiguity**. Magnetometry signal P and slope dP/dB are plotted against magnetic field B. Gray curves are projections. **a**, Dynamic-phase magnetometry. All data points lie on a single circle on the $(P, dP/dB)$ plane. Thus there are infinite possibilities of B (black dots) projected onto the same point on the $(P, dP/dB)$ plane. Adding a magnetic field offset does not solve this 2π phase ambiguity. **b**, Geometric phase magnetometry. Since $P(B)$ is chirped, data points are distinct on the $(P, dP/dB)$ plane, except for $P = \pm 1$. There are finite values of B (black dots) that give the same signal; but one can resolve this degeneracy by also evaluating dP/dB. For $P = \pm 1$, once can still resolve the degeneracy by adding a known magnetic field offset.

4.3   Geometric-Phase Magnetometry

4.3.1   Geometric-Phase DC Magnetometry Protocol

To implement geometric-phase magnetometry, we use a modified version of an experimental protocol (Berry sequence) previously applied to a superconducting qubit [81]. In our realization, the NV spin sensor is placed in a superposition state by a $\pi/2$ pulse, where driving frequency of the $\pi/2$ pulse is chosen to be resonant with the NV transition at $B = 0$ (i.e. zero signal field), and then acquires a geometric-phase due to off-resonant driving with control parameters cycled along a closed path as illustrated in Figure 4-1 b. Under the rotating wave approximation and assuming only two of the NV m_s ground-state sub-levels are addressed by the microwave driving field, the

effective two-level Hamiltonian is given by:

$$H = \frac{\hbar}{2}(\Omega \cos{(\rho)}\sigma_x + \Omega \sin{(\rho)}\sigma_y + \gamma B \sigma_z) \tag{4.5}$$

Here, Ω is the NV spin Rabi frequency for the microwave driving field, ρ is the phase of the driving field, and $\vec{\sigma} = (\sigma_x, \sigma_y, \sigma_z)$ is the Pauli spin vector. By sweeping the phase, the Larmor vector $\vec{R}(t) = R \cdot (\sin\theta\cos\rho, \sin\theta\sin\rho, \cos\theta)$, where $\cos\theta = \gamma B/(\Omega^2 + (\gamma B)^2)^{1/2}$, $R = (\Omega^2 + (\gamma)^2)^{1/2}$, rotates around the z axis. The Bloch vector $\vec{s}(t)$ then undergoes precession around this rotating Larmor vector (for detailed picture of the measurement protocol, see Figure 4-3). If the rotation is adiabatic (i.e., adiabaticity parameter $A \equiv \rho \cdot \sin\theta/2R \ll 1$), then the system acquires a geometric-phase proportional to the product of (i) the solid angle $\Theta = 2\pi(1 - \cos\theta)$ subtended by the Bloch vector trajectory and (ii) the number of complete rotations N of the Bloch vector around the Larmor vector in the rotating frame defined by the frequency of the initial $\pi/2$ pulse. We apply this Bloch vector rotation twice during the interaction time , with alternating direction separated by a π pulse, which cancels the accumulated dynamic phase and doubles the geometric phase: $\phi_g = 2N\Theta$ (full derivation in next section). A final $\pi/2$ pulse allows this geometric-phase to be determined from standard fluorescence readout of the NV spin-state population difference:

$$P_{meas}(B) = \cos\left[4\pi N \left(1 - \frac{\gamma B}{\sqrt{(\gamma B)^2 + \Omega^2}}\right)\right] \tag{4.6}$$

This normalized geometric phase signal exhibits chirped oscillation as a function of magnetic field. There are typically only a small number of field ambiguities that give the same signal P_{meas}; these can be resolved uniquely by measuring the slope dP_{meas}/dB (Figure 4-2 b). From the form of Equation 4.6, it is evident that at large B, cosine signal approaches to zero like B^{-2}, and the slope goes to zero. Hence, we define the field range as the largest magnetic field value (B_{max}) that gives the last oscillation minimum in the signal: $B_{max} \propto \Omega N^{1/2}$. Importantly, the field range of
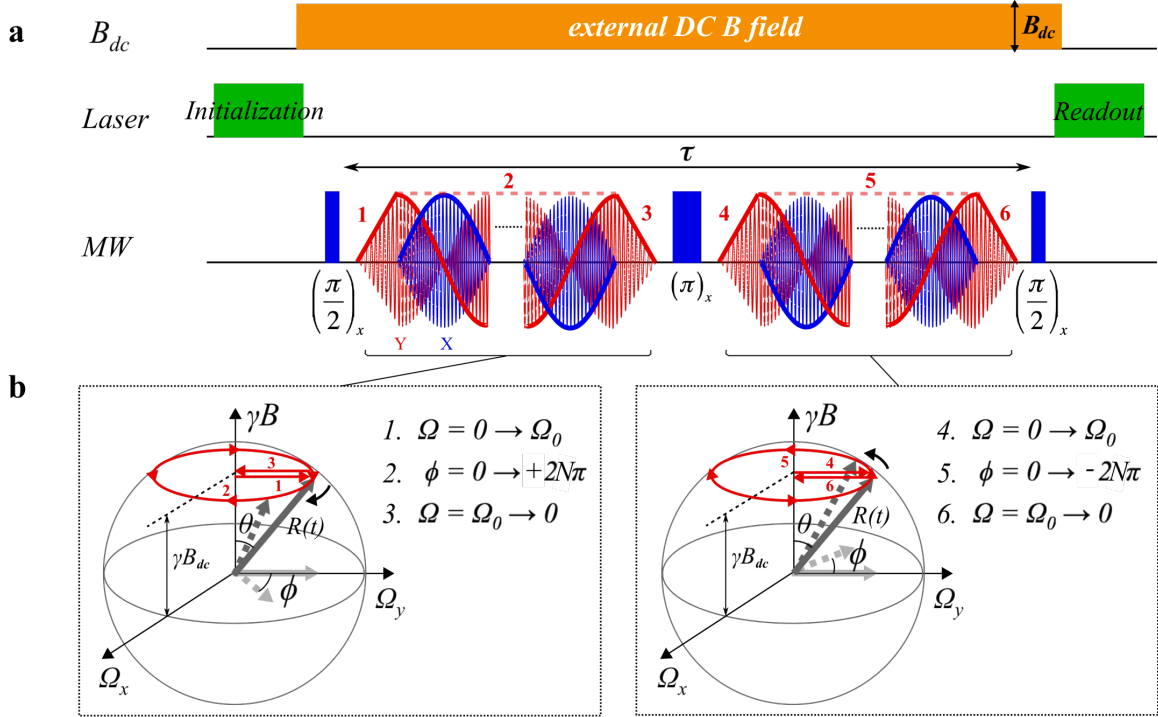
Figure 4-3: **Schematic of geometric-phase magnetometry**. **a**, Pulse sequence for geometric-phase magnetometry with an external dc magnetic field B_{dc} that is varied to acquire a magnetometry curve. A pulsed green laser initializes and reads out the NV spin state. A Berry sequence is applied on top of a Hahn-echo pulse sequence to cancel out the dynamic phase component of total phase accumulation. Resonant $(\pi/2)_x$ and $(\pi)_x$ pulses define a rotating frame, and B_{dc} causes a detuning of the Larmor vector $\vec{R}(t)$ during the Berry sequence. Phase rotation of the Larmor vector $\vec{R}$(t) is controlled by two quadrature bias microwave fields (X : blue, Y : red). One sinusoidal modulation period corresponds to a full rotation ($\phi = 2\pi$) with the winding number $N=1$. N can be controlled by varying the sinusoidal modulation number of two quadrature bias microwaves. **b**, Geometric phase magnetometry. Since $P(B)$ is chirped, data points are distinct on the $(P, dP/dB)$ plane, except for $P = \pm1$. There are finite values of B (black dots) that give the same signal; but one can resolve this degeneracy by also evaluating dP/dB. For $P = \pm1$, once can still resolve the degeneracy by adding a known magnetic field offset.

geometric-phase magnetometry has no dependence on the interaction time . If the magnetic field is below B_{max}, then one can make a geometric-phase magnetometry measurement with optimal sensitivity $\eta \propto \Omega\,N^{-1}\,T^{1/2}$.

4.3.2   Derivation of Geometric-Phase Magnetometry Signal

The geometric-phase magnetometry protocol is characterized by a time-varying Hamiltonian with three control parameters, Rabi frequency Ω, driving field phase ρ, and external magnetic field B:

$$H(t) \;=\; \frac{\hbar}{2}\vec{R}(t)\cdot\vec{\sigma} \tag{4.7}$$

where $\vec{R}(t) \;=\; (\Omega\cos\rho(t),\,\Omega\sin\rho(t),\,\gamma B)$ is the Larmor vector and $\vec{\sigma} \;=\; (\sigma_x,\,\sigma_y,\,\sigma_z)$ are the Pauli matrices. At time $t = t_i$, the NV spin is prepared in a superposition of two levels: $|\psi(t_i)\rangle = \frac{1}{\sqrt{2}}(|+\rangle + |-\rangle)$. If the evolution of the Larmor vector is adiabatic, the instantaneous eigenstates depend on the Larmor vector

$$|+_R\rangle = +\cos\frac{\theta}{2}|+\rangle + e^{i\rho}\sin\frac{\theta}{2}|-\rangle \tag{4.8}$$

$$|-_R\rangle = -\sin\frac{\theta}{2}|+\rangle + e^{i\rho}\cos\frac{\theta}{2}|-\rangle \tag{4.9}$$

where θ is the polar angle between the z-axis and the Larmor vector $\vec{R}(t)$. During the precession, the spin state vector rotates around the Larmor vector. Thus, the spin acquires a dynamic phase ϕ_d, given by

$$\phi_d(t_i, t_f) \;=\; \int_{t_i}^{t_f} |\vec{R}(t')|dt' \;=\; \gamma B(t_f - t_i) \tag{4.10}$$

It is clear from this expression that the dynamic phase depends on the precession time. If this precession is cyclic, namely, $\vec{R}(t_f) = \vec{R}(t_i)$, the state will also acquire a geometric phase ϕ_g. To obtain the expression for the geometric phase, we first calculate the Berry connection: $\vec{A}^{\pm} = i\langle\pm_R|\nabla_\lambda|\pm_R\rangle = -\frac{1\mp\cos\theta}{2\,r\sin\theta}\hat{\rho}$, where $\lambda = (\theta, \rho)$ describes the polar and azimuthal angles for the Larmor vector, and $\nabla_\lambda = r^{-1}\partial_\theta\hat{\theta} +$

$r^{-1}\sin^{-1}\theta\partial_\rho\hat\rho$ is the gradient. Only the ρ component of the Berry connection is nonzero. Then, the geometric phase between two states is given by

$$\phi_g^{\mp}(t_i, t_f) = \oint_C \vec{A}^\pm \cdot d\vec{\lambda} = -\pi N(1 \mp \cos\theta) = \mp\frac{N}{2}\Theta \qquad \mathrm{mod}\, 2\pi \qquad (4.11)$$

The integration is performed along the closed path C with $\rho \in [0, 2\pi N]$, and $\Theta = 2\pi(1 - \cos\theta)$ representing the solid angle subtended by the path C. In the Berry sequence used for geometric-phase magnetometry (Figure 4-3), we insert two Berry pulses between the spin echo pulses. Let us take the entire sequence length to be T. The microwave π rotation pulse about the x axis, $e^{-i\sigma_x\pi/2} = -i\sigma_x$, flips the $|\pm\rangle$ states, giving a minus sign in front of the phase acquired during the second half of the interaction time.

$$\begin{aligned}|\Psi(T)\rangle = &-\frac{i}{\sqrt{2}}e^{-\frac{i}{2}\left[\phi_d\left(0,\frac{T}{2}\right)-\phi_d\left(\frac{T}{2},T\right)+\phi_g\left(0,\frac{T}{2}\right)-\phi_g\left(\frac{T}{2},T\right)\right]}|+\rangle\\ &-\frac{i}{\sqrt{2}}e^{+\frac{i}{2}\left[\phi_d\left(0,\frac{T}{2}\right)-\phi_d\left(\frac{T}{2},T\right)+\phi_g\left(0,\frac{T}{2}\right)-\phi_g\left(\frac{T}{2},T\right)\right]}|-\rangle\end{aligned}$$

$$(4.12)$$

The dynamic phase cancels because $\phi_d(0, T/2) = \phi_d(T/2, T) = \gamma B T/2$. However, the geometric phase can add constructively and be doubled in magnitude by alternating the direction of Larmor vector precession between each pulse: $\phi_g(0, T/2) = \phi_g(T/2, T) = N\Theta$. At the end of the interaction time the spin state is $|\Psi(T)\rangle = -\frac{i}{\sqrt{2}}\left(e^{-iN\Theta}|+\rangle + e^{+iN\Theta}|-\rangle\right)$. The final $\pi/2$-pulse maps the phase into a population difference: $P = \cos(2N\Theta)$. In Figure 4-4 b, the geometric phase signal is measured in a 3D parameter space of Rabi frequency, microwave frequency detuning, and winding number.
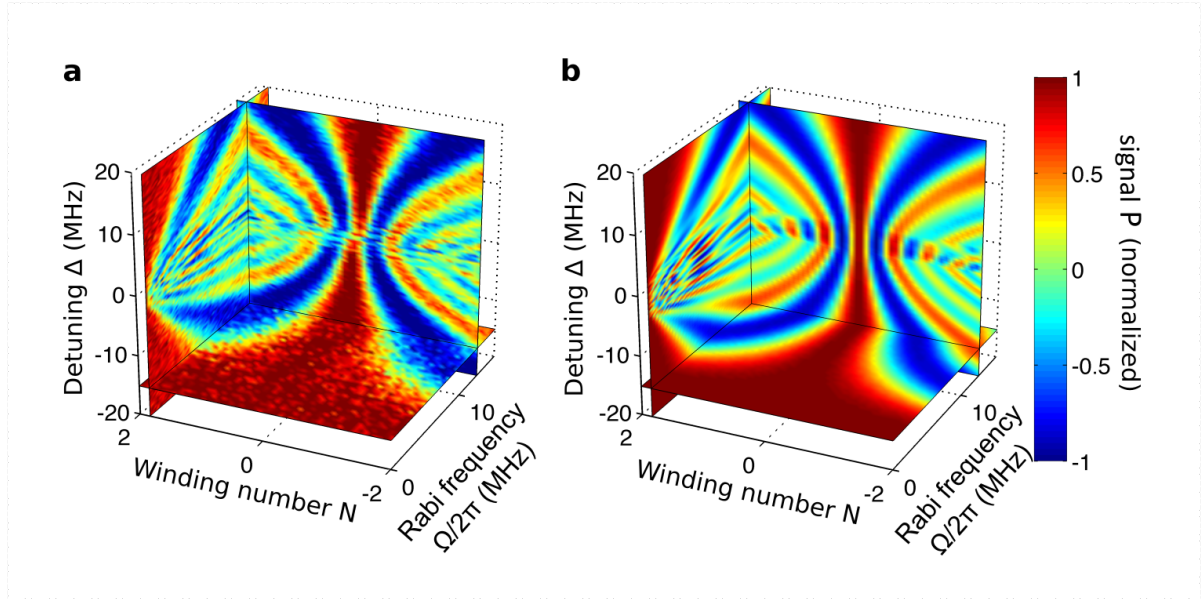
Figure 4-4: **Observation of geometric-phase dependence on control parameters using a single NV spin in diamond**. **a**, Measurement of the cosine of the geometric-phase as a function of Rabi frequency Ω, microwave frequency detuning Δ, and winding number N with a fixed interaction time of $T = 10$ μs. The amplitude of each hyperfine oscillation is extracted by fitting the data along Δ at $N = 2$, $\Omega/2\pi = 12$ MHz to an analytical expression for the geometric-phase signal including the three NV hyperfine transitions. The measured signal is normalized to the mean of these three amplitudes. **b**, Analytical model of the cosine of the geometric phase including the three hyperfine transitions, with the relative amplitudes determined in **a**. The measurement and analytical model agree well.

4.3.3 2π Phase Ambiguity Unwrapped in Geometric-Phase Magnetometry

Again, the geometric phase signal and its derivative are

$$P_g(B) = \cos\left[4\pi N\left(1 - \frac{\gamma B}{\sqrt{(\gamma B)^2 + \Omega^2}}\right)\right]$$

$$\frac{dP_g(B)}{dB} = \frac{4\pi N\gamma\Omega^2}{((\gamma B)^2 + \Omega^2)^{\frac{3}{2}}} \sin\left[4\pi N\left(1 - \frac{\gamma B}{\sqrt{(\gamma B)^2 + \Omega^2}}\right)\right]$$

(4.13)

For any given value of $P_g \neq \pm 1$, there are only finite degeneracies of magnetic field values. They are related by $\frac{\gamma B_m}{\sqrt{(\gamma B_m)^2 + \Omega^2}} = \frac{\gamma B}{\sqrt{(\gamma B)^2 + \Omega^2}} + \frac{m}{2N}$, where m is an integer, which satisfies $|m| < 2N$. This degeneracy can be resolved by measuring dP_g/dB because the slope decreases monotonically with increasing B across a fixed value of P_g, unless $P_g = \pm 1$. This concept can also be presented clearly by plotting the geometric phase signal in 3D (Figure 4-2 b). In contrast to dynamic phase, geometric phase magnetometry measurements, projected onto the $(P_g, dP_g/dB)$ plane, do not lie on a closed 1D curve. All data points except for $(P_g = \pm 1, dP_g/dB = 0)$ are spread across a 2D map and the degeneracy is resolved. Note that even if $P_g = \pm 1$ is measured, one can always add a microwave frequency detuning to look for $P_g \neq \pm 1$. In summary, the geometric phase magnetometry protocol is as follows: (Step 1) Measure the signal P_g and slope dP_g/dB. (Step 2) Identify the corresponding magnetic field value B. If the measured signal and slope leaves an ambiguity, for example $(P_g = \pm 1, dP_g/dB = 0)$, add a microwave frequency offset and repeat the measurement. (Step 3) The steepest slope for high-sensitivity magnetometry is accessible by tuning a microwave frequency. The geometric phase magnetometry signal with three hyperfine transitions is

$$P_g(B) = \frac{1}{3}\sum_{m_I = -1, 0, +1} \cos\left[4\pi N\left(1 - \frac{\gamma B + m_I\omega_{HF}}{\sqrt{(\gamma B + m_I\omega_{HF})^2 + \Omega^2}}\right)\right]$$

(4.14)

The hyperfine transitions introduce a complicated modulation. In particular, degeneracy points can appear at $P_g = \pm 1$. However, since the data points are spread across the two-dimensional $(P_g, dP_g/dB)$ space, the degeneracy can always be resolved by

moving to a different magnetic field value. Although it is difficult to derive an analytical expression to show 2π phase unwrapping in general, exploring the following three cases are sufficient to cover the parameter space:

- For $\gamma|B| \gg \omega_{HF}$, $P_g(B) \sim \cos\left[4\pi N\left(1 - \gamma B/\sqrt{(\gamma B)^2 + \Omega^2}\right)\right] + O(\omega_{HF}^2)$

- For $\gamma|B| \sim \omega_{HF} \ll \Omega$, $P_g(B) \sim \cos\left[4\pi N\left(1 - \gamma B/\Omega\right)\right]\left(1 + 2\cos[4\pi N(1 - \omega_{HF}/\Omega)]\right)$

- For $\gamma|B| \sim \omega_{HF} \geq \Omega$, approximation is difficult. However, this parameter range is of importance for neither large-field-range nor high-sensitivity magnetometry.

4.3.4 Sensitivity and Field Range of Geometric-Phase Magnetometry

For the geometric phase magnetometry, the maximum slope of the curve is given by $|dP_g/dB|_{max} = 4\pi\gamma N\Omega_{-1}$, and then the sensitivity is

$$\eta \approx \frac{1}{\gamma\alpha\sqrt{\beta}}\frac{\Omega\sqrt{T}}{4\pi N} = \frac{1}{\gamma\alpha\sqrt{\beta}}\frac{1}{2A\sqrt{T}} \tag{4.15}$$

where $A = 2\pi N/\Omega T$ is the adiabaticity parameter evaluated at $B \approx 0$. The maximum field-range is defined at the last minimum of the chirped curve: $\phi_g(B_{max}) = 4\pi N(1 - \gamma B_{max}/\sqrt{(\gamma B_{max})^2 + \Omega^2}) = \pi$. By defining a small parameter, $\epsilon \equiv \phi_g/4\pi N \ll 1$, the above equation can be solved in terms of B_{max} to first order:

$$B_{max} \approx \sqrt{2N}\Omega \tag{4.16}$$

4.4 Measurement of Dynamic and Geometric-Phase Magnetometry

4.4.1 Sample and Measurement Calibration

NV Diamond Sample

The diamond chip used in this experiment is an electronic-grade single-crystal cut along the [110] direction into a volume of $4\times4\times0.5$ mm^3 (Element 6 Corporation). A high-purity chemical vapor deposition (CVD) layer with 99.99 % ^{12}C near the surface contains preferentially oriented NV centers. The estimated N and NV densities are 1×10^{15} and 3×10^{12} cm^{-3}, respectively. The spin qubit used in this work consists of the $m_s = +1$ and 0 ground states. Near-resonant microwave irradiation allows coherent manipulation of the ground spin states. The NV spin resonance lifetimes are $T_1 \sim 3$ ms, $T_2 \sim 500$ μs, and $T_2^* \sim 50$ μs.
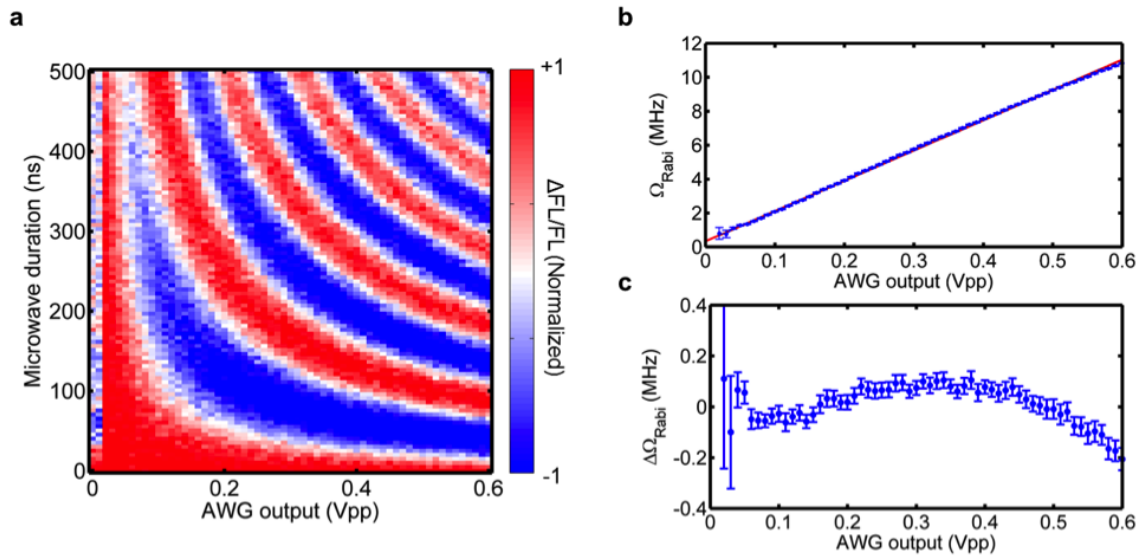
Figure 4-5: **Calibration of NV Rabi frequency as a function of AWG output voltage.** **a**, Normalized Rabi signal, measured as a function of the AWG output voltage and microwave pulse duration. **b**, Reduced Rabi frequency values $\Omega_{Rabi} = \Omega/2\pi$ in units of MHz (blue dots) obtained by fitting data in a to a sinusoidal function at each AWG voltage. Red line is a linear fit of Ω_{Rabi} to voltage. **c**, Residuals of linear fit shown in **b**. The nonlinearity of Ω_{Rabi} is less than 0.2 MHz, which can be attributed to power compression by the I/Q mixer (1 dB compression point is measured to be 1.0 Vpp).
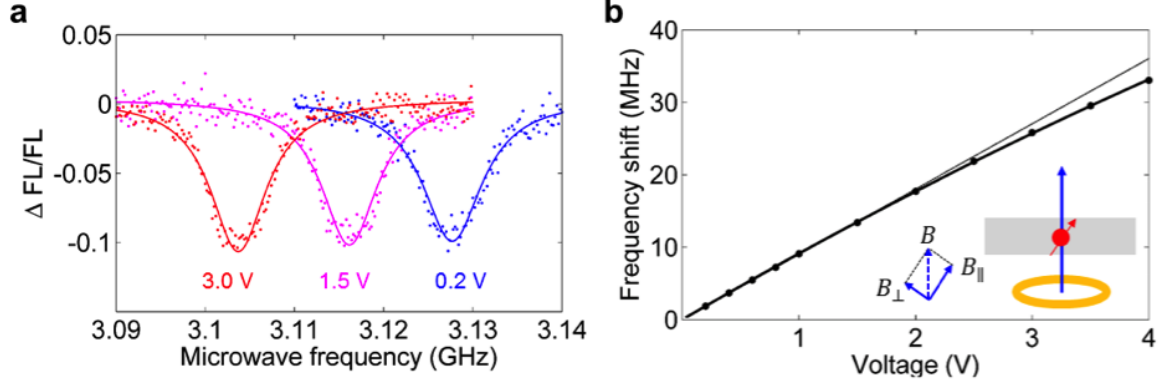
Figure 4-6: **Magnetic field calibration via NV electron spin resonance. a**, Continuous electron spin resonance (ESR) measurement of NV spin transitions in presence of an external magnetic field. First, to split the $m_s = \pm 1$ states, a static field of $B_0 = 93$ G is applied along the [111] NV axis using a permanent magnet, which sets the $|ms = 0, +1\rangle$ resonance peak at 3.13 GHz. Next, an additional external field B is applied using a 40-turn electromagnetic coil placed h = 0.5 mm above the NV center. The coil is also connected to a 150 Ω resistor in series. A high-stability voltage controller provides a high-precision electric current through the coil. An output voltage setting of 3.0 V gives I = 0.02 A, corresponding to a magnetic field of $B = \mu_0 N I / 4\pi h \sim 16$ G in the direction perpendicular to the [100] diamond surface. NV ESR lines are measured for V = 0.2, 1.5, and 3.0 V (color dots). The ESR center frequency is extracted by Gaussian fitting to the date (solid lines). **b**, Absolute value of the ESR frequency shift as a function of applied voltage to the electromagnet (dots). The additional external field B has longitudinal and transverse components with respect to the NV axis: $B = B_\parallel + B_\perp$. The inset diagram indicates a side-view of the magnetometry setup, showing the diamond (gray box), NV axis (red arrow), copper electromagnet (orange circle), and direction of B (blue arrow). The NV spin state frequencies as a function of B are obtained by solving the eigenvalue problem, det(H-λI)=0, where $H/\hbar = (D + \gamma B_0 + \gamma B_\parallel)\sigma_z/2 + \gamma B_\perp \sigma_x/2$ is the two-level system Hamiltonian. Thus, for $\gamma B \ll D$, the measured frequency shift exhibits a quadratic term as a perturbation: $B_\parallel + 2\gamma B_\perp^2/(D + B_0)$ (thick solid curve). For very small B (few gauss), a linear fit gives a calibration of B to the applied electromagnet voltage of $\Delta B/V = 0.50 \pm 0.01$ G V^{-1} (thin line).

Hamiltonian Parameter Control System

The Rabi frequency Ω and phase ρ of the microwave drive field, as well as the applied magnetic field to be sensed B, are key variables of this work. It is thus crucial to calibrate the microwave driving system and magnetic field control system beforehand. Microwave pulses for NV geometric phase magnetometry are generated by mixing a high frequency ($\sim$3 GHz) local oscillator signal and a low frequency ($\sim$50 MHz) arbitrary waveform signal using an IQ mixer. The Rabi frequency and microwave phase are controlled by the output voltage of an arbitrary waveform generator (Figure 4-5). For more details on the microwave setup, please see the Appendix A. An external magnetic field for magnetometry demonstration is created by sending an electric current through a copper electromagnetic coil (4 mm diameter, 0.2 mm thick, $n = 40$ turns, $R = 0.25$ Ohm) placed h = 0.5 mm above the diamond surface. The electric current is provided by a high-stability DC voltage controller. To enable fine scan of the electric current with limited voltage resolution, another resistor with 150 Ohm is added in series. Thus, a DC power supply voltage of 3V approximately corresponds to $I = 0.02$A, which creates an external field of $B = \mu_0 nI/4\pi h \sim 16$ G. One can determine the change of the external magnetic field as a function of DC power supply voltage $\Delta B(V)$ by measuring the shift of the resonance peak Δf in the NV electron spin resonance (ESR) spectrum using $\Delta f = \gamma \Delta B$. The result is $\Delta B/V = 0.50 \pm 0.01 \, G \, V^{-1}$ (Figure 4-6). Joule heating produced by the coil is $P = I^2 R \sim 10^{-4}$ W. The mass and heat capacity of the coil are about 0.15 g and 0.06 J K^{-1}, respectively. Thus, the temperature rise is at most 2 mK s^{-1}. Since the temperature coefficient of the fractional resistivity change for copper is 0.00386 K^{-1} [94], the change of resistance due to Joule heating is negligible.

Numerical Methods for Geometric Phase Simulation

All simulations of NV spin evolution in this work are carried out by computing the time-ordered time evolution operator at each time step.

$$U(t_i, t_f) = \mathcal{T}\left[\exp\left(-i\int_{t_i}^{t_f} H(t)dt\right)\right] = \prod_{j=1}^{N} \exp[-i\Delta t H(t_j)] \tag{4.17}$$

where t_i and t_f are the initial and final time, respectively, $\mathcal{T}$ is the time-ordering operator, Δt is the time step size of the simulation, $N = (t_f - t_i)/\Delta t$ is the number of time step, and $H(t)$ is the time-dependent Hamiltonian (Eq. (1)). In the simulation, we used $\Delta t = 1$ ns step size which is sufficiently small in the rotating frame. The algorithm is implemented with MATLAB®.

4.4.2 Magnetometry Measurement Results

Dynamic-Phase Magnetometry

We implemented both dynamic and geometric-phase magnetometry using the optically addressable electronic spin of a single NV color center in diamond. NV-diamond magnetometers provide high spatial resolution under ambient conditions [15, 13, 95], and have therefore found wide-ranging applications, including in condensed matter physics [96, 97], the life sciences [18, 98, 99], and geoscience [100, 101]. At an applied bias magnetic field of 96 G, the degeneracy of the NV $|m_s = \pm 1\rangle$ levels is lifted. The two-level system used in this work consists of the ground state magnetic sublevels $|m_s = 0\rangle$ and $|m_s = +1\rangle$, which can be coherently addressed by applied microwave fields. The hyperfine interaction between the NV electronic spin and the host ^{14}N nuclear spin further splits the levels into three states, each separated by 2.16 MHz. First, we performed dynamic-phase magnetometry using a Ramsey sequence to illustrate the 2π phase ambiguity and show how the dependence on interaction time gives rise to a trade-off between field range and magnetic field sensitivity. We recorded the NV fluorescence signal as a function of the interaction time T between the two microwave $\pi/2$ pulses (Figure 4-1 a). Signal contributions from the three hyperfine

transitions of the NV spin result in the observed beating behavior seen in Figure 4-7 b. We fixed the interaction time at $T = 0.2, 0.5, 1.0\mu$s, varied the external magnetic field for each value of T, and observed a periodic fluorescence signal with a 2π phase ambiguity (Figure 4-7 c). The oscillation period decreased as the interaction time was increased, indicating a reduction in the magnetic field range (i.e., smaller B_{max}). In contrast, the magnetic field sensitivity, which depends on the maximum slope of the signal, improved as the interaction time increased. For each value of T, we fit the fluorescence signal to a sinusoid dependent on the applied magnetic field and extracted the oscillation period and slope, which we used to determine the experimental sensitivity and field range. From this procedure, we obtained $\eta \propto T^{-0.49(6)}$ and $B_{max} \propto T^{-0.96(2)}$, consistent with expectations for dynamic-phase magnetometry and illustrative of the trade-off inherent in optimizing both η and B_{max} as a function of interaction time (Figure 4-8 a).
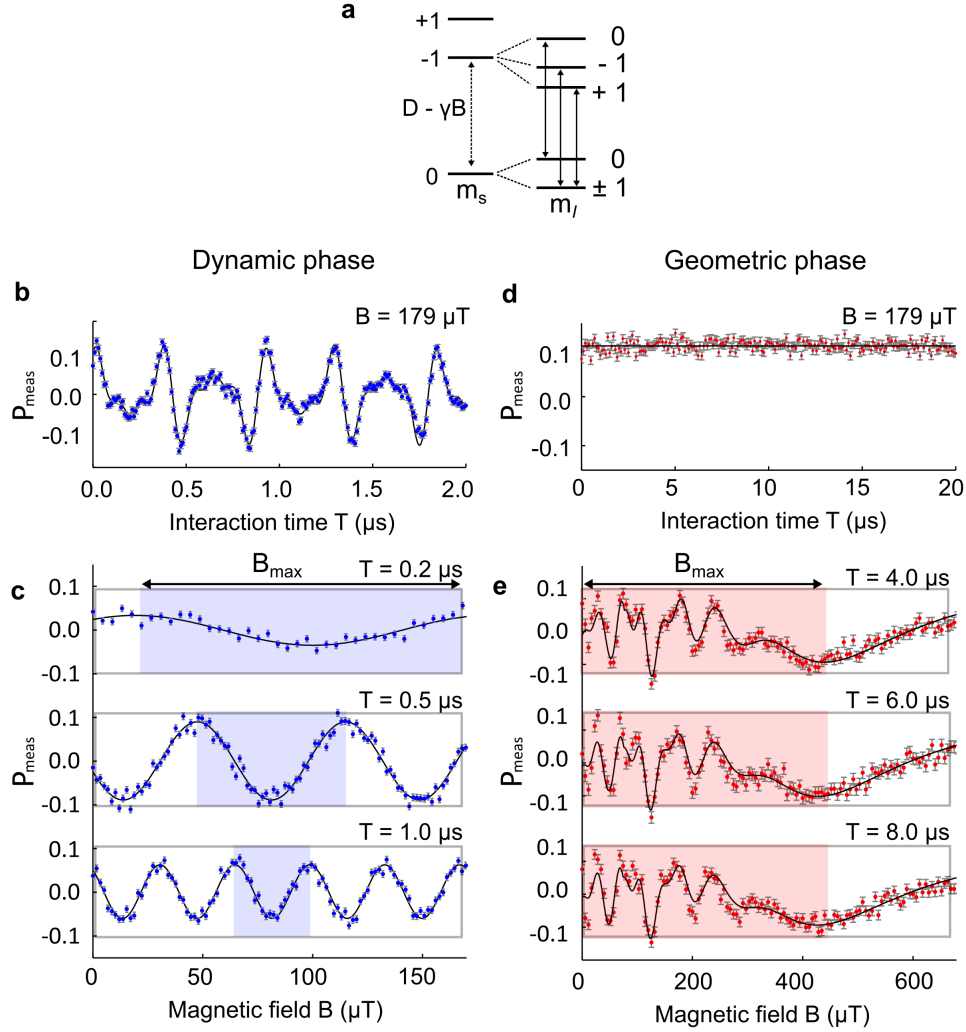
Figure 4-7: **Demonstration of dynamic and geometric-phase magnetometry using a single NV spin in diamond**. **a**, NV electronic spin ($S{=}1$) sublevels $m_s = 0$ and ± 1 with zero-field splitting $D = 2\pi \times 2.87$ GHz. An external magnetic field B introduces Zeeman splitting between the $m_s = \pm 1$ states with gyromagnetic ratio $\gamma = 2\pi \times 28$ GHz/T. $m_s = 0$ and $+1$ define the two-level system used in this work. Hyperfine interactions with the host ^{14}N nuclear spin lead to $m_I = 0, \pm 1$, split by ± 2.16 MHz. **b-e**, Blue and red dots represent measured magnetometry data for dynamic-phase **b,c** and geometric-phase **d,e** protocols, respectively. Vertical axes give the measured optical signal $P_{meas} = k \times (\Delta\text{FL}/\text{FL})$, where $\Delta\text{FL}/\text{FL}$ is the fractional change of NV-spin-state-dependent fluorescence and k is a constant that depends on NV readout contrast. Error bars are 1σ photon shot-noise. Black lines show fits to a model outlined in the main text. Blue and red shaded regions represent maximum magnetic field ranges. Beating due to three hyperfine resonances is evident in **b**. In dynamic-phase magnetometry, the oscillation period decreases as the interaction time increases, indicating a trade-off between sensitivity and field range **c**. Geometric-phase magnetometry signal in **d** shows independence of T. Field range is defined at the last minimum **e**.
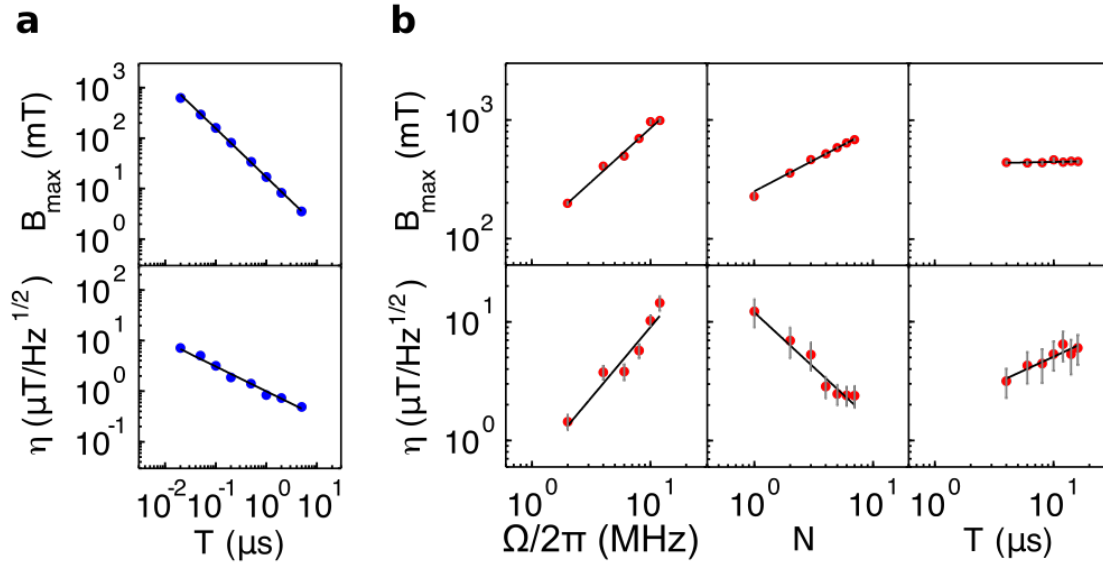
Figure 4-8: **Scaling of sensitivity and field range with three control parameters**. **a**, Measured sensitivity and field range of dynamic-phase magnetometry as a function of interaction time T. The theoretical model predicts $\eta \propto T^{-1/2}$ and $B_{max} \propto T^{-1}$, and the measurement gives $\eta \propto T^{-0.49(6)}$ and $B_{max} \propto T^{-0.96(2)}$. **b**, Measured sensitivity and field range of geometric-phase magnetometry as a function of Rabi frequency Ω, winding number N, and interaction time T. The theoretical model predicts $\eta \propto \Omega^1 N^{-1} T^{1/2}$ and $B_{max} \propto \Omega^1 N^{1/2} T^0$, and the measurements give $\eta \propto \Omega^{1.2(5)} N^{-0.92(1)} T^{0.46(1)}$ and $B_{max} \propto \Omega^{0.9(1)} N^{0.52(1)} T^{0.02(1)}$. **a,b**, Dots indicate data points and lines are linear fits to data.

Geometric-Phase Magnetometry

Next, we used a Berry sequence to demonstrate two key advantages of geometric-phase magnetometry: i.e., there is neither a 2π phase ambiguity nor a sensitivity/field-range trade-off with respect to interaction time. For fixed adiabatic control parameters of $\Omega/2\pi = 5$ MHz and $N = 3$, the observed geometric-phase magnetometry signal P_{meas} has no dependence on interaction time T (Figure 4-7 d). Varying the external magnetic field with fixed interaction times $T = 4.0, 6.0, 8.0\mu$s, P_{meas} exhibits identical chirped oscillations for all T values (Figure 4-7 e), as expected from Equation 4.6. From the P_{meas} data we extract dP_{meas}/dB, which allows us to determine the magnetic field uniquely for values within the oscillatory range, and also to quantify B_{max} from the last minimum point of the chirped oscillation (Figure 4-7e). Additional measurements of the dependence of P_{meas} on the adiabatic control parameters Ω, N, and T yield the scaling of sensitivity and field range: $\eta \propto \Omega^{1.2(5)} N^{-0.92(1)} T^{0.46(1)}$ and $B_{max} \propto \Omega^{0.9(1)} N^{0.52(5)} T^{0.02(1)}$, which is consistent with expectations and shows that geometric-phase magnetometry allows η and B_{max} to be independently optimized as a function of interaction time (Figure 4-10).

Comparison of Sensitivity and Field range

In Figure 4-9, we compare the measured sensitivity and field range for geometric-phase and dynamic-phase magnetometry. For each point displayed, the sensitivity is measured directly at small B (0.01$\sim$0.1 mT), whereas the field range is calculated from the measured values of N and Ω (for geometric-phase magnetometry) and T (for dynamic-phase magnetometry, with T limited by the dephasing time T_2^*), following the scaling laws give above. Since geometric-phase magnetometry has three independent control parameters (T, N, and Ω), B_{max} can be increased without changing sensitivity by increasing N and Ω while keeping the ratio N/Ω fixed. Such smart control allows a 10-fold improvement in geometric-phase sensitivity (compared to dynamic phase measurements) for $B_{max} \sim$1 mT, and a 400-fold enhancement of B_{max} at a sensitivity of $\sim 2\mu$T$\cdot$ Hz$^{-1/2}$. Similarly, the sensitivity can be improved without
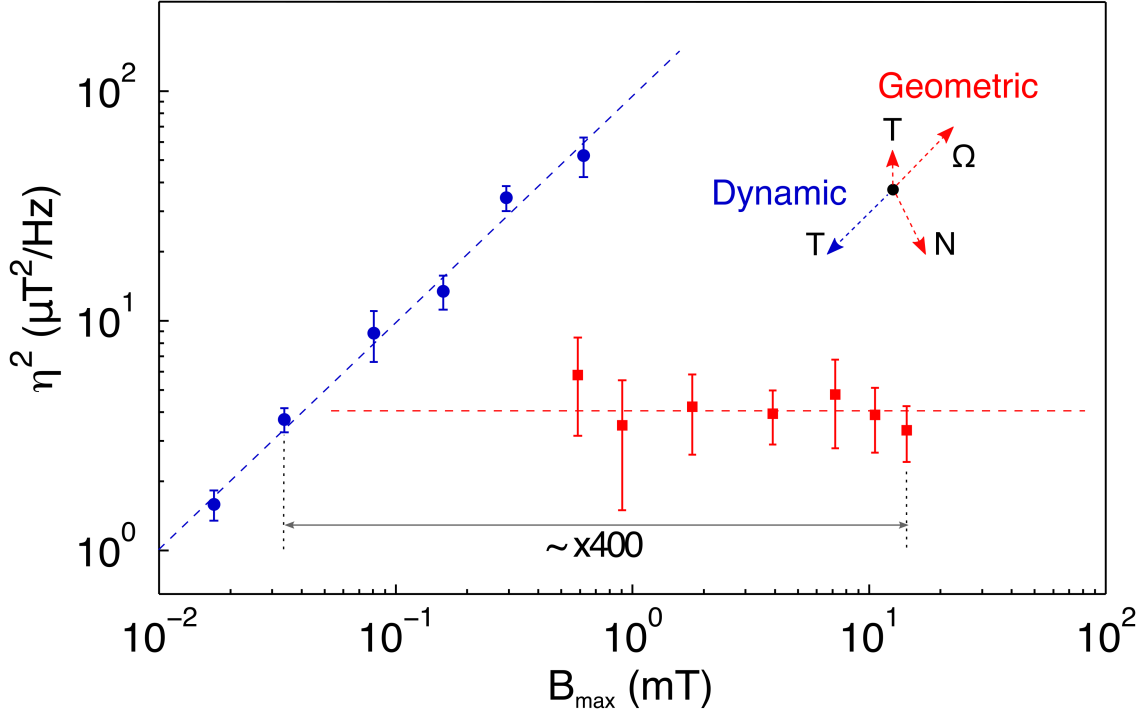
Figure 4-9: **Decoupling of magnetic field sensitivity and maximum field range.** Measured performance of dynamic-phase (blue dots) and geometric-phase (red squares) magnetometry. Dashed lines are linear fits to data. Dashed arrows indicate the orientation of control parameters Ω, N, T as independent vectors on the (η^2, B_{max}) map. Since a Ramsey sequence used for dynamic-phase magnetometry has only a single control parameter (T), the relations for sensitivity $(\eta \propto T^{-1/2})$ and field range $(B_{max} \propto T^{-1})$ are unavoidably coupled as $\eta^2 \propto B_{max}$. In contrast, a Berry sequence used for geometric-phase magnetometry employs all three control parameters, and thus the sensitivity $(\eta \propto \Omega^{-1}NT^{1/2})$ can be chosen independently of the field range $(B_{max} \propto \Omega N^{1/2}T^0)$. For example, larger B_{max} with constant η is obtainable with geometric-phase magnetometry by increasing Ω and N while keeping T and the ratio Ω/N fixed.

changing B_{max} by decreasing the interaction time, with a limit set by the adiabaticity condition ($A \equiv \rho \cdot \sin\theta/2R \approx N/\Omega T \ll 1$).
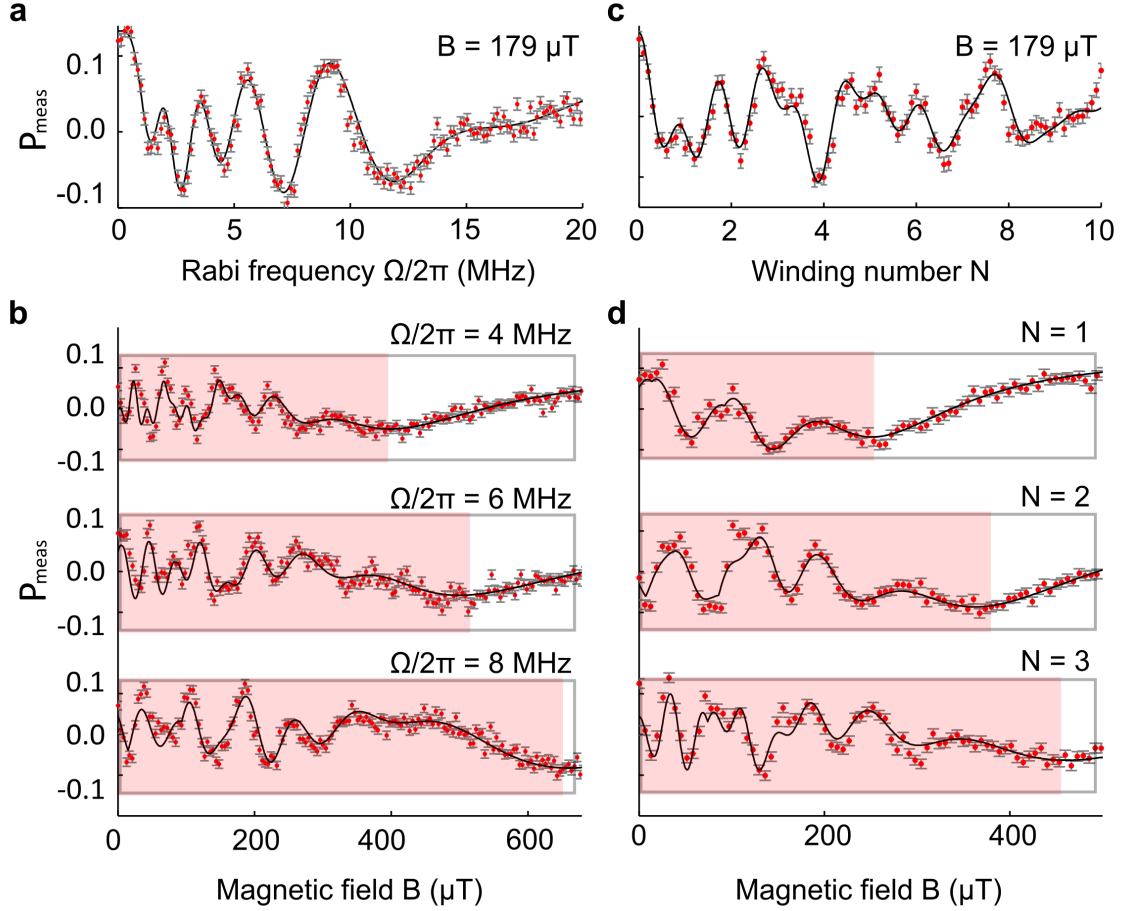
Figure 4-10: **Dependence of geometric-phase magnetometry signal on control parameters**. **a-d**, Geometric-phase magnetometry data (dots) for various values of Rabi frequency Ω and winding number N, as well as applied magnetic field B. Error bars are 1σ photon shot-noise. Black lines are fits of the data to an analytical expression of the geometric-phase signal including the three NV hyperfine transitions. Red shaded regions indicate the maximum magnetic field range defined by the last oscillation minimum. Fixed parameters used in these measurements are: **a**, $B = 179$ μT, $N = 3$, $T = 10$ μs, **b**, $\Omega/2\pi = 4,6,8$ MHz, $N = 3$, $T = 10$ μs, **c**, $B = 179$ μT, $\Omega/2\pi = 5$ MHz, $T = 10$ μs, and **d**, $\Omega/2\pi = 5$ MHz, $N = 1,2,3$, $T = 10$ μs.

4.4.3 Geometric-Phase Magnetometry in Non-Adiabatic Regime

Finally, we explored geometric-phase magnetometry outside the adiabatic limit by performing Berry sequence experiments and varying the adiabaticity parameter by more than two orders of magnitude (from $A \approx 0.01$ to 5). We find good agreement between our measurements and simulations, with an onset of non-adiabatic behavior for $A \geq 0.2$ (Figure 4-11). At each value of the adiabaticity parameter A, we determine the magnetic field sensitivity from the largest slope of the measured magnetometry curve. (The magnetometry curve is the plot of P_{meas} obtained as a function of applied magnetic field B.) To compare with the best sensitivity provided by dynamic-phase magnetometry, we fix the interaction time at $T \approx T_2^*/2$ in the non-adiabatic geometric-phase measurements. We find that the sensitivity of geometric-phase magnetometry improves in the non-adiabatic regime, and becomes smaller than the sensitivity from dynamic-phase measurements for $A \geq 1.0$ (Figure 4-12 a). We recast the sensitivity scaling in terms of the adiabaticity parameter and interaction time, $\eta \propto A^{-1}T^{-1/2}$ and investigated the trade-off between these parameters. (Note that in the non-adiabatic regime the Bloch vector no longer strictly follows the Larmor vector, and thus the sensitivity scaling is not exact.)
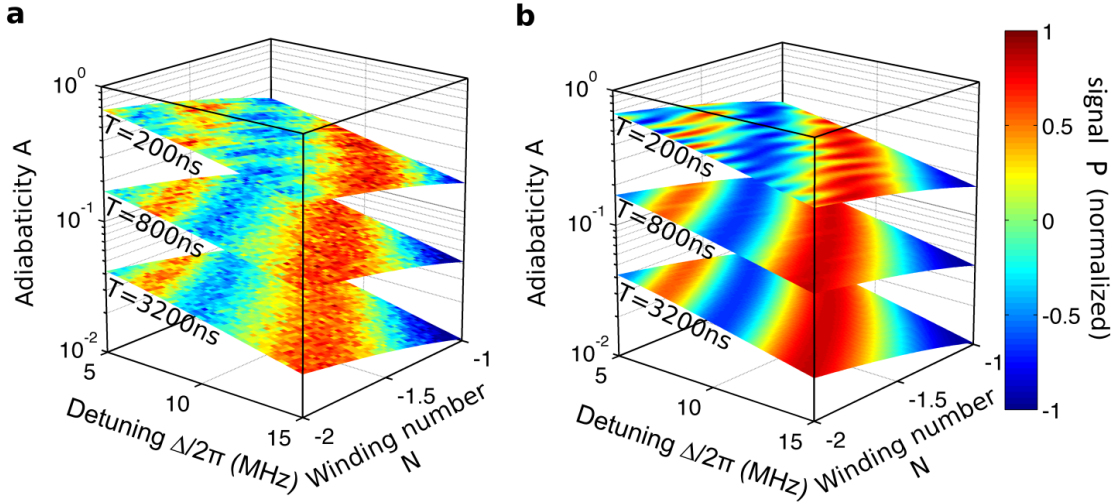
Figure 4-11: **Measurement and simulation of geometric phase signal in the non-adiabatic regime**. **a**, Measurement of the cosine of the geometric-phase as a function of microwave frequency detuning Δ and winding number N with a fixed Rabi frequency of $\Omega/2\pi = 13$ MHz. Three layers represent isochrone planes at $T = 200$, 800, 3200 ns. Vertical axis is adiabaticity $A = \rho \cdot \sin\theta/2R$, where $R = (\Omega^2 + \Delta^2)^2$. The amplitude of each hyperfine oscillation is extracted by fitting the data along Δ at $N = -2$, $T = 3200$ ns to an analytical expression for the geometric-phase signal including the three NV hyperfine transitions. The measured signal is normalized to the mean of these three amplitudes. The analytical expression for the geometric-phase signal assumes adiabaticity and thus is independent of the interaction time T. The data for layers at $T = 3200$ ns and 800 ns ($0.01 < A < 0.2$) look very similar, as expected. However, the layer at $T = 200$ ns ($A > 0.2$) looks distinctly different, indicating that the analytical expression becomes invalid in the non-adiabatic regime. **b**, Simulation of the cosine of the geometric-phase including the three hyperfine transitions with the relative amplitudes obtained in a (see also Methods). The measurement and simulation agree, indicating that the time evolution of the spin state is described deterministically by the Schrödinger equation even in the non-adiabatic regime.

4.5 Geometric Phase Coherence time

4.5.1 Geometric Phase Coherence Theory

If the NV spin qubit interacts with an environment with random noise, the Larmor vector will experience a perturbation:

$$\vec{R}(t) = \vec{R}_0(t) + \delta\vec{R}(t) \tag{4.18}$$

The second term, assumed to be smaller than the first term, is a classical random variable representing fluctuation of the energy splitting due to coupling to environmental noise. When the measurement is repeated, the qubit acquires a different phase each time due to the random noise. Then the system is described by a mixed state using a density matrix, which is obtained by weighting the appropriate probability p for each environmental condition, $\rho(t_f) = p\, U(t_i, t_f)\rho(t_i)U^\dagger(t_i, t_f)$, where $\rho(t_i) = |\psi(t_i)\rangle\langle\psi(t_i)|$ is the initial density matrix at time $t = t_i$ constructed from a pure initial state. In particular, the diagonal elements give the probability of occupying each state, and the off-diagonal elements represent the coherence between these states. Thus, the time-averaged coherence, which can be compared to experiments, is defined as the off-diagonal component of the density matrix averaged over many realizations: $W(t_i, t_f) = |\langle\rho_\pm(t_f)\rangle|/|\langle\rho_\pm(t_i)\rangle|$. For magnetic field sensing, the longitudinal magnetic fluctuations are of main interest as a decoherence source, so that $\delta\vec{R} = (0, 0, \delta R)$ is considered in the following calculations. First, the dynamic phase fluctuation is given by

$$\delta\phi_d(t_i, t_f) = \int_{t_i}^{t_f} \frac{R_z}{R}\delta R\, dt' \tag{4.19}$$

Since we know that the dynamic phase is canceled by an echo operation, we consider only the fluctuation term. Next, to calculate the geometric phase fluctuation, we modify the Berry connection as $A_\rho \to A'_\rho = A_\rho + \partial_\theta A_\rho \delta\theta = \frac{1}{2}\cos\theta + \frac{1}{2}\delta(\cos\theta)$. The second term describes the fluctuation of the polar angle due to the fluctuating
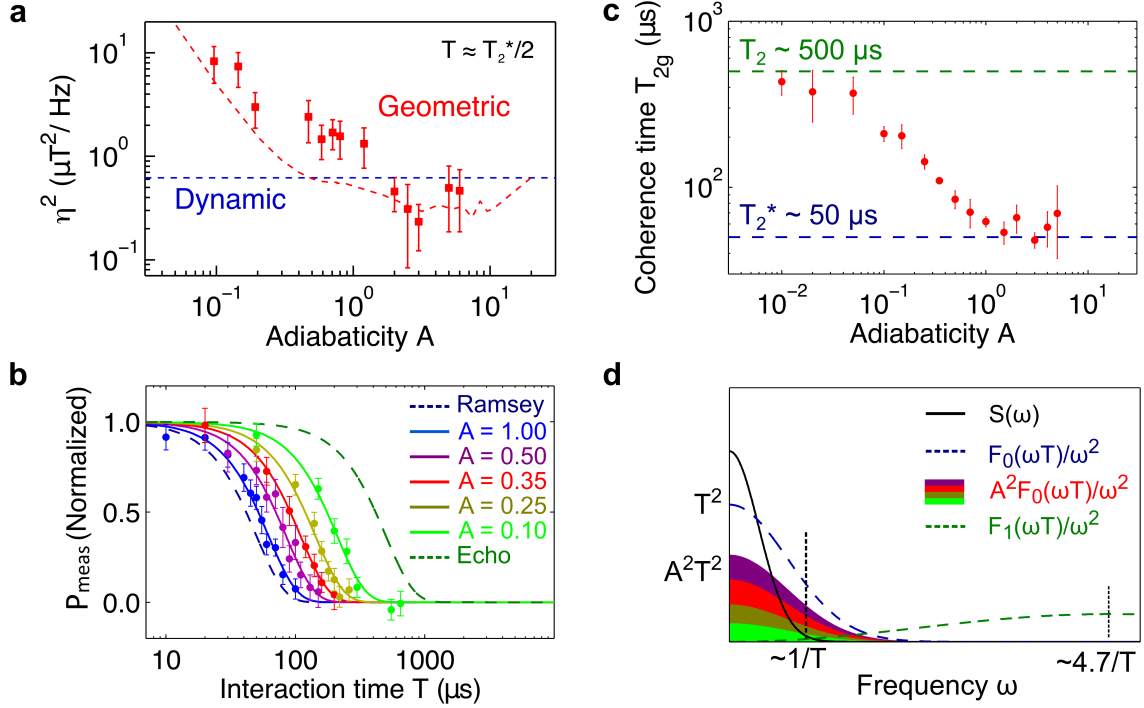
Figure 4-12: **Improved geometric-phase coherence time and sensitivity in nonadiabatic regime.** **a**, Measured geometric-phase magnetic field sensitivity-squared (red squares) plotted against adiabaticity parameter A using a fixed interaction time of $T \approx T_2^*/2$ at which the dynamic-phase Ramsey sequence gives optimal sensitivity (dashed blue line). Dashed red line shows geometric-phase sensitivity lower limit calculated by a numerical simulation assuming maximum signal contrast. The simulation does not include the contrast reduction due to hyperfine modulation. **b**, Measured Berry sequence signal as a function of interaction time T for various adiabaticity parameter values. Color dots are data; solid color lines are exponential fits to data $\sim \exp(T/T_{2g})^2$. Blue and green dashed lines indicate T_2^* and T_2 decay of the dynamic-phase signal measured with a Ramsey and Hahn-echo sequence, respectively. **c**, Measured geometric-phase coherence time T_{2g} as a function of adiabaticity parameter A. Three regimes are observed: (i) For $A < 0.1$, $T_{2g} \sim T_2$, (ii) For $0.1 < A < 1.0$, $T_{2g} \sim 1/A$, and (iii) For $A \sim 1.0$, $T_{2g} \sim T_2^*$. **d**, Qualitative representation of contributions to the decoherence function (Eq. 4.24) in the frequency domain: environmental noise spectral density function $S(\omega)$ (black line); dynamic-phase (spin-echo) filter function $F_1(\omega T)/\omega_2$ (dashed green line); and geometric-phase (Berry sequence) filter function $A^2 F_0(\omega T)/\omega_2$ (filled color area, same color-coding as in **a**), which vanishes in the limit $A \to 0$ and reaches the Ramsey sequence function $F_0(\omega T)/\omega_2$ (dashed blue line) in the limit $A \to 1$.

field δR. The cyclic path is also perturbed due to the fluctuation: $dC_\phi \rightarrow dC'_\phi = Nt^{-1}dt' + \delta Nt^{-1}dt'$. The first term corresponds to the speed of rotation of the Larmor vector, and the second term gives the first order correction due to the fluctuation. The geometric phase fluctuation is then given by

$$
\begin{aligned}
\delta\phi_g(t_i, t_f) &= \frac{N\pi}{t_f - t_i} \int_{t_i}^{t_f} \delta(\cos\theta) dt' = \frac{N\pi}{t_f - t_i} \int_{t_i}^{t_f} \left[\frac{R^2 - R_z^2}{R^3} \right] \delta R dt' \\
&\approx A \int_{t_i}^{t_f} \delta R dt'
\end{aligned}
\tag{4.20}
$$

Here the definition of adiabaticity $A = \dot{\rho} \cdot \sin\theta / 2R$ is used. The final state is

$$
\begin{aligned}
|\Psi(T)\rangle = &-\frac{i}{\sqrt{2}} e^{+\frac{i}{2}\left[\delta\phi_d\left(0,\frac{T}{2}\right) - \delta\phi_d\left(\frac{T}{2},T\right)\right] + \frac{i}{2}\left[\delta\phi_g\left(0,\frac{T}{2}\right) - \delta\phi_g\left(\frac{T}{2},T\right)\right]} |+\rangle \\
&-\frac{i}{\sqrt{2}} e^{-\frac{i}{2}\left[\delta\phi_d\left(0,\frac{T}{2}\right) - \delta\phi_d\left(\frac{T}{2},T\right)\right] - \frac{i}{2}\left[\delta\phi_g\left(0,\frac{T}{2}\right) - \delta\phi_g\left(\frac{T}{2},T\right)\right]} |-\rangle
\end{aligned}
\tag{4.21}
$$

It is important to remember that the direction of revolution is switched between the first and second Berry pulses. Finally, the coherence becomes

$$
W(0, T) = \langle \exp\left[-i\frac{R_z}{R} \int_0^T \delta R f_1(T; t) dt - iA \int_0^T \delta R f_0(T; t) dt \right] \rangle
\tag{4.22}
$$

where $f_n(T; t) = \sum_{k=0}^{n} (-1)^k \Theta(t_{k+1} - t) \Theta(t - t_k)$ is a function that characterizes the pulse sequence, Θ is the Heaviside step function, and $t_0 = 0$, $t_{n+1} = T$. If the noise is assumed to follow a Gaussian distribution with a zero mean $\langle \delta R(t) \rangle = 0$, then the coherence function can be reduced to the two-point correlation function $S(t_i, t_f) = \langle \delta R(t_i) \delta R(t_f) \rangle$ using Wick's theorem: $W(0, T) \sim \langle e^{-i\delta R} \rangle \sim \exp\left[-\langle \delta R \delta R \rangle / 2 \right]$. Hence, the coherence can be analyzed in the frequency domain by use of the spectral density of the noise: $S(\omega) = \int_{-\infty}^{+\infty} dt e^{i\omega t} S(t)$. We also define the decoherence function as $\chi(T) = -\log W(T)$. The cross term between the dynamic and geometric part becomes zero because the sequence functions f_1 and f_0 have opposite parity. Thus,

the decoherence function reduces to two terms

$$\chi_d(T) = \frac{1}{2}\left(\frac{R_z}{R}\right)^2 \int_0^T dt_a \int_0^T dt_b \langle \delta R(t_a)\delta R(t_b)\rangle f_1(T;t_a)f_1(T;t_b)$$
$$= \left(\frac{R_z}{R}\right)^2 \int_0^\infty \frac{d\omega}{\pi} S(\omega)\frac{F_1(\omega T)}{\omega^2} \tag{4.23}$$

$$\chi_g(T) = \frac{1}{2}A^2 \int_0^T dt_a \int_0^T dt_b \langle \delta R(t_a)\delta R(t_b)\rangle f_0(T;t_a)f_0(T;t_b)$$
$$= A^2 \int_0^\infty \frac{d\omega}{\pi} S(\omega)\frac{F_0(\omega T)}{\omega^2} \tag{4.24}$$

Here $F_0(\omega T) = \frac{\omega^2}{2}|\mathrm{FT}(f_0)|^2 = 2\sin^2\left(\frac{\omega T}{2}\right)$ and $F_1(\omega T) = \frac{\omega^2}{2}|\mathrm{FT}(f_1)|^2 = 8\sin^4\left(\frac{\omega T}{4}\right)$ are the filter functions for geometric and dynamic phase evolution in the Berry sequence, respectively.

4.5.2 Measurement of Geometric-Phase Coherence Time

We performed a spectral density analysis to assess how environmental noise leads to both dynamic and geometric phase decoherence, with the relative contribution set by the adiabaticity parameter A, thereby limiting the interaction time T. We take the exponential decay of the NV spin coherence $W(T) \sim exp(-\chi(T))$, characterized by the decoherence function $\chi(t)$

$$\chi(T) = A^2 \int_0^\infty \frac{d\omega}{\pi} S(\omega)\frac{F_0(\omega T)}{\omega^2} + \int_0^\infty \frac{d\omega}{\pi} S(\omega)\frac{F_1(\omega T)}{\omega^2} \tag{4.25}$$

Here, $S(\omega)$ is a spectral density function that describes magnetic noise from the environment; $F_0(\omega T) = 2\sin^2(\omega T/2)$ is the filter function for geometric-phase evolution in the Berry sequence, which is spectrally similar to a Ramsey sequence, with maximum sensitivity to static and low frequency ($\leq 1/T$) magnetic fields; and $F_1(\omega T) = 8\sin^4(\omega T/4)$ is the filter function for dynamic-phase evolution in the Berry sequence, which is spectrally similar to a Hahn-echo sequence, with maximum sensitivity to higher frequency ($\geq 1/T$) magnetic fields.

Figure 4-12 b shows examples of the measured decay of the geometric-phase signal

(P_{meas}) as a function of interaction time T and adiabaticity parameter A. From such data we extract the geometric-phase coherence time T_{2g} by fitting $P_{meas} \sim \exp[-(T/T_{2g})^2]$. We observe four regimes of decoherence behavior (Figure 4-12 c), which can be understood from Equation (4.25) and its schematic spectral representation in Figure 4-12 d. For $A < 0.1$ (adiabatic regime), dynamic-phase evolution (i.e., Hahn-echo-like behavior) dominates the decoherence function $\chi(T)$ and thus $T_{2g} \sim T_2 \approx 500~\mu$s. For $0.1 \leq A < 1.0$ (intermediate regime), the coherence time is inversely proportional to the adiabaticity parameter ($T_{2g} \sim 1/A$) as expected from the scaling in Equation (4.25). For $A \approx 1.0$ (non-adiabatic regime), geometric-phase evolution (i.e., Ramsey-like behavior) dominates $\chi(T)$ at long times and thus $T_{2g} \sim T_2^* \approx 50~\mu$s. For $A \gg 1.0$ (strongly non-adiabatic limit), the driven rotation of the Larmor vector is expected to average out during a Berry sequence (Figure 4-1 b) and only the z-component of the Larmor vector remains. Thus, the Berry sequence converges to a Hahn-echo-like sequence and the coherence time is expected to increase to T_2 for very large A.

4.6   Summary and Outlook

In summary, we demonstrated a new approach to NV-diamond magnetometry using geometric-phase measurements, which avoids the trade-off between magnetic field sensitivity and maximum field range that limits traditional dynamic-phase magnetometry. For an example experiment with a single NV, we realize a 400-fold enhancement in static (DC) magnetic field range at constant sensitivity. We also explore geometric-phase magnetometry as a function of adiabaticity, with good agreement between measurements and model simulations. We find that adiabaticity controls the coupling between the NV spin and environmental noise during geometric manipulation, thereby determining the geometric-phase coherence time. We also show that operation in the non-adiabatic regime, where there is mixed geometric and dynamic phase evolution, allows magnetic field sensitivity to be better than that of dynamic-phase magnetometry. The generality of our geometric-phase technique should make it broadly applicable to precision measurements in many quantum systems, such as

trapped ions, ultracold atoms, and other solid-state spins.

Chapter 5

Observation of Topological Transition in NV Spin Qubit

5.1 Introduction

Topology of quantum systems has gained great interest after the discovery of topological insulators [77, 102, 103]. To understand the topology of a quantum system, topologically invariant numbers, such as the Chern number [104, 105], are introduced as observables. As topological numbers are in general be robust to small perturbations in the system, change of this number represents the topological transition in the quantum system, such as an integer quantum Hall state [76]. In recent years, a theoretical framework, to measure the Chern number in a two-level system was developed [106], and the Chern number transitions from 0 to 1 and 1 to 2 were measured in super conducting qubits [107, 108]. In this chapter, we present results on measuring Chern number transitions in various topologies using the NV center as a spin qubit. Taking advantage of the three hyperfine splitting in the ground state, we show that even with single NV spin qubit we can study topological phases of interacting three qubit system. This new scheme to study topology can be applied to simulate topological phases of conventionally unaccessible Hamiltonians.
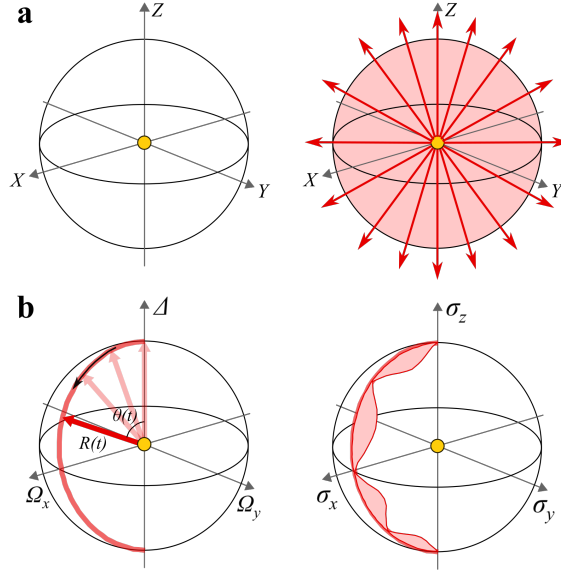
Figure 5-1: **Conceptual picture of topologically invariant number.** **a**, Gaussian sphere in real space with magnetic monopole (yellow dot) at the center. By Gauss's law, total magnetic flux (red arrows) enclosed by the closed surface (red shaded area) is equal to the number of monopoles inside. **b**, In spin qubit quantum system, when the Larmor vector (red arrow) is swept over the Hamiltonian parameter space, non-adiabatic response from the qubit arises (red shade). Integrating this area over the path of Larmor vector sweep is equal to the number of quantum degeneracy points (yellow dot) enclosed by the sweeping parameter sphere.

5.2   Concept of Measuring Chern Number using Spin Qubit

5.2.1   Chern Number Basics

In Chapter 4, we discussed about the Berry phase in a qubit system. By using the Stoke's theorem, we can rewrite the Berry phase in terms of surface integral of the 'Berry curvature' over the surface where Larmor vector's geometric path makes the boundary. If the surface is closed, then the boundary term vanishes, but the in-determinacy of the boundary term which is multiples of 2π appears in the Chern theorem [109]. And according to the Chern theorem, the integral of the Berry cur-vature over a closed manifold is quantized in units of 2π. This number is the called Chern number, and is important for understanding various quantization effects in

quantum physics.

Chern number can be intuitively understood as number of times an eigenstate wraps around a given manifold in Hamiltonian space [109] and yields quantization of the resistance in the integer quantum Hall effect [76, 104, 105]. In quantum system, Chern number is defined as the integral over a closed manifold $\mathbf{S}$ in the Hamiltonian parameter space

$$C_1 = \int_{\mathbf{S}} \mathbf{B} \cdot d\mathbf{S} \tag{5.1}$$

where $\mathbf{B}$ is the Berry curvature [73]. Berry curvature can intuitively thought as a magnetic field with points of ground state degeneracy acting as its sources, i.e. magnetic monopoles [74, 76]. Applying Gauss law for the Berry curvature (magnetic field), C_1 counts the number of degenerate energy eigenvalues enclosed in the parameter manifold $\mathbf{S}$ (Figure 5-1).

5.2.2 Chern Number in Spin Qubit

In *Gritsev et.al.*, the paper proposed to directly measure the Chern number, using a two-level qubit system [106]. The key result is to extract the Berry curvature from the non-adiabatic response of a qubit. Berry curvature equation is given as

$$\langle F_\phi \rangle = -\langle \partial_\phi H \rangle = \langle \phi_0 | F_\phi | \phi_0 \rangle - v_\theta B_{\theta\phi} + O(v^2) \tag{5.2}$$

where the first term is a constant and the second term is the product of parameter ramp speed v_θ and the Berry curvature $B_{\theta\phi}$. This equation can be understood in analogy with the Lorentz force in electromagnetism. Derivation of above equation is discussed in Appendix E. In this section, let us discuss how Berry curvature in above equation can be measured in the experiment. Let us first assume that our time varying Hamiltonian is a spherical version of the gradient. Then the ϕ and θ

components are

$$A_\phi^S = i \frac{1}{r \sin\theta} \langle \psi_0 | \partial_\phi | \psi_0 \rangle = \frac{A_\phi^C}{r \sin\theta}, \tag{5.3}$$

$$A_\theta^S = i \frac{1}{r} \langle \psi_0 | \partial_\theta | \psi_0 \rangle = \frac{A_\theta^C}{r} \tag{5.4}$$

where the Berry curvature vector is given by $\mathbf{B}^S = \nabla \times \mathbf{A}^S$, which in general a complicated expression. However, for our spherical surface of integration, the Chern integral is given by

$$C_1 = \frac{1}{2\pi} \int \mathbf{B} \cdot d\mathbf{S} = \frac{1}{2\pi} \int B_r^S dS_r \tag{5.5}$$

since the surface element is strictly radial:

$$dS_r = \hat{r} dS_r = \hat{r}(r^2 \sin\theta \, d\theta \, d\phi) \tag{5.6}$$

where we have used the standard form of a spherical surface element. Taking the curl in spherical coordinates, the radial component of $\mathbf{B}^S$ is

$$B_r^S = \frac{1}{r \sin\theta}[\partial_\theta(\sin\theta A_\phi^S) - \partial_\phi A_\theta^S] = \frac{1}{r^2 \sin\theta}[\partial_\theta A_\phi^C - \partial_\phi A_\theta^C] = \frac{B_{\theta\phi}^C}{r^2 \sin\theta} \tag{5.7}$$

Plugging equation (5.6) and (5.7) into (5.5), we get the Cartesian expression for C_1. Finally, for our case, the Hamiltonian is cylindrically invariant: we can get the Hamiltonian at arbitrary ϕ from the Hamiltonian at $\phi = 0$ by just rotating the spins by an angle ϕ around the z-axis. Also, the Berry curvature must be cylindrically symmetric, such that $B_{\theta\phi}(\theta, \phi) = B_{\theta\phi}(\theta)$ is independent of ϕ. Therefore, if we plug into the expression for the Chern number, we find

$$C_1 = \underbrace{\frac{1}{2\pi} \int_0^{2\pi} d\phi}_{=1} \int_0^\pi d\theta B_{\theta\phi}(\theta) = \int_0^\pi B_{\theta\phi}(\theta) d\theta \tag{5.8}$$

110

Starting with the Hamiltonian of a single qubit or equivalently spin-1/2 particle in a magnetic field:

$$\mathcal{H}_S = -\frac{\hbar}{2}(H_X \sigma^x + H_Y \sigma^y + H_Z \sigma^z) \tag{5.9}$$

and re-parameterizing it for spherical coordinates, it becomes

$$\mathcal{H}_S(H_r, \theta, \phi) = -\frac{\hbar}{2} H_r(\sin\theta\cos\phi\,\sigma^x + \sin\theta\sin\phi\,\sigma^y + \cos\theta\,\sigma^z) \tag{5.10}$$

Therefore,

$$F_\phi = -\langle \partial_\phi \mathcal{H}(\phi = 0) \rangle = \frac{\hbar}{2} H_r \sin\theta \langle \sigma^y \rangle \tag{5.11}$$

$$\hbar B_{\theta\phi} d\theta = \frac{\hbar}{2} H_r \sin\theta \langle \sigma^y \rangle dt \tag{5.12}$$

$$B_{\theta\phi} = \frac{H_r}{2v_\theta \sin\theta} \langle \sigma^y \rangle \tag{5.13}$$

5.3 Measurement of Landau Zener transition

Before getting into the complicated Chern number measurement directly, let us study
the well understood Landau-Zener transition where a spin qubit is subject to linearly
time-varying Hamiltonian. In two-level system, when qubit is subject to a time-
dependent Hamiltonian such that the energy separation of the two states is a linear
function of time, it undergoes a non-adiabatic process, the Landau-Zener (L-Z) tran-
sition, with probability of transition between the two energy states given by the
Laudau-Zener (L-Z) formula [110, 111]. In this section, we measure this probability
of transition between two energy levels of the NV spin qubit states smoothly sweep-
ing the detuning Δ and Rabi frequency Ω of microwave driving. L-Z formula for this
elliptical trajectory can be semi-analytically calculated. We measure the change of
transition probability by varying the maximum Rabi frequency and total time it takes
to complete the half-cycle of elliptical trajectory. This measurement is an important
stepping stone for the next measurement - the Chern number measurement.

5.3.1 Landau Zener transition in elliptical trajectory

First, let us use a standard approach to discuss the Schrödinger equation with a time-
dependent Hamiltonian $\mathcal{H}(t)$. At each steps of time, there exists a set of instantaneous
basis states $|n(t)\rangle$, which are eigenstates of the instantaneous Hamiltonian

$$\mathcal{H}(t)|n(t)\rangle = \omega_n(t)|n(t)\rangle \tag{5.14}$$

where $\omega_n(t)$ is the eigenenergy. A general state can be described by a linear combi-
nation of eigenstates.

$$|\psi(t)\rangle = \sum_n a_n(t)|n(t)\rangle \tag{5.15}$$

Using the Schrödinger equation, $i\partial_t|\psi(t)\rangle = \mathcal{H}(t)|\psi(t)\rangle$, Equation (5.15) can be rewritten in terms of the basis amplitude as

$$i\partial_t a_m(t) + i\sum_n (t)\langle m(t)|\partial_t|n(t)\rangle = \omega_m(t)a_m(t) \tag{5.16}$$

By applying a Gauge transformation: $a_n(t) \rightarrow a_n(t)\exp[-i\chi_n(t)]$, where

$$\chi_n(t) = \int_{t_i}^t \omega_n(\tau)d\tau \tag{5.17}$$

right hand side of Equation (5.16) can be removed. After fixing the gauge, both hands can be integrated as following.

$$a_n(t) = -\int_{t_i}^t dt' \sum_m a_m(t')\langle n|\partial_{t'}|m\rangle e^{i(\chi_n(t)-\chi_m(t))} + C \tag{5.18}$$

If degenerate states are neglected, $m = n$ gives the Berry phase.

$$\gamma_g = -i\int_{t_i}^t dt'\langle n|\partial_{t'}|n\rangle \tag{5.19}$$

Next, let us consider a two-level system. Two energy levels can be coupled via Hamiltonian in Pauli vector basis.

$$H(t) = \vec{n}\cdot\vec{\sigma} \tag{5.20}$$

Without losing generality, let $\vec{n} = (\Omega(t)\cos\phi, \Omega(t)\sin\phi, \Delta(t))$, where Ω is the Rabi frequency, Δ is the detuning and ϕ is the azimuthal rotation angle. Since $\vec{n}$ is a generalized vector in the Hamiltonian space such that a spin qubit will precess around, let us call it Larmor vector. For simplicity, let $\phi = 0$. The eigenenergies of the system are

$$\omega_\pm(t) = \pm\sqrt{\Omega(t)^2 + \Delta(t)^2} \tag{5.21}$$

Eigenstates can be obtained by solving following equations.

$$i\partial_t|\Psi_+(t)\rangle = \Delta(t)|\Psi_+(t)\rangle + \Omega(t)|\Psi_-(t)\rangle \qquad (5.22)$$

$$i\partial_t|\Psi_-(t)\rangle = \Omega(t)|\Psi_+(t)\rangle - \Delta(t)|\Psi_-(t)\rangle \qquad (5.23)$$

At $t = 0$, set the initial conditions as $|\Psi_-(0)\rangle = |0\rangle$, $|\Psi_+(0)\rangle = |1\rangle$, and amplitudes as $a_1(0) = 0$, $a_0(0) = 1$. Rabi frequency and detuning are swept using a parametric representations.

$$\Omega(t) = \Omega_1 cos\theta \qquad (5.24)$$

$$\Delta(t) = \Delta_1 sin\theta \qquad (5.25)$$

Ω_1 and Δ_1 are maximum Rabi frequency and detuning in the sweep. Here, the parameter $\theta(t)$ is monotonically increasing from 0 to π at a rate of $v_\theta = d\theta/dt$. The transition amplitude is calculated from

$$a_+(\theta) = -\int_0^\theta d\theta' \langle\Psi_+(t)|\partial_{\theta'}|\Psi_-(t)\rangle e^{i[\chi_+(\theta')-\chi_-(\theta')]} + C \qquad (5.26)$$

and transition probability from $|\Psi_-\rangle$ to $\Psi_+\rangle$ is given by $P = |a_+(\theta_f)|^2$. The phase part can be written as

$$\chi_+ - \chi_- = \int_0^{t'} (\omega_+ - \omega_-)dt = \frac{\Delta_1}{v_\theta}E(\theta', k) \qquad (5.27)$$

where E is an incomplete ellipsoidal integral of second kind and $k = \sqrt{(\Delta_1^2 + \Omega_1^2)/\Delta_1^2}$ is the eccentricity. There is no analytical expression for this integral. However, information on scaling of parameters can be extracted by considering asymptotic cases.

$$\text{Adiabatic case } (v_\theta \to 0) : P \to 0$$

$$\text{Diabatic case } (v_\theta \to \infty) : P \sim \Omega_1^2$$

One more important special case is a circular trajectory, where $\Omega_1 = \Delta_1$.

$$P \sim \Omega_1^2 \frac{v_\theta^2}{v_\theta^2 + \Delta_1^2} \tag{5.28}$$

5.3.2 Results of Landau-Zener transition measurements

In the measurement, we used two-level qubit state of $|0\rangle$ and $|+1\rangle$ of the NV spin. $|0\rangle$ is considered as a ground state, and $|+1\rangle$ is considered to be an excited state. In L-Z measurement, both the Rabi frequency and detuning are varied to make an ellipsoidal trajectory as shown in Figure 5-2 b,c, which will also be used in the future topological number measurements. Let us adopt parametric representation for $\Omega(t)$ and $\Delta(t)$ from Equation (5.24) and (5.25), and let θ be a linear function of time.

$$0 < T < T_{ramp} \ , \ \theta(t) = \pi \frac{T}{T_{ramp}} \tag{5.29}$$

T_{ramp} is a ramping time until the Larmor vector travels from $\theta = 0$ to $\theta = \pi$. Microwave pulse sequence which generates this elliptical trajectory is shown in Figure 5-2 c. While fixing the maximum detuning $\Delta_1 = 25$ MHz, there are two parameters that can be varied: (1) the maximum Rabi frequency Ω_1 and (2) T_{ramp} time. First, L-Z transition by varying the maximum Rabi frequency Ω_1 is measured. In this measurement, $T_{ramp} = 1$ μs. The $\langle \sigma_z \rangle$ component of the qubit is measured at various intermediate times T_{meas} (Figure 5-2 c). The result is presented in Figure 5-3 a. The top plot shows the signal contrast as a function of the sweep angle θ. The bottom 2D-plot is a measure of signal contrast as a function of the sweep angle and sweeping maximum Rabi frequency Ω_1. Red and blue region correspond to the $|0\rangle$ and $|+1\rangle$ state, respectively. Figure 5-3 b shows the result of numerical simulation, obtained by computing the time-ordered time evolution operator at each time steps of Δt.

$$U(t_i, t_f) = T\{\exp(-i \int_{t_i}^{t_f} dt H(t))\} = \prod_j \{\exp(-i\Delta t H(t_j)\} \tag{5.30}$$
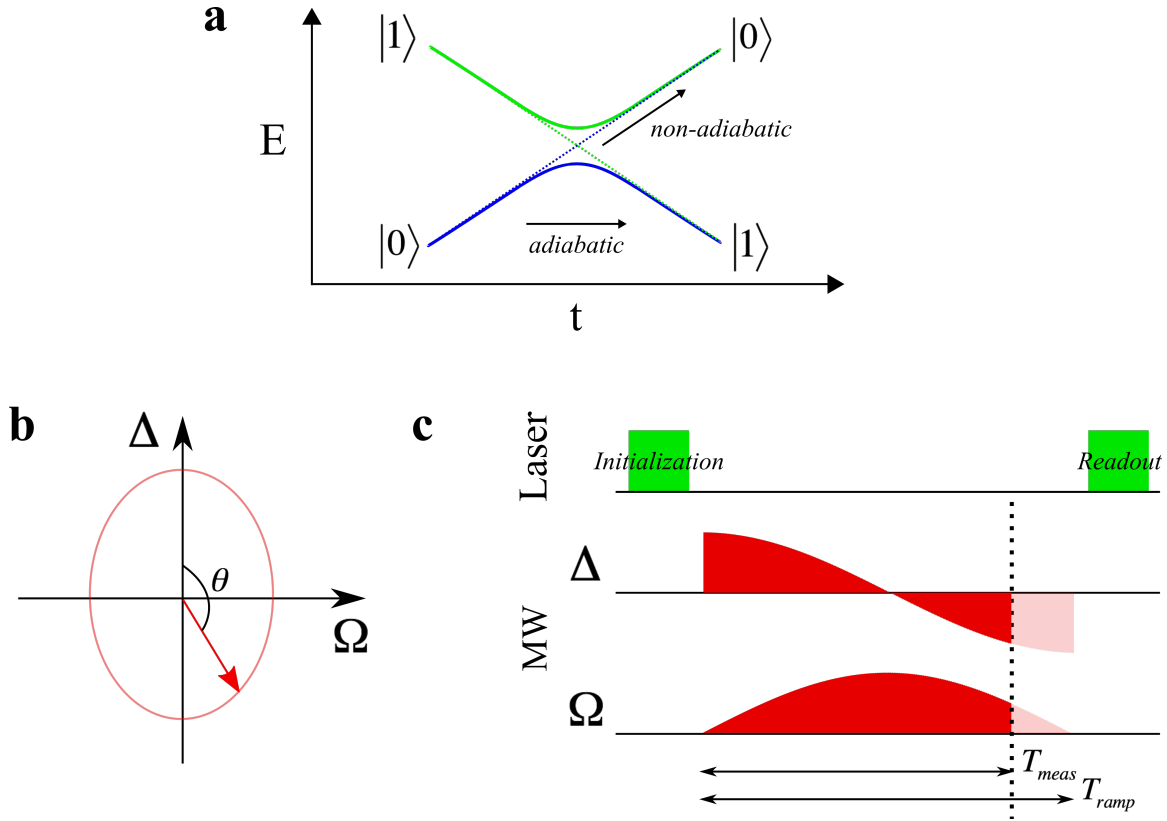
Figure 5-2: **Landau-Zener transition measurement scheme. a**, Diagram of single qubit energy level with time-dependent perturbation. If the change of Hamiltonian over time is low (adiabatic), then by the Adiabatic theorem, spin initialized in ground state will stay in its ground state over the time evolution. However, if the change of Hamiltonian is non-adiabatic, qubit can be excited via Landau-Zener (L-Z) transition. **b**, Schematics of Larmor vector sweeping trajectory in Hamiltonian parameter space with Rabi frequency Ω and detuning Δ. Change of Larmor vector over time will induce the L-Z transition. **c**, Pulse sequence to create Larmor vector sweep. Detuning is swept as $\Delta = \Delta_1 \cos\theta(t)$ and Rabi frequency is swept as $\Omega = \Omega_1 \sin\theta(t)$, where $0 < \theta < \pi$. Total sweep time is given by T_{ramp} time, and by varying T_{meas}, we measure the qubit spin state via green laser.
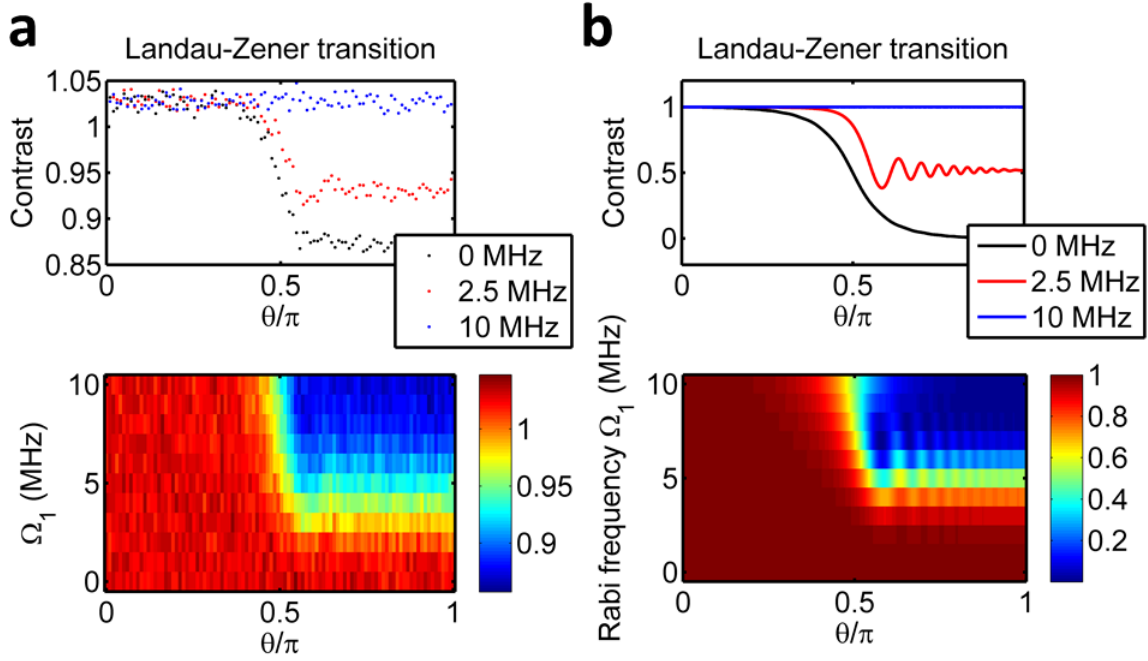
Figure 5-3: **Landau-Zener transition measurement by sweeping Rabi frequency.** **a**, Measuring $\langle \sigma_z \rangle$ of the qubit by sweeping θ. Ω_1 was varied from 0 to 10 MHz. $T_{ramp} = 1$ μs (slow change), $\Delta_1 = 25$ MHz were fixed. Lower figure is $\langle \sigma_z \rangle$ 2D plot by varying θ and Ω_1. Red and blue regions are $|0\rangle$ and $|+1\rangle$ states respectively. Upper figure is a cross sectional plot of the lower figure when $\Omega_1 = 0$, 2.5 and 10 MHz. Let's call the Larmor vector velocity projected in z-axis as L-Z velocity. For large L-Z velocity ($\Omega_1 > 3$ MHz), qubit state remained in its ground state ($|0\rangle \to |+1\rangle$), however, for small $\Omega_1 < 3$ MHz, we observed L-Z transition into excited states ($|0\rangle \to |0\rangle$). At $\Omega_1 \sim 5$ MHz, ripple structure starts to appear, and this is when the transition starts to happen. **b**, Numerically simulated L-Z transitions. We confirmed that the simulation matches with our measurement.
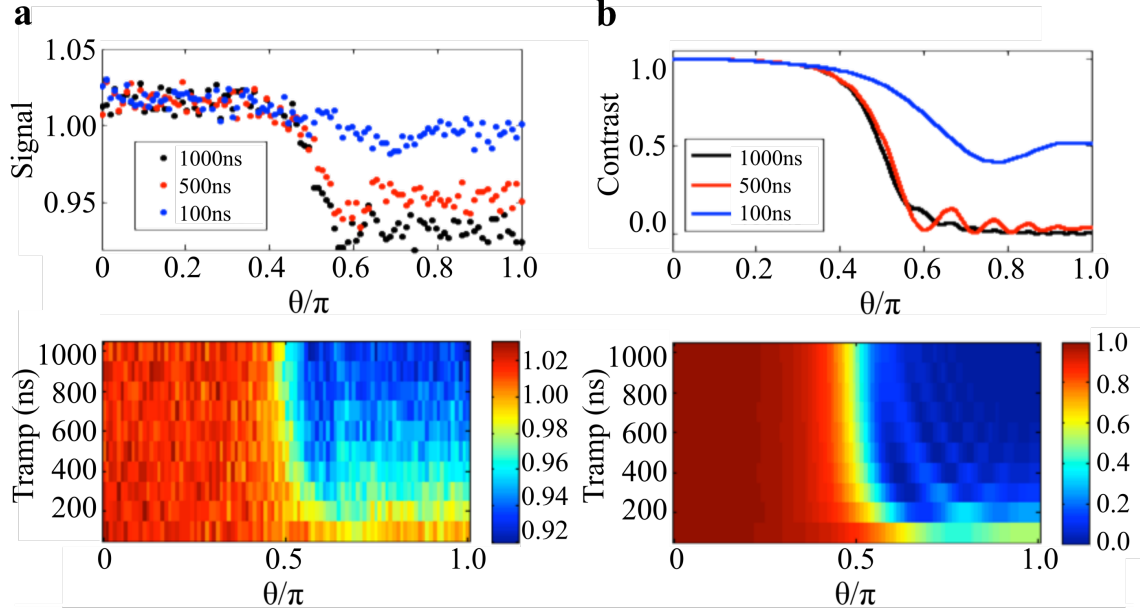
Figure 5-4: **Landau-Zener transition measurement by sweeping T_{ramp}. a**, Measuring $\langle \sigma_z \rangle$ of the qubit by sweeping θ. T_{ramp} was varied from 0 to 1000 ns. Ω_1 = 10 MHz, Δ_1 = 25 MHz were fixed. Lower figure is $\langle \sigma_z \rangle$ 2D plot by varying θ and T_{ramp}. Red and blue regions are $|0\rangle$ and $|+1\rangle$ states respectively. Upper figure is a cross sectional plot of the lower figure when T_{ramp} = 100, 500 and 1000 ns. For fast L-Z velocity ($T_{ramp} < 200$ ns), qubit is in diabatic case, therefore L-Z transition happens (ground state $|0\rangle$ to excited state $|0\rangle$) with rate $\sim \Omega_1^2$. However, for slow L-Z velocity $T_{ramp} > 500$ ns, we observed suppressed L-Z transition. **b**, Numerically simulated L-Z transitions. We confirmed that the simulation matches with our measurement.

In the simulation, the time-ordering operator T is very important because the Hamiltonian at each time point doesn't commute with each other; a qubit Hamiltonian is described by $SU(2) \sim U(1) \times SO(3)$, and two successive rotation operators in three-dimension don't commute. In equation (5.30), second equality holds in the limit of $\Delta t \to 0$. Here, $\Delta t = 1ns$ is chosen to be $\Delta t \ll 1/\Omega_1, 1/\Delta_1$. This approach is still more accurate than taking the first few terms of Magnus expansion or Dyson series. In Figure 5-3, both measurement and simulation show that for fixed T_{ramp}, the L-Z transition doesn't happen for large Rabi frequency, and transition rate increases as Rabi frequency gets small. For fixed T_{ramp} and Δ_1, smaller Rabi frequency corresponds to larger L-Z velocity, v_θ in z-axis, therefore, L-Z transition probability gets larger. In Figure 5-3 a, at $\Omega_1 \sim 5$ MHz, ripple structure starts to appear, and this

is when the transition starts to happen. Next, we measured L-Z transition by varying the T_{ramp} with fixed Ω_1 and Δ_1. This measurement is the same as varying the Larmor vector velocity in z-axis. With $\Delta_1 = 25$ MHz and $\Omega_1 = 10$ MHz fixed, T_{ramp} is swept from $0.1\mu s$ to $1\mu s$ with $0.1\mu s$ of incrementation. In Figure 5-4 a, top plot shows the signal contrast as a function of the sweep angle θ. The bottom 2D-plot is a measure of signal contrast as a function of the sweep angle and the ramp time. The red and blue region correspond to the $|0\rangle$ and $|1\rangle$ state, respectively. Figure 5-4 b shows the result of numerical simulation. For short T_{ramp} time, i.e. larger L-Z velocity, higher probability of transition is observed, and this is consistent with the equation (5.28). There is a significant change in transition probability at $T_{ramp} = 300$ ns from both measurement and simulation results. This indicates that for $T_{ramp} > 300$ ns, time-evolution of the qubit almost follows the adiabatic passage.

5.4   Measurement Calibration for Chern number measurement

5.4.1   Control Pulse Calibration via Dynamic State Preparation

To determine the topological invariant number associated with a topological phase, precise state tomography measurements in all three directions should be performed. The first step toward this goal is to measure $\langle \sigma_z \rangle$ after an elliptic or spherical manipulation of a spin qubit. In previous section, we reported observation of the Landau-Zener transition during the manipulation and confirmed that the transition probability was dependent on the Rabi frequency and the ramp time. The next step, is to measure $\langle \sigma_z \rangle$ under various topological cases, which can be transited back and forth by changing the offset microwave detuning, Δ_2 (Figure 5-5 a). Using this result as a springboard, we can move onto the measurement of all three components of the spin and extract the Chern number.
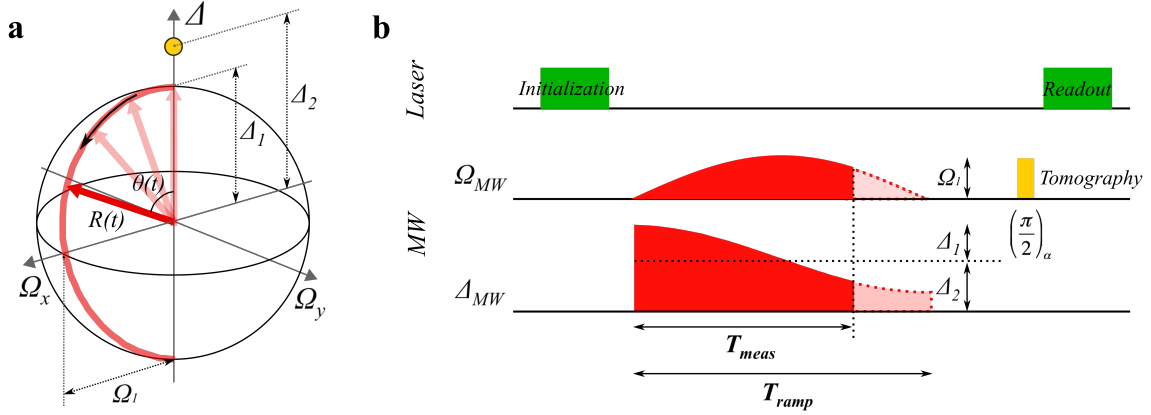
Figure 5-5: **Dynamic State Preparation Schematics. a**, Red pulse, the control pulse, indicates Larmor vector sweep in spherical Hamiltonian parameter space. Z-axis is a detuning, Δ, and X,Y-axis are the Rabi frequencies, Ω_x and Ω_y, same construction as in geomatric phase magnetometry. Δ_1 is the maximum detuning in $\Delta = \Delta_1 \sin \theta(t) + \Delta_2$, and Ω_1 is the maximum Rabi frequency in $\Omega = \Omega_1 \cos \theta(t)$. Here, we assume spherical sweep, therefore, $\Delta_1 = \Omega_1$. Yellow dot represents the quantum degeneracy point (resonance point), and Δ_2 is an offset detuning, which is from the degeneracy point to the center of parameter sweep sphere. Larmor vector $\vec{R}(t)$ (red arrorw) is swept with $\theta(t)$ from 0 to π, which is along the path on the parameter sweep sphere. **b**, Microwave pulse sequence to generate spherical parameter sweep in **a**. After the qubit is initialized into ground state, microwave frequency with detuning is swept as $\Delta = \Delta_1 \sin \theta(t) + \Delta_2$ with modulated amplitude of $\Omega = \Omega_1 \cos \theta(t)$ (Rabi frequency). At each $\theta(t)$, $\langle \sigma_x \rangle$, $\langle \sigma_y \rangle$ and $\langle \sigma_z \rangle$ are measured (green readout pulse) at T_{meas} with tomography pulse (yellow).

Let us first look at the control Hamiltonian of a spin qubit,

$$H = \vec{H}(t) \cdot \vec{\sigma} \tag{5.31}$$

where $\vec{\sigma} = (\sigma_x, \sigma_y, \sigma_z)$ are the spin$-1/2$ Pauli matrices in Bloch sphere, and $\vec{H}(t) = (H_X, H_Y, H_Z)$ is a control magnetic field, which constructs the Hamiltonian parameter space. We can experimentally realize this Hamiltonian parameter space by microwave pulses. H_X and H_Y correspond to the Rabi frequency, Ω and H_Z is the detuning from the resonance frequency, Δ. The eigenenergy of the states are given by $E_{\pm}(t) = \pm\sqrt{H_X^2 + H_Y^2 + H_Z^2}$, and the eigenstates are obtained by solving the Shrödinger equation. As a Hamiltonian path for measuring topological invariant number, we choose a spherical trajectory in the Hamiltonian space of $(\Omega_X, \Omega_Y, \Delta)$. To illustrate the dynamical state preparation using this spherical trajectory, we use the spherical coordinates (θ, ϕ). Using this parametric representation, we can write the measurement sequence as follows

$$H_X = \Omega_1 \sin\theta \cos\phi, \quad H_Y = \Omega_1 \sin\theta \sin\phi, \quad H_Z = \Delta_1 \cos\theta + \Delta_2, \tag{5.32}$$

where $\theta(t) = \pi t/T_{ramp}, 0 < t < T_{meas}$ and $\Omega_1 = \Delta_1$. Let us call this as control pulse sequence. From the azimuthal symmetry, we can fix $\phi = 0$. This spherical trajectory starts at the north pole when $t = 0$ and ramps along the $H_Y = 0$ meridian with constant velocity $v_\theta = d\theta/dt$ until it reaches the south pole at $t = T_{ramp}$. Here, let us define adiabaticity parameter

$$A = \frac{\Omega_1 T_{ramp}}{2\pi} \tag{5.33}$$

which is a normalized factor to determine how fast the Larmor vector changes over time when we vary both T_{ramp} and Ω_1. First, to realize the motion on a spherical manifold, the control magnitude $|H| = \Omega_1 = \Delta_1$ is fixed. In the adiabatic limit, the state would remain in the instantaneous ground state, with the spin vector parallel to the direction of the control field, following the meridian. In this measurement, the
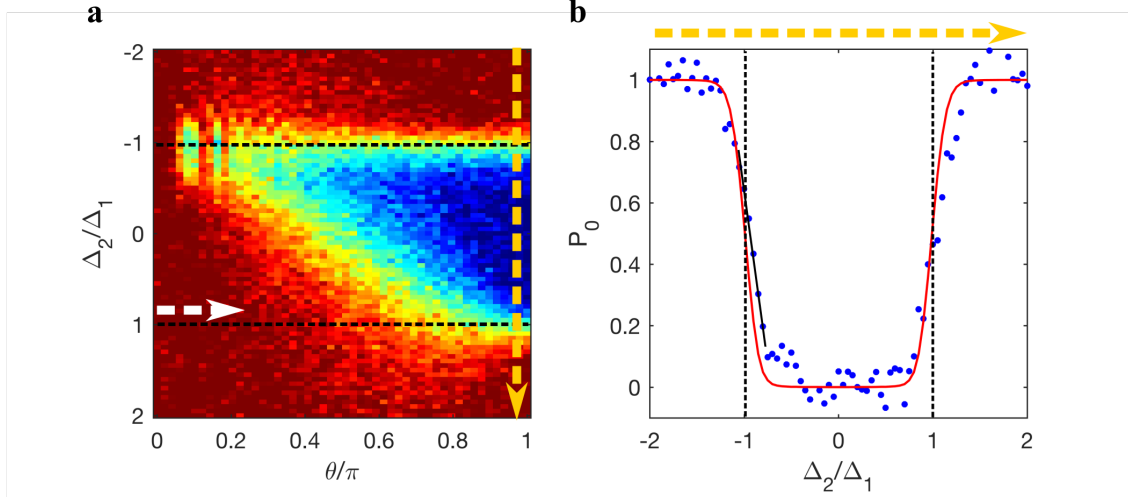
Figure 5-6: **Projection measurement $\langle\sigma_z\rangle$ of spin qubit after dynamic state preparation. a**, $\langle\sigma_z\rangle$ of spin qubit after dynamic state preparation. The horizontal axis is an angle θ/π sweep and the vertical axis is Δ_2/Δ_1, the sweep of degeneracy point. Red region is $|0\rangle$ and blue region is $|+1\rangle$. Moving in the horizontal direction (white dashed arrow) corresponds to the adiabatic passage. The vertical direction at $\theta/\pi \sim 1$ (yellow dashed arrow) indicates the transition. **b**, The cross section at $\theta/\pi \sim 1$. Y axis is the probability of spin state being in $|0\rangle$. Red solid line is simulation, blue dots are measurement, black line is a linear fit. The sensitivity obtained from this measurement (slope of the black line) is ~ 12 μT Hz$^{-1/2}$.

z component of the spin is determined at each point in time by pausing the ramp and performing projection measurement $P = |0\rangle\langle 0|$. There are two parameters varied during the measurement. The angle θ is swept from 0 to π in $T_{ramp} = 3000$ ns, and the Δ_2/Δ_1 is swept from -2 to +2 where $\Delta_1 = 10$ MHz. The detuning offset Δ_2 is introduced by changing the signal generator carrier frequency (for more details, see Appendix A). The result is shown in Figure 5-6.

By taking a cross section at $\theta \sim \pi$, we observed a transition of $|0\rangle$ to $|+1\rangle$, where $|0\rangle$ indicates spin up and $|+1\rangle$ indicates spin down when we project spin$-1/2$ manifold. In following text, we will project $|m_s = 0\rangle$ into spin up ($\langle\sigma_z\rangle = +1$) and $|m_s = +1\rangle$ into spin down ($\langle\sigma_z\rangle = $ -1) to have sub-manifold of spin$-1/2$ from spin-1. The measured transition is less sharp than what the simulation predicts mainly because of the hyperfine coupling to the host nitrogen nuclear spin. The DC-field sensitivity obtained from this measurement is $\sim$12 μT Hz$^{-1/2}$. The estimation is obtained by
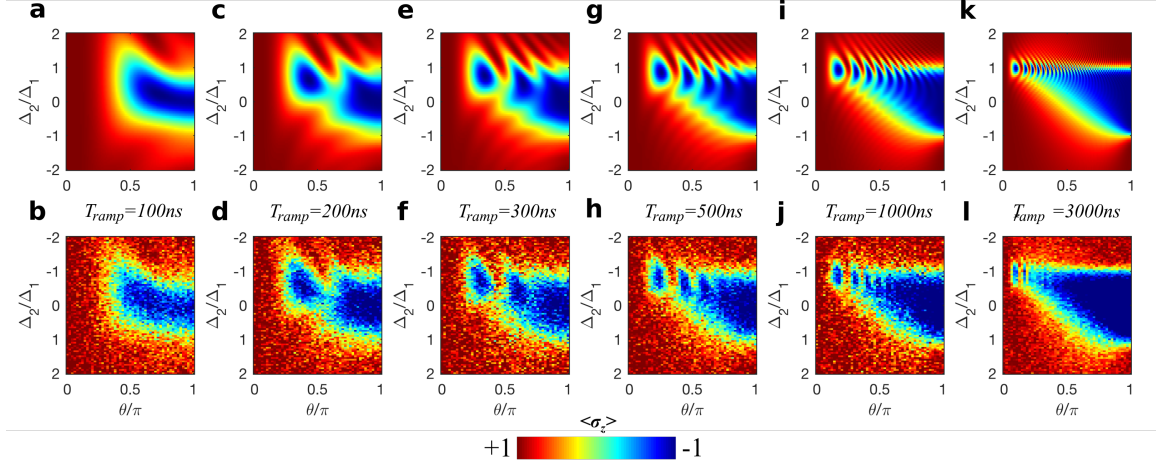
Figure 5-7: **Measurement and simulation of dynamic state preparation by varying T_{ramp}. b,d,f,h,j,l**, The bottom row is experiment and the **a,c,e,g,i,k**, top row is simulation. From the left, T_{ramp} is changed from 100 ns to 3000 ns. For each plot, we show the contrast of projection measurement as a function of state angle theta in the horizontal direction and the Δ_2/Δ_1 ratio in the vertical direction.

using the slope $= dS/d(H_0/H_r) \sim 3.31$, $d(H_0/H_r)/dB = 1/10$MHz - 1, std(error) $= 0.09$, $T_{tot} = 1.5$ s.

Next, we can vary the ramp speed v_θ. This can be tuned by varying $T_{ramp} = 100, 200, 300, 500, 1000$ and 3000 ns. The result is compared with the simulation (Figure 5-7). The bottom plots (Figure 5-7 b,d,f,h,j,l) show the measurement of signal contrast as a function of the sweep angle. The top plots (Figure 5-7 a,c,e,g,i,k) are simulation results. The red and blue region correspond to the $|0\rangle$ and $|+1\rangle$ state, respectively. The simulation was carried out by calculating the time-ordered time evolution operator at each time steps, and we confirmed it matched with the measurement.

5.4.2 Tomography Pulse Calibration

To measure the non-adiabatic response from a spin qubit while it travels the spherical trajectory, it is important to perform a good tomography measurement; having correct phase matching scheme and pulse duration to precisely measure $\langle \sigma_x \rangle$ and $\langle \sigma_y \rangle$ components. General scheme of control pulse to create spherical trajectory is a sine

enveloped chirped signal, since we sweep both detuning and Rabi frequency. For the chirped signal, it is not trivial how to define a certain phase in an arbitrary time, because during the control pulse is applied, qubit spin is no longer in a resonance rotating frame due to the detuning.

To match the relative phase, we connected the tomography pulse directly to the control pulse after a given time T_{meas} (Figure 5-8). Assuming that for control pulse is creating the Larmor vector, $\vec{R}(t)$ to rotate along Ω_y, then continuing tomography pulse with *in phase* will still be a Larmor vector pointing to Ω_y (Figure 5-8 a inset), which we then can rotate for $\pi/2$ duration to read out $\langle \sigma_x \rangle$ component of a qubit. If the tomography pulse had *off phase* of $\pi/2$, then this will create Larmor vector pointing Ω_x (Figure 5-8 b inset), which we then can rotate for $\pi/2$ duration to read out $\langle \sigma_y \rangle$ component of a qubit. To confirm if this tomography pulse scheme works and to check if there is any dynamic phase noise leaks into the measurement, we swept only the Rabi frequency, without any detuning in the parameter space, and performed tomography measurements. Tomography pulse Rabi frequency was set to 10 MHz, and $T_{ramp} = 400$ ns (details on choosing this particular T_{ramp} will be discussed in later section). Theoretically, when we increase our Larmor vector $\vec{R}(t)$ in Ω_x, then spin qubit will fully precess around $\vec{R}(t)$ in y-z plane. Therefore, $\langle \sigma_x \rangle$ would be a decaying oscillation and $\langle \sigma_y \rangle$ would be a flat signal, if there is no dynamic phase contribution to the measurement. This was indeed what we measured (Figure 5-8 c,d). For measuring Chern number, careful measurement on $\langle \sigma_y \rangle$ is important, and we measured dynamic phase noise contribution to be highly suppressed. Note that this tomography pulse calibration process is much simpler than that of superconducting qubit system [107, 108]. Due to the presence of finite inharmonicity in SCQ, they had to go through more complicated calibration process. Since the NV spin qubit system has only two levels under an external bias magnetic field, we can forget about leakage to other states, which gives fidelity advantage of using NV center for quantum simulations.
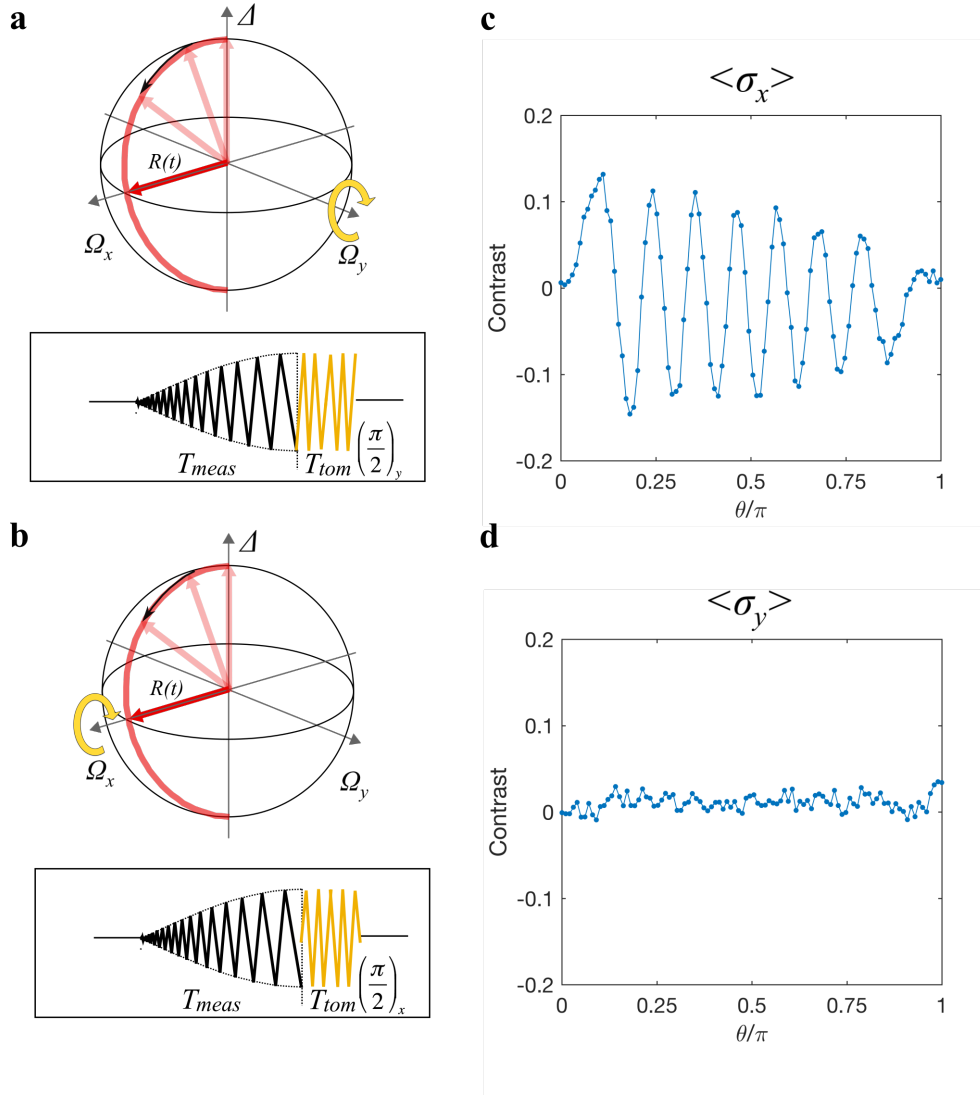
Figure 5-8: **Tomography pulse matching scheme. a**, Tomography pulse for measuring $\langle\sigma_x\rangle$. In Hamiltonian parameter sphere, this is to rotate the qubit around Ω_y axis. Inset figure on the left shows the chirped control sequence (black) with tomography pulse (yellow). Tomography pulse is continuously connected to the control pulse. **c**, To check if this scheme works, we swept only Rabi frequency Ω without any detuning, and applied $\langle\sigma_x\rangle$ tomography pulse. We measured full contrast oscillation, which is what we expected from $\langle\sigma_x\rangle$ tomography pulse. **b**, Tomography pulse for measuring $\langle\sigma_y\rangle$. In Hamiltonian parameter sphere, this is to rotate the qubit around Ω_x axis. Inset figure on the left shows the chirped control sequence (black) with tomography pulse (yellow). Tomography pulse is now 90 degree phase off from the control pulse. **d**, To check if this scheme works, we swept only Rabi frequency Ω without any detuning, and applied $\langle\sigma_y\rangle$ tomography pulse. We measured 0 contrast signal, which is what we expected from $\langle\sigma_y\rangle$ tomography pulse.

5.5 Measurement of Chern number of a Single Qubit

5.5.1 Chern Number Measurement

Using the dynamic state preparation, and precise quantum state tomography scheme, now we can measure the Berry-curvature. The $\langle \sigma_y \rangle$-component is particularly important here because it gives the deviation from the trajectory due to non-adiabatic effect (Equation (5.13)). To observe the Berry-curvature, we should operate our control pulse scheme in a non-adiabatic regime. In the mean time, we want to be in a quasi-adiabatic regime so that the spin qubit also quasi-adiabatically follows the Larmor vector $\vec{R}(t)$ (Figure 5-5 a).

Since we fix the sweep parameter space size Ω_1, what determines the adiabaticity of dynamic state preparation is the total ramp time, T_{ramp}. In Figure 5-7 of dynamic state preparation, we varied T_{ramp} and observed non-adiabatic response starts to appear when $T_{ramp} < 1000$ ns. As a quasi-adiabatic boundary value, we choose $T_{ramp} = 400$ ns. By integrating $\langle \sigma_y \rangle$ over the Larmor vector path S, we can calculate the corresponding Chern number of given topology (Equation (5.5), (5.13)).

First, we swept θ from 0 to π in $T_{ramp} = 400$ ns and measure the non-adiabatic response of a qubit at each T_{meas} when $\Delta_2/\Delta_1=0$, which is called the topological case and $\Delta_2/\Delta_1=-2$, which is called the trivial case. The results are shown in Figure 5-9. For topological case, the degeneracy point is placed inside the Hamiltonian parameter sphere (resonance point is placed inside the spherical sweep of Δ_1 and Ω_1), therefore, while the qubit spin travels along the spherical path, it acquires a Berry-curvature due to Lorentzian force response. By integrating over this deviation over the θ path, we extract Chern number $C_1 = 1.117 \pm 0.120$ for topological case (Equation (5.5)).

In contrast, for trivial case, the degeneracy point is placed outside the Hamiltonian parameter sphere (resonance point is placed outside the spherical sweep of Δ_1 and Ω_1), overall Berry-curvature acquired during the spherical path is zero. By integrating over the trajectory over the θ path, we extract Chern number $C_1 = 0.006 \pm 0.115$ for trivial case. In theory, we expect the Chern number to be $C_1 = 1$ for topological case and $C_1 = 0$ for trivial case, and this matched with our measurements.
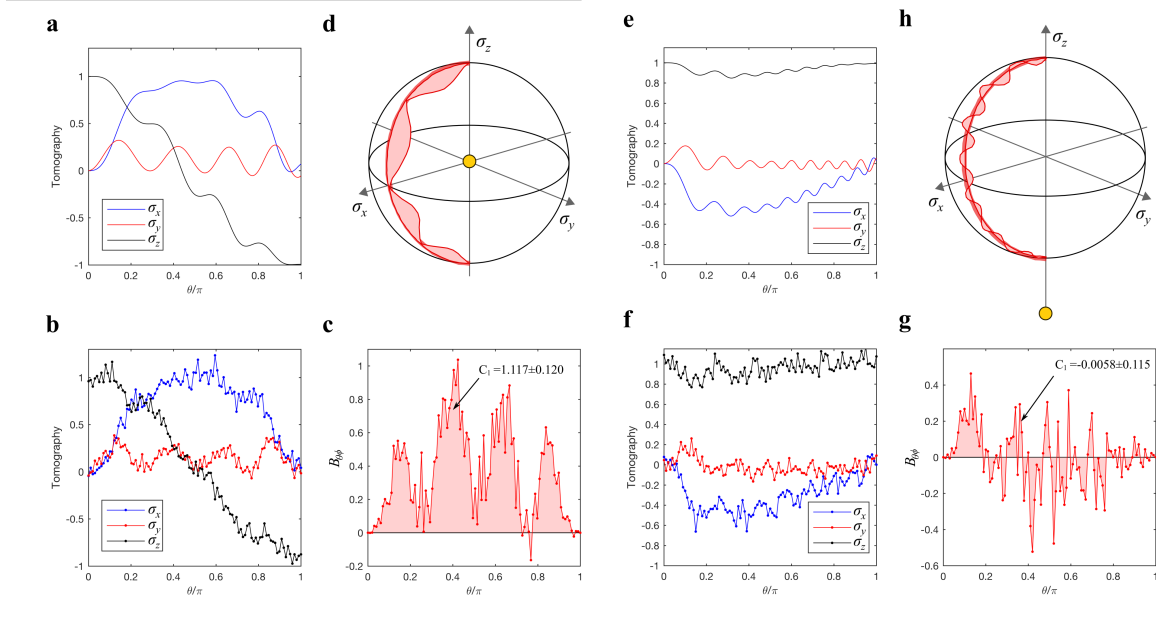
Figure 5-9: **Chern number measurement for two different topologies. a,b**, Spin tomography measurements ($\langle\sigma_x\rangle$ blue, $\langle\sigma_y\rangle$ red, $\langle\sigma_z\rangle$ black) when degeneracy point is inside the parameter sweeping sphere ($\Delta_2/\Delta_1 = 0$). **a** is a numerical simulation with hyperfine coupling effect implemented, and **b** is the measurement. **c**, Calculated Berry curvature $B_{\theta\phi}$ from $\langle\sigma_y\rangle$ tomography measurement. Integrating over the θ path swept from 0 to π gives Chern number of $C_1 = 1.117 \pm 0.120$. Uncertainty is calculated from the uncertainty of Ω_1 in the measurement. **d**, Deviation of the qubit (red shaded area) along the Larmor vector path (red solid line) in Bloch sphere picture. Yellow dot indicates the degeneracy point relative to parameter sphere. **e,f**, Spin tomography measurements when degeneracy point is outside the parameter sweeping sphere ($\Delta_2/\Delta_1 = -2$). **e** is a numerical simulation with hyperfine coupling effect implemented, and **f** is the measurement. **g**, Calculated Berry curvature $B_{\theta\phi}$ from $\langle\sigma_y\rangle$ tomography measurement. Integrating over the θ path swept from 0 to π gives Chern number of $C_1 = 0.006 \pm 0.115$. Uncertainty is calculated from the uncertainty of Ω_1 in the measurement. **h**, Suppressed deviation of the qubit (red shaded area) along the Larmor vector path (red solid line) in Bloch sphere picture. Yellow dot indicates the degeneracy point relative to parameter sphere.

5.5.2 Measurement of Topological Transition via Chern Numbers

Chern number of a single qubit is a number of times that the Larmor vector wraps around the sphere as θ and ϕ are swept. When the Hamiltonian parameter sphere contains the quantum degeneracy point, then the Larmor vector can wrap the sphere once θ is swept ($C_1 = 1$). In contrast, when the quantum degeneracy point is outside the parameter sphere, then the Larmor vector fails to wrap around the sphere ($C_1 = 0$). The topological transition happens when the quantum degeneracy point moves from inside to outside the spherical manifold in Hamiltonian parameter space. In this section, we present the measurement of topological transition via extracting Chern number by varying relative position of the quantum degeneracy point, Δ_2/Δ_1.

We performed $\langle \sigma_y \rangle$ tomography measurements by sweeping Δ_2/Δ_1 from 0 to -2. Again, $\Delta_1 = 10\text{MHz}$, and $T_{ramp} = 400$ ns were fixed. $\langle \sigma_z \rangle$ was also measured as a check for the dynamic state preparation. These measurements agreed with the simulation (Figure 5-10). Each cross sections along the sweep of θ in $\langle \sigma_y \rangle$ tomography measurement corresponds to the non-adiabatic responds of a spin qubit over the path for given Δ_2/Δ_1. By integrating $\langle \sigma_y \rangle$ over the θ path, and using equation (5.8), (5.13), we can extract the Chern number.

Now, we measured transition of Chern number by sweeping Δ_2/Δ_1 (Figure 5-11. As the quantum degeneracy point moves from inside ($\Delta_2/\Delta_1 = 0$) to outside ($\Delta_2/\Delta_1 = -2$) the Hamiltonian parameter sphere, we observed transition of Chern number from 1 to 0. However, the transition in our measurement happens to be a smooth change rather than a discrete jump and there are several reasons for this. First, topological transition ideally is quantized in the limit of $T_{ramp} \to \infty$, for a perfectly coherent, non-dephasing qubit. Because of a finite T_2^* time of the NV spin, the transition is broadened and the perfect quantization is destroyed. This broadening can be expressed as following

$$\delta\left(\frac{\Delta_2}{\Delta_1}\right) \approx \frac{2\pi}{\Delta_1 T_2^*} = 0.16 \tag{5.34}$$

128
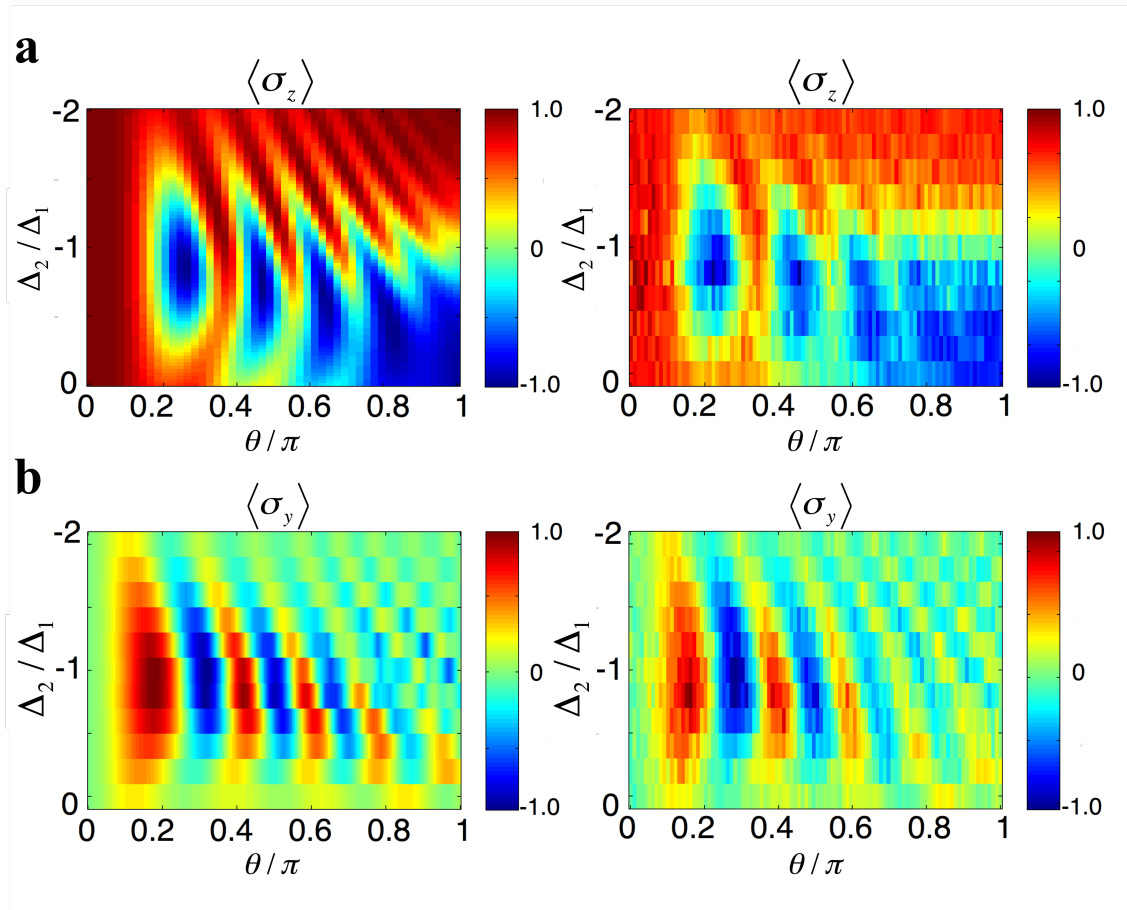
Figure 5-10: **Spin tomography measurements by sweeping** Δ_2/Δ_1. **a,** Simulation (left) and measurement (right) of 2D spin state tomography $\langle\sigma_z\rangle$ by sweeping θ from 0 to π and Δ_2/Δ_1 from -2 to 0. **b,** Simulation (left) and measurement (right) of 2D spin state tomography $\langle\sigma_y\rangle$ by sweeping θ from 0 to π and Δ_2/Δ_1 from -2 to 0.
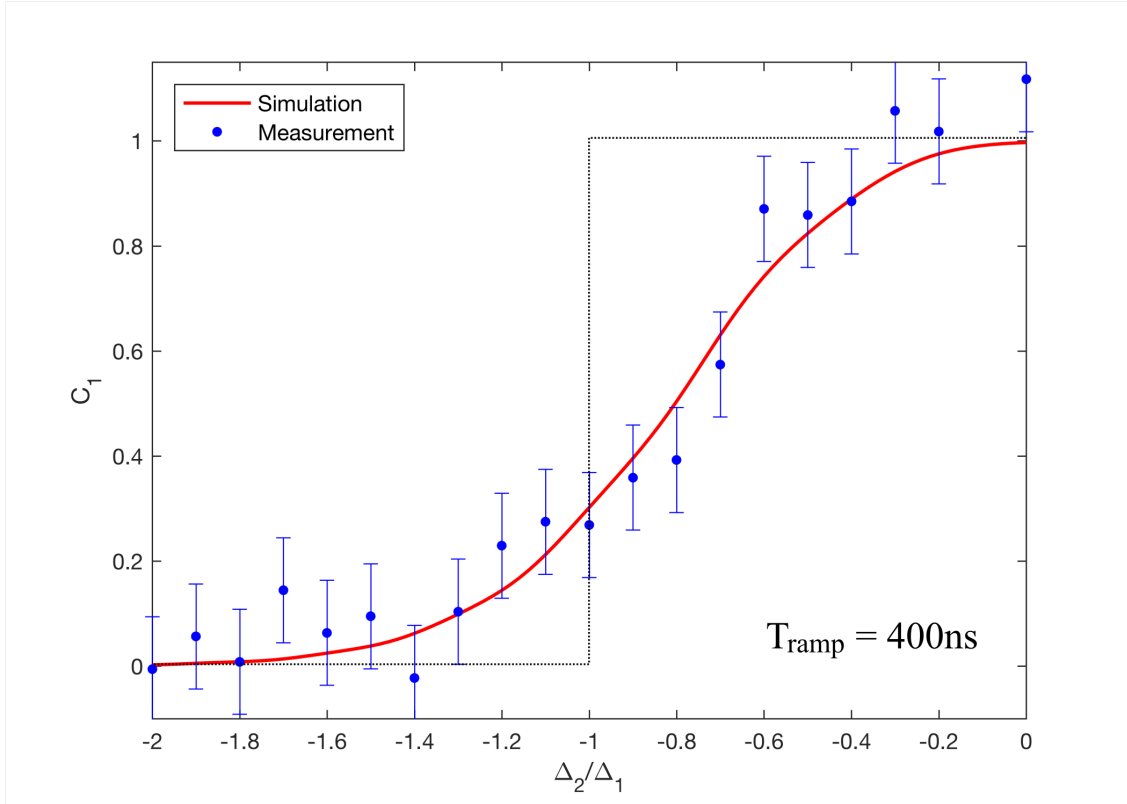
Figure 5-11: **Chern number transition by varying Δ_2/Δ_1.** Blue dots are the measurement, and red solid line is a numerically calculated Chern number with hyperfine splitting effect implemented. We observed transition of the Chern number from 1 to 0 as Δ_2/Δ_1 changed from 0 to -2. Black dotted line is theoretically expected discrete transition of the Chern number. T_{ramp} was fixed to 400 ns. Each blue dots with Chern number C_1 is calculated by measuring $\langle \sigma_y \rangle$ with θ sweep at given Δ_2/Δ_1. Uncertainty was calculated from the uncertainty of Ω_1.
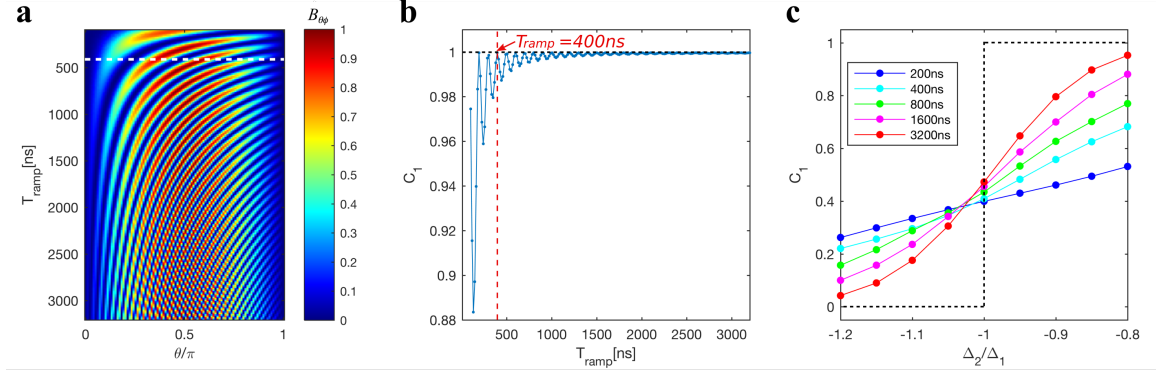
Figure 5-12: **Topological transition slope dependence on T_{ramp}.** **a**, 2D simulation of Berry curvature calculation by sweeping θ from 0 to π and T_{ramp} from 200 to 3200 ns. White dashed line is when $T_{ramp} = 400$ns. As T_{ramp} is increased, signal becomes oscillating faster with lower amplitudes, where the measurement gets challenging with limited SNR. This is the reason why we chose T_{ramp} in the measurement. **b**, Simulation of the Chern number at topological case by sweeping T_{ramp} from 200 to 3200 ns. As T_{ramp} is increased, C_1 of topological approaches closer to perfect 1. Nevertheless, at $T_{ramp} = 400$ ns, we get $C_1 \approx 1$. **c**, Simulated transition slope as we change T_{ramp} from 200 to 3200 ns. Black dashed line indicates discrete transition expected from the theory. As we increase T_{ramp}, transition slope also increases.

This value is less than the width of what we observed in the measurement, which infers that the transition width in fact is limited by fast T_{ramp} time. We used $T_{ramp} = 400$ ns, in which the $\langle \sigma_y \rangle$ signal could be measured with good signal-to-noise ratio. For more discrete transition measurement, we could increase our $T_{ramp} = 1\mu$ s, however, SNR for such measurement is poor so that more time-averaging is inevitable (Figure 5-12 a). We ran a simulation of topological transition of C_1 by varying T_{ramp}, and confirmed that more discrete transition happens for longer T_{ramp} (Figure 5-12 c). From the measurement, we extracted transition slope to be m~0.92, which is comparable to the measurement from SCQ groups measurement, m~1.25 [108], where they used $T_{ramp} = 500$ ns.

Secondly, NV spin has a hyperfine couplings of $h_f = 2.16$MHz (^{14}N) from its host nitrogen nuclear spin (I = 1), which lifts the quantum degeneracy into 3 resonances. For given h_f, $\Omega_1 = 10$MHz sweep in not large enough to induce a sharp transition. Interestingly, this lifted degeneracy can be used to investigate the topology of coupled spins system, which will be discussed in details in next section.

5.6 Measurement of Chern number of Interacting Qubit System

5.6.1 Topological Transition in Coupled Two Qubit System

Study of topological transition of interacting qubits is an interesting topic because the Hamiltonian of interacting qubit system can be mathematically projected into the Hamiltonian of complex condense matter systems. For example, coupled two qubit Hamiltonian can be projected into the Haldane model of the graphene [77, 107, 108]. It is known to be challenging to change the each components of the Haldane Hamiltonian to observe change of topology in graphene. However, changing Hamiltonian parameters with qubits can be simply done by varying microwave parameters, and this makes coupled qubit system as a quantum simulator. In this work, we won't get into the details of projecting coupled qubit system into complex model in condense matter system, but rather focus on observing interesting phenomenological dynamics of topological transition in coupled qubit systems. For the discussion on coupled two qubit system, Hamiltonian of the system can be expressed as [108]

$$H_{2Q} = -\frac{1}{2}\left[H_z(\sigma_1^z + \sigma_2^z) + H_0\sigma_1^z + g(\sigma_1^x\sigma_2^x + \sigma_1^y\sigma_2^y)\right] \quad (5.35)$$

where g is a coupling strength between two spins. Since the total spin in z axis is conserved, first there are two obvious eigenstates: with energies $E_{\uparrow\uparrow/\downarrow\downarrow} = \pm(H_z + H_0/2)$. When the s_{tot}^z=0, then the 44 Hamiltonian reduces to 22 matrix with the eigenenergies of $E_{\uparrow\downarrow/\downarrow\uparrow} = \pm\sqrt{H_0^2/4 + g^2}$. Now, The ground state energy levels of these two sectors are degenerate when $|H_z + H_0/2| = \sqrt{H_0^2/4 + g^2}$, which means that the effective degeneracy points of the given Hamiltonian are

$$H_z^{deg} = \frac{-H_0 \pm \sqrt{H_0^2 + 4g^2}}{2} \quad (5.36)$$

In *P. Roushan et.al.* showed that controlling the coupling constant, g is equivalent to controlling the separation between two degeneracy points along the H_z axis (the

132

detuning axis, Δ, in our Hamiltonian parameter space). Therefore, response of a qubit when varying g with fixed H_r (radius of parameter sweep sphere) is topologically invariant to varying H_r (in our previous measurements, Δ_1) with fixed g.

To summarize, topological transition for interacting two qubit system is topologically equivalent to a single qubit with lifted two degeneracies. For NV spin with ^{14}N host nuclear spin, hyperfine coupling lifts the ground state degeneracy into three states. Therefore, in principle, single NV spin qubit with three hyperfine states can measure topological properties of three interacting qubit system.

To confirm this idea, we ran a proof-of-principle simulation which numerically calculates topological phase transition of two coupled spin qubits, using NV spin with ^{15}N host nuclear spin (I = 1/2) which has two hyperfine states ($h_f = 3$MHz). In the interacting two qubit picture, this is mathematically equivalent to the case when the coupling strength $g = 1.5$MHz. With fixed g, we swept $H_r(\Delta_1) = 0.3$ to 3 MHz and $H_0(\Delta_2) = 0$ to 3 MHz with adiabaticity parameter A (Equation (5.33)) fixed to 6, and calculated the Chern number.

From the simulation result, we could reproduce the same results as in [108] where they used two coupled qubits and varied the coupling strength g to measure the topological phase diagram. Small discrepancy came from the nonlinear dependence of g and H_0 in the equation (5.36).

5.6.2 Topological Transition in Coupled Three Qubit System

After simulating coupled two qubit system with spin qubit with two degeneracy points, now we can move on to measure the topological phase diagram of three qubit coupled system, by using a single NV spin qubit with three hyperfine ground states. In Hamiltonian parameter space, this can be represented as three distinguished degeneracy points separated by the hyperfine splitting of $h_f = 2.16$MHz, along z-axis (detuning Δ axis). In this system, there are two control parameters; H_0 (Δ_2) : offset frequency detuning, H_r ($\Omega_1 = \Delta_1$) : parameter sphere sweep radius. Separation of degeneracy points is fixed to $g = h_f$. Importantly, sweeping H_r allows us to have the same topological dynamics as controlling g between three coupled spin qubits.
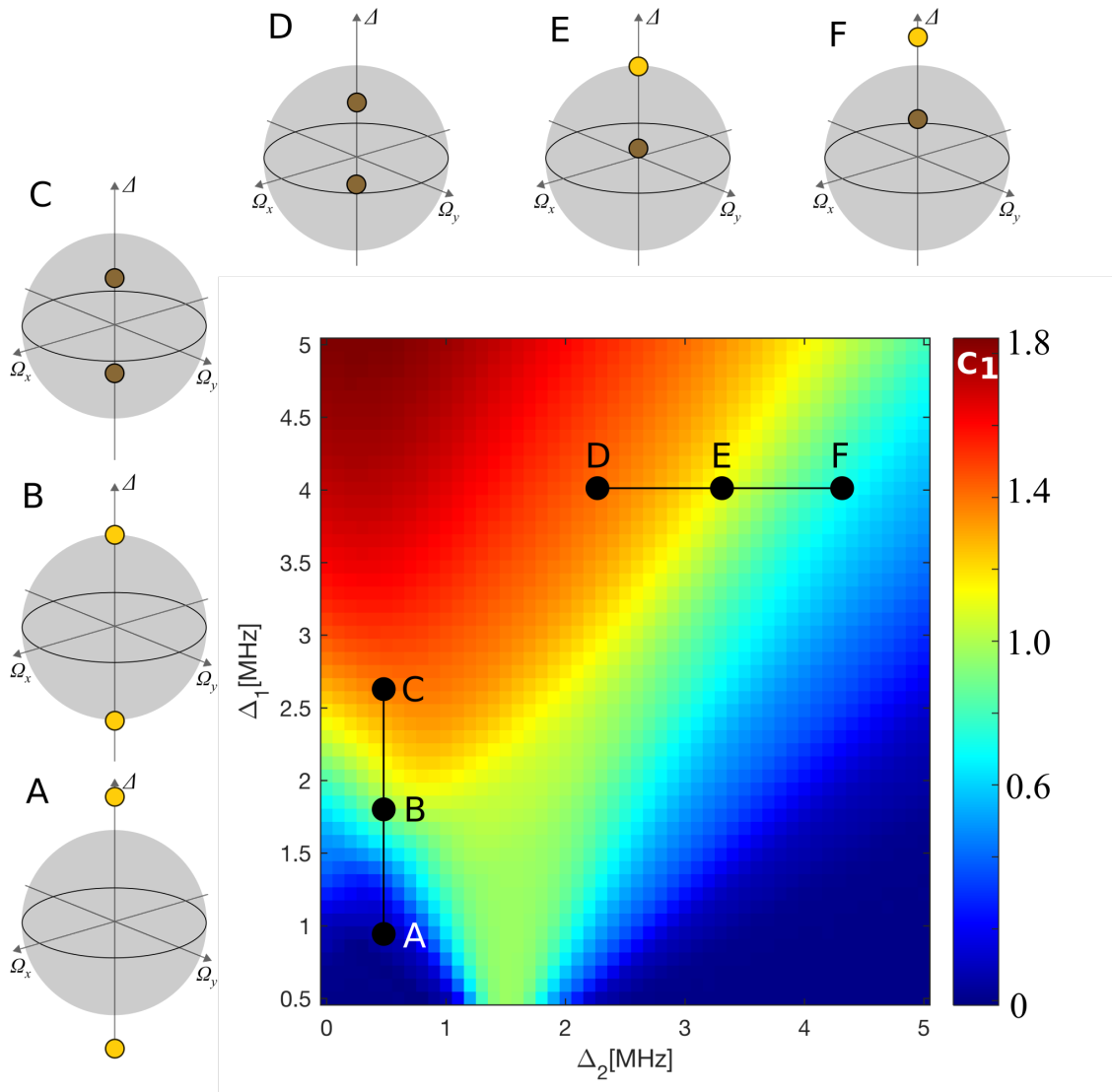
Figure 5-13: **2D simulation of Chern number transition with 2 degeneracies.**
Numerically calculated Chern number transition with two degeneracies separated by
3 MHz in H_z axis. Transition from **A to B to C** indicates increasing the radius of
parameter sphere (Δ_1), where the sphere gradually encloses both degeneracies. In
this case, Chern number shifts from 0 to 1 to almost 2. This is equivalent to reducing
the coupling strength g in two interacting qubit system. Transition from **D to E
to F** indicates moving the center of parameter sphere relative to degeneracies (Δ_2),
where the sphere gradually looses one of the degeneracies. In this case, Chern number
shifts from 2 to 1. This is equivalent to shifting H_0 with fixed g in two interacting
qubit system.

2D topological phase diagram was constructed by sweeping H_0 (Δ_2) = 0 to 5MHz, H_r (Δ_1) = 0.5 to 5 MHz with h_f = 2.16 MHz (Figure 5-14 a). For the proof-of-principle measurement, we performed Chern number measurements by varying Δ_2 = 0 to 5MHz with Δ_1 = 0.5, 1.1, 1.75, 2.2, 3, 4 and 5 MHz (Figure 5-14 b). Here, to fix the adiabaticity parameter $A = 3$, we varied T_{ramp} as Δ_1 is changed (Equation (5.33)). Also, full spin population from all three degeneracies add up to 1 (because we are using a single qubit) in the measurement, and we project this to 3, which is a full spin population for three qubit coupled system.

When $\Delta_1 = 0.5$ MHz, the radius of parameter sphere is smaller than h_f. For each degeneracies, we measured similar Chern number transition to what we measured in previous section (C_1 transition from 1 to 0). When $\Delta_1 = 5$ MHz, the radius of parameter sphere is much larger than h_f, and it could wrap all three degeneracies (Figure 5-14 a). Therefore, we measure the Chern number transition, C_1 from 1 to 3. For 0.5 MHz $< \Delta_1 < 5$ MHz, transition steps of $C_1 = 0,1,2,3$ were observed, and each cross sectional measurement of the 2D topological phase diagram matched with the numerical simulation. We couldn't find any interesting Hamiltonian in condense matter system where it can be projected into three coupled qubit Hamiltonian, which is out of the scope of this work.
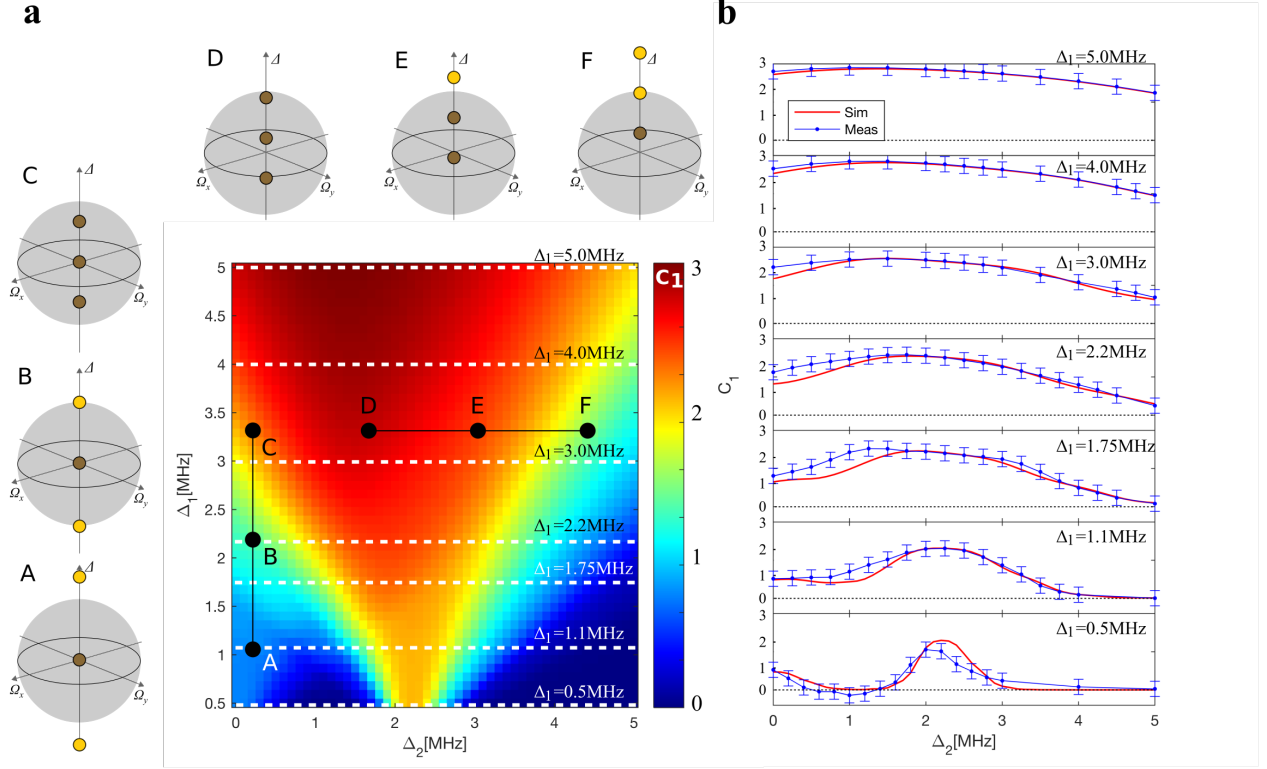
Figure 5-14: **2D topological phase diagram with 3 degeneracies. a**, Numerically calculated Chern number transition with three degeneracies separated by 2.16 MHz in H_z axis. Transition from **A to B to C** indicates increasing the radius of parameter sphere (Δ_1), where the sphere gradually encloses all three degeneracies. In this case, Chern number shifts from 1 to 2 to almost 3. This is equivalent to reducing the coupling strength g in three interacting qubit system. Transition from **D to E to F** indicates moving the center of parameter sphere relative to degeneracies (Δ_2), where the sphere gradually looses two of the degeneracies. In this case, Chern number shifts from 3 to 2 to 1. This is equivalent to shifting H_0 with fixed g in three interacting qubit system. **b**, Measured (blue dots with lines) and simulated (red solid lines) Chern number transition plot by sweeping Δ_2 from 0 to 5 MHz, for fixed Δ_1. These measurements correspond to the cross sections (white dashed line) in 2D topological phase diagram in **a**. Uncertainty in the measurement is given by the uncertainty of $\Omega_1 = \Delta_1$.

5.7 Summary and Outlook

Using the NV center as a spin qubit, we measured Chern number transition from 0 to 1 and transition between 0 to 3 by using the lifted degeneracies due to hyperfine splittings. Due to its simple control scheme of the qubit state in room temperature, NV spin can be a strong candidate to simulate the topology of quantum systems. Furthermore, scalability of NV spins towards non-trivial number of ensembles will allow us to simulate more exotic topological systems.

Chapter 6

Outlook

In this thesis, I used two different control schemes, dynamic phase and geometric phase control, to perform novel quantum measurements to be applied for quantum sensing, in particular magnetic field sensing, and for quantum information science, such as observing change of interaction dynamics between two spins under a dressing field and demonstrating a simple quantum simulation. In this last chapter, let me discuss about further directions of employing these schemes to other interesting quantum measurements.

Quantum Metrology

Magnetic Field Sensing with Entangled State

In quantum magnetometry, improving the sensitivity to sense small fields in condensed matter system [112] or in biological systems [18, 99] is one of the main directions of research. There has been many technical improvements to increase the sensitivity of quantum magnetometer such as collecting more photon signals from ensemble of NV spins [113], increasing the coherence time of NV spin by suppressing noise from the bath [72], or increasing the number of NV sensor spins subject to the sample magnetic field [114]. Despite all these technical and engineering advances, however, the sensitivity is ultimately limited by the fundamental Standard Quantum Limit

(SQL). To push sensitivity below the SQL, there has been many proposals to create non-classical state of spins [115, 116] to beat the sensitivity scaling of $\eta \sim 1/\sqrt{n}$ and to approach Heisenberg scaling of $\eta \sim 1/n$, where n is the number of quantum sensor spins. Creating such non-classical state using NV ensemble spins in diamond still remains as a deep challenge, because of limited understanding on high [N] density samples, however, we can try to utilize two NV spin system (discussed in Chapter 3) to create an entangled state to be applied for magnetic field sensing. For this, same quantization axis two NV spins can be used to create maximally entangled Bell state. Generating Bell state using a pulse sequence in [23], we expect to have improved magnetometry sensitivity of twice compared to the sensitivity of a single NV magnetometer. In general, lifetime of the Bell state is shorter than the coherence time of a single NV, therefore extending entangled state lifetime will be an important topic to study. In AC magnetometry using the Bell state, short coherence time will limit the spectral resolution, however, we can circumvent this problem by combining entanglement state generation with Synchronized Readout scheme, where we can achieve high sensitivity with high spectral resolution for nano-scale AC magnetic field sensing.

Measurement of Quantum Work in Periodically Driven Floquet System

In *P. Weinberg et.al.*, they show that the Chern number is related to work done on the system during the adiabatic cycle [117]. This result shows that the work done on the system during one adiabatic cycle is quantized in units of the driving frequency, Ω, which can be thought as a Floquet energy pump similar to the Thouless pump in equilibrium systems [118]. By carefully thinking about the connection to the Chern number measurement in Chapter 5, we might be able to experimentally demonstrate the quantized energy pump utilizing NV spins and surrounding nuclear spins.

Quantum Information Application

Realization of Quantum Register

NV center in diamond is a hybrid system of electronic spins and nuclear spins, where you can create a complete set of quantum register; We can transfer information through electronic spins and store the information in nuclear spins. Using two NV spin system as the simplest quantum register has already been demonstrated [23]. However, there is no reliable way to scale up the number of strongly coupled NV spins yet. This is because creating NV spin at a desirable position with high precision is a huge technical challenge. Nevertheless, realizing chain of NV spins with similar coupling strengths between spins is an active field of research [119, 120].

Once we realize such system, it becomes important to selectively control each spins without disturbing other spins. This selective addressability can be achieved by applying strong magnetic field gradient [56, 57] along the quantization axis of NV spins. Previous work has demonstrated strength of field gradient up to ~ 0.2 G/nm [57]. However, to be able to selectively control two same axis NV spins with spatial separation of 5nm with fidelity higher than 95%, one wants to create ~ 1.0 G/nm, which gives spectral separation of ~ 14 MHz between two spins. This requires some smart engineering of placing coils on the surface of a diamond via E-beam lithography.

One possible direction as a stepping stone for realizing quantum register is to search for hybrid system of NV spins strongly coupled to g = 2 electronic spins on the surface of diamond. Depth of molecular implanted two NV spins are shallow, therefore, there is a good chance to find strongly coupled NV spin and g = 2 surface dark spin system [121]. Using this system, we can try to create non-classical state such as GHZ (Greenberger-Horne-Zeilinger) state or transfer polarization (information) along the chain of spins using the Hartman-Hahn cross polarization protocol. More rigorous study on fidelity of non-classical state generation vs. local environmental noise will be also interesting topic to study.

Study of Many-Body Physics under Controllable Disorder

Once material engineering allows us to create dense ensemble NV sample where the dominant interaction becomes NV-NV interaction, then we can try to measure some change in many-body dynamics of NV ensemble spins by varying the disorder parameter through dressing scheme (Chapter 3). Here, we can use one class of NV with quantization axis aligned to the bias magnetic field as system spins, and use off-axis NV classes as sources of disorder fields. Dressing into different basis on the off-axis NV class will allow us to tune the disorder where we can fully suppress or continuously sweep the disorder as a control parameter.

Appendix A

Single NV Confocal Setup

Optical Setup

Excitation Path

Measurement with single NV centers is conducted using a home-built confocal scanning laser microscope. First, let me explain green laser path to create excitation path. An acousto-optic modulator (Isomet Corporation) operated at 80 MHz allows time-gating of a 400 mW, 532 nm diode-pumped solid state laser (Changchun New Industries). We align telescope lens, with f = 200 mm, to shrink the beam size passing through AOM. Calculated beam waist are $w_o = 40\mu$m and $w = 64\mu$m at the AOM crystal. 1st order diffracted laser power from AOM is about 66% compare to the input power. Measured isolation is $\sim7.5\times10^{-5}$. This beam is then focused and coupled to single-mode fiber with a mode-field-diameter of ~5 μm (Thorlab), then delivered to an oil-immersion objective (100$\times$, 1.3 NA, Nikon CFI Plan Fluor) focuses the green laser pulses onto an NV center. All this excitation optics are placed on an optical breadboard on top of lead foam, to isolate mechanical noise from the table. (Figure A-1
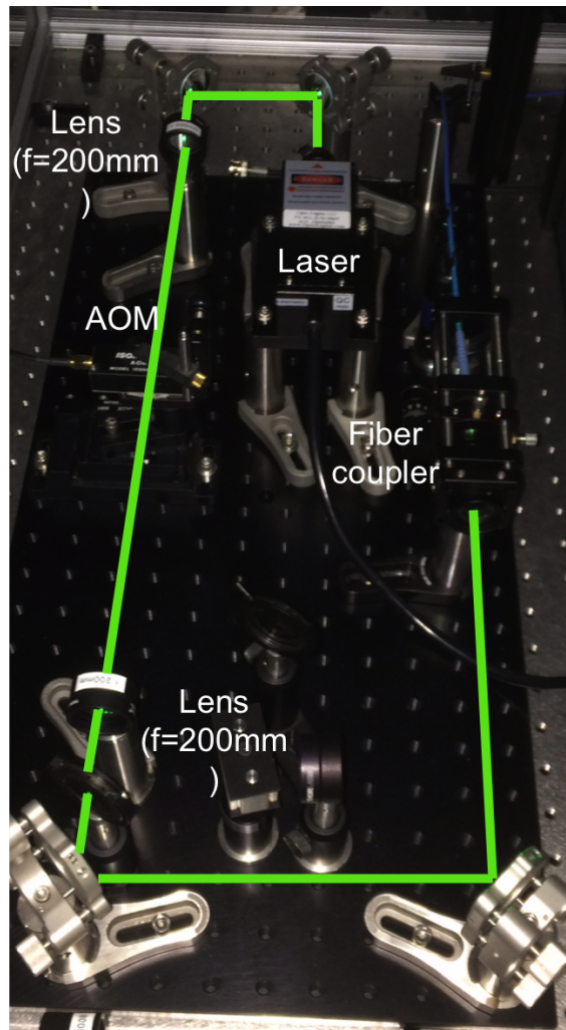
Figure A-1:   **Optical excitation path.**
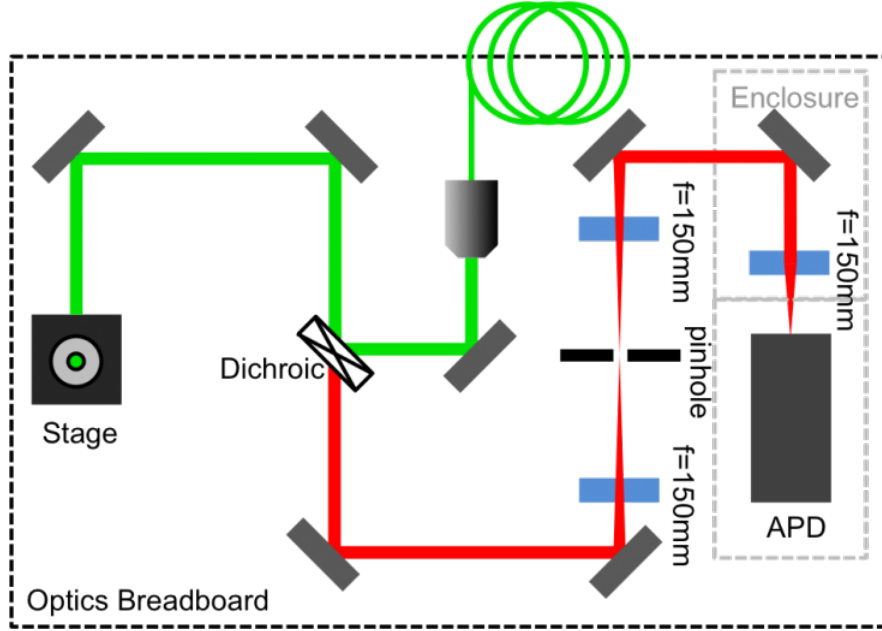
Figure A-2: **Optical detection path schematics.**

Detection Path

Diamond sample is fixed on a three-axis motorized stage (Micos GmbH) which can move in three dimensions by 10 cm. Fiber coupled green laser goes through a dichroic filter (Semrock LP02-633RS-25), excites NV through objective, and NV red fluorescence passes through back to the same objective, and then onto a silicon avalanche photodetector (Perkin Elmer SPCM-ARQH-12). To make confocal, we place a pinhole (diameter 75μm) with f = 150 mm telescope, and remove 20 % of light due to unfocused light. After careful alignment, we measure PSF(X,Y) $\sim$ 250 nm with PSF(Z) $\sim 2\mu$m with single NV FL count of $\sim$ 120 kcps with background of $\sim$ 20 kcps at 1/4 of optical saturation. The NV spin initialization and readout pulses are 3 μs and 0.5 μs, respectively. The change of fluorescence signal is calculated from ΔFL = FL$^+$ - FL$^-$, where FL$\pm$ are the fluorescence counts obtained after spin projection using a microwave $\pi/2$-pulse along the $\pm x$-axis, respectively. For each measurement, the fluorescence count FL when the spin is in the $m_s = 0$ state is also measured as a reference. The temperature of the confocal scanning laser microscope is monitored by a 10k thermistor (Thorlabs) and stabilized to within 0.05 ^{o}C using a 15 W heater controlled with a PID algorithm.
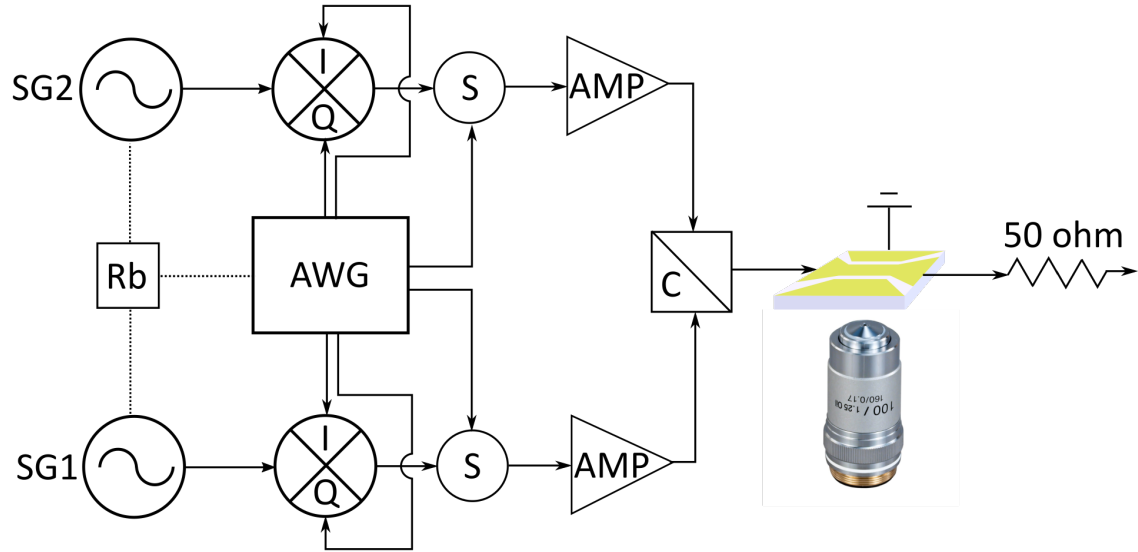
Figure A-3: **Microwave delivery schematics.**

Microwave Setup

A signal generator (SG, Agilent E4428C) provides the carrier microwave signal with frequency $\omega_{LO}/2\pi \sim 3$ GHz. The microwave pulses are generated by an arbitrary waveform generator (AWG, Tektronix AWG 5014C) and sent to the I/Q channels of the IQ mixer (Marki IQ 1545 LMP). Phase control was done by AWG. The output signal from the IQ mixer is amplified (Mini-circuits ZHL-16W-43-S+), and combined (if there are multiple driving frequencies for two NV control), and sent through a gold coplanar waveguide (10μm gap, 1μm height) fabricated on a glass cover-slip by photo-lithography. To reduce phase jitter noise, an in-laboratory Rubidium clock (Stanford Research Systems FS725) phase-locks the signal generator and AWG at 10 MHz

Appendix B

Double Quantum Rabi Nutation

Introduction

When we drive NV spin's $|+1\rangle$, $|-1\rangle$ transition simultaneously, depending on the resonance condition, we get different modulations in double quantum (DQ) Rabi oscillations. This chapter will go through the analytical derivations, and do some example numerical simulations using realistic parameters.

Analytical Calculation

Hamiltonian

Under the doubly rotating frame of $|+1\rangle$ and $|-1\rangle$ transitions, system Hamiltonian can be simplified as below,

$$H = -\delta|+\tilde{1}\rangle\langle+\tilde{1}| + \delta|-\tilde{1}\rangle\langle-\tilde{1}| - \frac{\Omega}{2}\Big[|+\tilde{1}\rangle\langle 0| + |-\tilde{1}\rangle\langle 0| + |0\rangle\langle+\tilde{1}| + |0\rangle\langle-\tilde{1}|\Big]$$

(B.1)

where,

$$|+\tilde{1}\rangle = e^{i\omega_+ t}|+1\rangle, \quad |-\tilde{1}\rangle = e^{i\omega_- t}|-1\rangle$$

(B.2)

147

Now, to express in terms of the DQ basis of bright state $|B\rangle$ and dark state $|D\rangle$,

$$|+\tilde{1}\rangle = \frac{1}{\sqrt{2}}\Big[|B\rangle + |D\rangle\Big], |-\tilde{1}\rangle = \frac{1}{\sqrt{2}}\Big[|B\rangle - |D\rangle\Big] \tag{B.3}$$

system Hamiltonian can be rewritten as,

$$H = -\delta|B\rangle\langle D| - \delta|D\rangle\langle B| - \frac{\Omega}{\sqrt{2}}\Big[|B\rangle\langle 0| + |0\rangle\langle B|\Big] \tag{B.4}$$

State of the NV spin goes under the time evolution, therefore

$$\Psi(t) = C_B(t)|B\rangle + C_0(t)|0\rangle + C_D(t)|D\rangle \tag{B.5}$$

Under the time dependent Schrödinger equation,

$$H\Psi(t) = -\Big(\delta + \frac{\Omega}{\sqrt{2}}\Big)|B\rangle - \frac{\Omega}{\sqrt{2}}|0\rangle - \delta|D\rangle = i\partial_t\psi \tag{B.6}$$

Time evolution of the state coefficients are

$$\dot{C}_B(t) = i\delta C_D(t) + \frac{i\Omega}{\sqrt{2}}C_0(t), \quad \dot{C}_0(t) = \frac{i\Omega}{\sqrt{2}}C_B(t), \quad \dot{C}_D(t) = i\delta C_B(t) \tag{B.7}$$

On Resonance Case

When there is no detuning in Rabi drive, then the state evolution equations are

$$\dot{C}_B(t) = \frac{i\Omega}{\sqrt{2}}C_0(t), \quad \dot{C}_0(t) = \frac{i\Omega}{\sqrt{2}}C_B(t), \quad \dot{C}_D(t) = 0 \tag{B.8}$$

and this results in DQ Rabi oscillation between $|0\rangle$ and $|B\rangle$

$$\Omega_{DQR} = \sqrt{2}\omega \tag{B.9}$$

No Driving Case

When there is no Rabi drive, Ω is zero, then the state evolution equations are

$$\dot{C}_B(t) = i\delta C_D(t), \quad \dot{C}_0(t) = 0, \quad \dot{C}_D(t) = i\delta C_B(t) \tag{B.10}$$

and this results in DQ state oscillation between $|B\rangle$ and $|D\rangle$

$$\Omega_{DQS} = 2\delta \tag{B.11}$$

Off Resonance Case

When there is a detuning in Rabi drive, then the state evolution equations are

$$\dot{C}_B(t) = i\delta C_D(t) + \frac{i\Omega}{\sqrt{2}}C_0(t), \quad \dot{C}_0(t) = \frac{i\Omega}{\sqrt{2}}C_B(t), \quad \dot{C}_D(t) = i\delta C_B(t) \tag{B.12}$$

We can calculate the time evolution of the state by solving the above differential equations.

Numerical Calculation on Off-Resonant case

Now, let's numerically calculate the state evolution for off-resonant DQ Rabi. For the case of ^{14}N, there always is a detuning factor due to the hyperfine splitting, which is about 2.16 MHz. If we assume that our Rabi frequency is 10 MHz, then for on resonance drive, DQ Rabi we get is 14.15 MHz, as simulated in Figure B-1.

Now, for hyperfine detuned state, there are modulation on DQ Rabi. For 2.16 MHz detuning with 10 MHz Rabi driving power, we get 7.4 MHz modulation on the Rabi oscillation, which is simulated in Figure B-2.
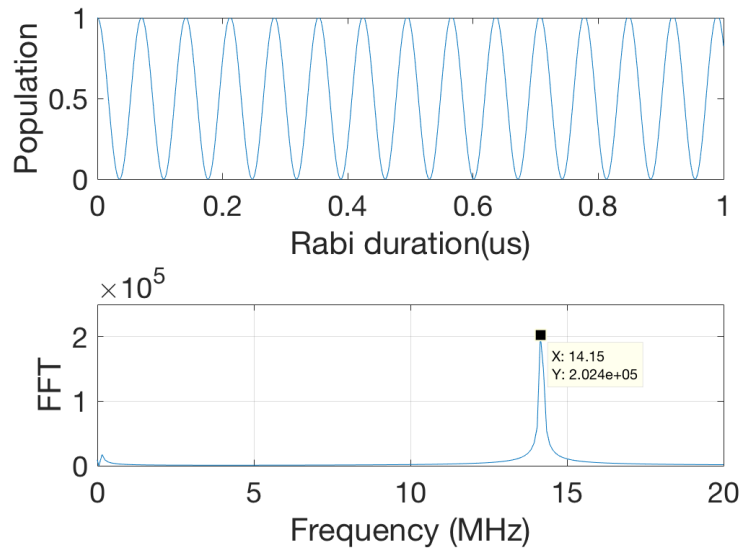
Figure B-1: DQ Rabi 10 MHz on resonance drive. DQ Rabi frequency is at 14.15 MHz
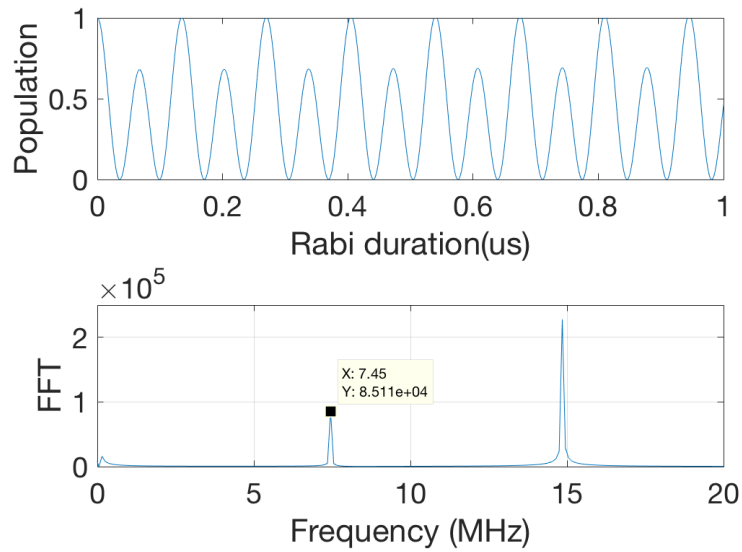
Figure B-2: DQ Rabi 10 MHz, 2.16 MHz detuned drive. DQ Rabi frequency is at 14.8 MHz with 7.4 MHz modulation

Appendix C

Double Ion Implanted Sample

Creation of two NV pair is done by molecular ion implanted technique (Innovion corp), with the implantation dosage of $\sim$6 keV and density of 1×10^9 cm^{-3} on isotopically pure (99.99% ^{12}C) diamond substrate. After the implantation, it is annealed in the oven with 800 ^{o} for 8 hours and at 1000 ^{o}C for 10 hours. Quick statistical measurement of FL measurement reveals conversion ratio between single to double NV to be $\sim$ 5 %

From [67], 6 keV ion implantation expects to create pairs with average separation of $\sim$ 6 nm, and this corresponds to $\sim$ 0.2 MHz of coupling strength between two NV spins. From the DEER measurement, we measured variation of coupling strength ranging from 0.050 MHz up to 0.8 MHz.
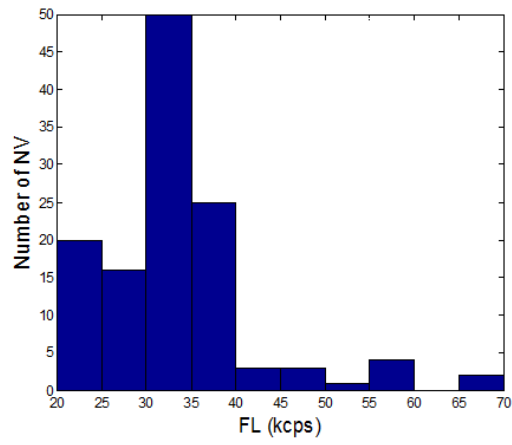
Figure C-1: **NV FL statistics.**

Appendix D

Motional Narrowing in spin$-1/2$

Let us look at two-body spin$-1/2$ toy model to examine how dynamic spin driving of one of the two coupled spins changes effective dipolar coupling strength. Full Hamiltonian of the system is given as

$$H(t) = \frac{\gamma B_A}{2}\sigma_A^z + \frac{\nu}{4}\sigma_A^z \otimes \sigma_B^z + \frac{\gamma B_B}{2}\sigma_B^z + \frac{\Omega}{2}\cos(\omega t)\sigma_B^x, \tag{D.1}$$

where σ^i are Pauli matrices for spin$-1/2$.

$$\sigma^x = \begin{pmatrix} 0 & 1 \\ 1 & 0 \end{pmatrix} \quad \sigma^y = \begin{pmatrix} 0 & -i \\ i & 0 \end{pmatrix} \quad \sigma^z = \begin{pmatrix} 1 & 0 \\ 0 & -1 \end{pmatrix} \tag{D.2}$$

γ is a gyromagnetic ratio, ν is strength of the dipolar coupling, Ω is Rabi frequency, ω is frequency of microwave field, and finally, B_A and B_B are external bias magnetic field on spin A and spin B, respectively. Spin B is driven along the σ^x axis and Ramsey spectroscopy is done with a sensing spin, spin A. When we go to doubly rotating frame on both spin A and B, the Hamiltonian in this frame is

$$\tilde{H} = UH(t)U^\dagger - iU\frac{dU^\dagger}{dt} \tag{D.3}$$

where $U = \exp[i\left((\gamma B_A - \delta\omega_A)\sigma_A^z + \omega\sigma_B^z\right)t/2]$ and $\delta\omega$ is a detuning in Ramsey spectroscopy. The doubly rotating frame Hamiltonian is further calculated as

$$\tilde{H} = \frac{\delta\omega_A}{2}\sigma_A^z + \frac{\nu}{4}\sigma_A^z \otimes \sigma_B^z + \frac{(\gamma B_B - \omega)}{2}\sigma_B^z + \frac{\Omega}{2}\frac{e^{i\omega t} + e^{-i\omega t}}{2}(\sigma_B^+ e^{i\omega t} + \sigma_B^- e^{-i\omega t}), \quad (D.4)$$

where

$$\sigma^+ = \begin{pmatrix} 1 & 0 \\ 0 & 0 \end{pmatrix} \qquad \sigma^- = \begin{pmatrix} 0 & 0 \\ 0 & 1 \end{pmatrix} \qquad (D.5)$$

By choosing $\omega = \gamma B_B$ and applying rotating-wave approximation, we have

$$\tilde{H} = \frac{\delta\omega_A}{2}\sigma_A^z + \frac{\nu}{4}\sigma_A^z \otimes \sigma_B^z + \frac{\Omega}{4}\sigma_B^x \qquad (D.6)$$

Hence the von Neumann equation in doubly rotating frame is

$$\frac{d\,\tilde{\rho}(t)}{dt} = -i[\tilde{H}, \tilde{\rho}(t)] \qquad (D.7)$$

Since $\tilde{H}$ is a time independent Hamiltonian, $\tilde{\rho}(t + dt) = e^{-i\tilde{H}dt}\rho(t)e^{i\tilde{H}dt}$.

Calculating eigenvectors and eigenvalues for the Hamiltonian $\tilde{H}$, we get

$$
\begin{aligned}
|\xi\rangle_+ &= \frac{\nu + \sqrt{\nu^2 + \Omega^2}}{\Omega}\widetilde{|\uparrow\uparrow\rangle} + \widetilde{|\uparrow\downarrow\rangle} & \lambda_{\xi+} &= \frac{1}{2}\delta\omega_A + \frac{\sqrt{\nu^2 + \Omega^2}}{4} \\
|\xi\rangle_- &= -\frac{\nu - \sqrt{\nu^2 + \Omega^2}}{\Omega}\widetilde{|\downarrow\uparrow\rangle} + \widetilde{|\downarrow\downarrow\rangle} & \lambda_{\xi-} &= -\frac{1}{2}\delta\omega_A + \frac{\sqrt{\nu^2 + \Omega^2}}{4} \\
|\eta\rangle_+ &= \frac{\nu - \sqrt{\nu^2 + \Omega^2}}{\Omega}\widetilde{|\uparrow\uparrow\rangle} + \widetilde{|\uparrow\downarrow\rangle} & \lambda_{\eta+} &= \frac{1}{2}\delta\omega_A - \frac{\sqrt{\nu^2 + \Omega^2}}{4} \\
|\eta\rangle_- &= -\frac{\nu + \sqrt{\nu^2 + \Omega^2}}{\Omega}\widetilde{|\downarrow\uparrow\rangle} + \widetilde{|\downarrow\downarrow\rangle} & \lambda_{\eta-} &= -\frac{1}{2}\delta\omega_A - \frac{\sqrt{\nu^2 + \Omega^2}}{4}
\end{aligned}
\qquad (D.8)
$$

where $\widetilde{|\uparrow\uparrow\rangle}, \widetilde{|\uparrow\downarrow\rangle}, \widetilde{|\downarrow\uparrow\rangle}, \widetilde{|\downarrow\downarrow\rangle}$ are two spin$-1/2$ basis in doubly rotating frame. Among these eigenstates, we want eigenenergy differences when the first spin, spin A, being

flipped, $|\uparrow\rangle \leftrightarrow |\downarrow\rangle$. These transitions are

$$
\begin{aligned}
|\xi\rangle_+ &\leftrightarrow |\xi\rangle_- : \delta\omega_A \\
|\eta\rangle_+ &\leftrightarrow |\eta\rangle_- : \delta\omega_A \\
|\xi\rangle_+ &\leftrightarrow |\eta\rangle_- : \delta\omega_A + \frac{\sqrt{\nu^2 + \Omega^2}}{2} \\
|\xi\rangle_- &\leftrightarrow |\eta\rangle_+ : \delta\omega_A - \frac{\sqrt{\nu^2 + \Omega^2}}{2}
\end{aligned}
\tag{D.9}
$$

Ramsey sequence is a powerful spectroscopic tool to measure the eigenstates and eigenvalues of given Hamiltonian, in the basis of spin σ^z. Under the Ramsey spectroscopy sequence on spin A, we can also derive the same result as above.We first prepare spins in initial density matrix, $\tilde{\rho}(0) = |\downarrow\rangle_A \langle\downarrow|_A \otimes (P_d |\downarrow\rangle_B \langle\downarrow|_B + P_u |\uparrow\rangle_B \langle\uparrow|_B)$ and apply $\pi/2$ rotation, $\tilde{U}_A^{(\frac{\pi}{2})_x}$ pulse on spin A, let the system evolve with the Hamiltonian $\tilde{H}$ for time t, apply $\tilde{U}_A^{(\pm\frac{\pi}{2})_x}$ pulse, and finally measure the probability of spin A being in a $|\downarrow\rangle_A$. Assuming that the $\tilde{U}_A^{(\pm\frac{\pi}{2})_x}$ pulses are applied instantaneously, i.e., the system does not evolve with $\tilde{H}$ during $\pi/2$ pulses, observed probability $P_A^{|\downarrow\rangle}$ is expressed as

$$
P_A^{|\downarrow\rangle} = \mathrm{Tr}\left[\left(\frac{\sigma_A^z + \mathbb{1}_A}{2} \otimes \mathbb{1}_B \right) \tilde{U}_A^{(-\frac{\pi}{2})_x} e^{-i\tilde{H}t} \tilde{U}_A^{+(\frac{\pi}{2})_x} \rho(0) \tilde{U}_A^{\dagger(+\frac{\pi}{2})_x} e^{i\tilde{H}t} \tilde{U}_A^{\dagger(-\frac{\pi}{2})_x} \right] \tag{D.10}
$$

$$
= \frac{1}{2} + \frac{\cos(\delta\omega_A t)\left(\Omega^2 + \nu^2 \cos(\alpha t)\right) + (P_d - P_u)\nu\sqrt{\Omega^2 + \nu^2}\sin(\delta\omega_A t)\sin(\alpha t)}{2(\Omega^2 + \nu^2)}
$$

$$
\tag{D.11}
$$

where $\alpha = \sqrt{\Omega^2 + \nu^2}/2$. To understand the meaning of this analytic expression, we take $P_d = P_u = 1/2$, i.e., take the initial state of spin B to be in a maximally mixed state, as an example. Then

$$
P_A^{|\downarrow\rangle} = \frac{1}{2} + \frac{\Omega^2 \cos(\delta\omega_A t) + \nu^2 \left(\cos\left((\delta\omega_A + \alpha)t\right) + \cos\left((\delta\omega_A - \alpha)t\right)\right)/2}{2(\Omega^2 + \nu^2)} \tag{D.12}
$$

This implies that there are three resonance frequencies : $\delta\omega_A$ with an amplitude of $\Omega^2/2(\Omega^2 + \nu^2)$, $\delta\omega_A \pm \sqrt{\Omega^2 + \nu^2}/2$ with amplitude of $\nu^2/4(\Omega^2 + \nu^2)$. This result is the

same as what we calculated as transition resonances between Eigenstates in above equations. Notice that when $\Omega = 0$ and $\nu = 0$, then $P_A^{|\downarrow\rangle} = (1 + \cos(\delta\omega_A t))/2$, which retrieves Ramsey spectroscopy for a single spin.

As we increase the driving Rabi frequency of spin B, Ω, Ramsey FFT $\delta\omega_A$ peak grows, and the right (left) peak amplitude shrinks and gets pushed further away from $\delta\omega_A$ peak. Moreover, for $\Omega \gg \nu$, only $\delta\omega_A$ peak remains with full amplitude, in which driving field on spin B fully suppresses dipolar coupling on spin A and recovers the Ramsey spectroscopy for a single spin. Let us say that we want to suppress the dipolar coupling as much as $X\%$ compared to non-driven full dipolar coupled Hamiltonian. Then the Rabi frequency, Ω, should be $\Omega \geq 10\nu/\sqrt{100 - X}$. For example, to suppress $X = 90\%$ with $\nu = 500$ kHz, Rabi frequency should be at least $\Omega = 1.58$ MHz. Since Rabi frequency is a function of given dipolar coupling strength, Ramsey spectroscopy combined with spin bath driving could be used to study the average dipolar coupling between sensor spins and bath spins to extract information on bath spin density.

Appendix E

Calculation of Non-Adiabatic Response of a Qubit

The goal is to derive the most important equation in the Floquet Chern number measurement.

$$\langle F_\phi \rangle = -\langle \partial_\phi H \rangle = \langle \psi_0 | \, F_\phi \, | \psi_0 \rangle - v_\theta B_{\theta\phi} + O(v^2) \tag{E.1}$$

The first term is a constant and the second term is the product of parameter ramp speed v_θ and the Berry curvature $B_{\theta\phi}$. This equation can be understood in analogy with the Lorentz force in electromagnetism [108].

Adiabatic Perturbation Theory

Let us start from the parameter-dependent Hamiltonian

$$\mathcal{H}(\lambda) \tag{E.2}$$

The parameter $\lambda(t)$ is time-dependent and varied at a rate of $v_\lambda = d\lambda/dt$. The Schrödinger equation is

$$i\partial_t \, | \psi \rangle = \mathcal{H}(t) \, | \psi \rangle \tag{E.3}$$

We use an instantaneous basis

$$|\psi(t)\rangle = \sum_n a_n(t) \, |n(t)\rangle \tag{E.4}$$

which satisfies the following eigenvalue equation

$$\mathcal{H}(t) \, |n(t)\rangle = \epsilon_n(t) \, |n(t)\rangle \tag{E.5}$$

Note that the basis is also time dependent. The Schrödinger equation is rewritten as

$$i\partial_t a_m(t) + i \sum_n a_n(t) \, \langle m(t)| \, \partial_t \, |n(t)\rangle = \epsilon_m(t) a_m(t) \tag{E.6}$$

We apply a gauge transformation and make the right hand side zero to solve this equation

$$a_n(t) \rightarrow a_n'(t) = a_n(t) \exp[-i\Theta_n(t)], \quad \Theta_n(t) = \int_{t_i}^t \epsilon_n(\tau) d\tau \tag{E.7}$$

The Schrödinger equation transforms as

$$\dot{a}_n(t) = -\sum_n a_m(t) \, \langle n| \, \partial_t \, |m\rangle \exp[i(\Theta_n(t) - \Theta_m(t)] \tag{E.8}$$

By integrating both hand sides

$$a_n(t) = -\int_{t_i}^t dt' \sum_m a_m(t') \, \langle n| \, \partial_{t'} \, |m\rangle \, e^{i(\Theta_n(t') - \Theta_m(t'))} \tag{E.9}$$

For later convenience, we will put the $n = m$ term into the exponent. We define a Berry connection

$$\mathcal{A}_n = -i \, \langle n| \, \partial_t \, |n\rangle \tag{E.10}$$

This term can always be incorporated into the exponent as a Berry phase by a unitary transformation $\Theta_n \rightarrow \Theta_n' = \Theta_n + \gamma_n$, where $\gamma_n = \int dt \mathcal{A}$. From now, we just drop the

prime sign for simplicity.

$$a_n(t) = -\int_{t_i}^{t} dt' \sum_{m \neq n} a_m(t') \langle n| \partial_{t'} |m\rangle \, e^{i(\Theta_n(t') - \Theta_m(t'))} \tag{E.11}$$

Two-Level System

Now we consider a two-level system. We are primarily interested in the transition amplitude from the ground state to the excited state of the final Hamiltonian

$$a_n(t) = -\int_{t_i}^{t} dt' \sum_{m \neq n} a_0(t') \langle n| \partial_{t'} |0\rangle \, e^{i(\Theta_n(t') - \Theta_0(t'))} \tag{E.12}$$

The stationary phase approximation gives

$$a_n(t) \simeq i \frac{\langle n| \partial_{t'} |0\rangle}{(\epsilon_n - \epsilon_0)} e^{i(\Theta_n(t') - \Theta_0(t'))} \big|_{t_i}^{t_f} \tag{E.13}$$

We can go to the parameter space by $t \to \lambda, \partial_t \to v_\lambda \partial_\lambda$.

$$a_n(t) \simeq i v_\lambda \frac{\langle n| \partial_\lambda |0\rangle}{(\epsilon_n - \epsilon_0)} e^{i(\Theta_n - \Theta_0)} \big|_{\lambda_i}^{\lambda_f} = -i v_\lambda \frac{\langle n| \partial_\lambda \mathcal{H} |0\rangle}{(\epsilon_n - \epsilon_0)^2} e^{-i(\Theta_n - \Theta_0)} \big|_{\lambda_i}^{\lambda_f} \tag{E.14}$$

Note that Θ_n includes both the dynamical and the Berry phase

$$\Theta_n(\lambda) = \int_\lambda^{\lambda_f} d\lambda' \left[\frac{\epsilon_n}{v_\lambda} - i\mathcal{A}_n \right] \tag{E.15}$$

This phase can be dropped if the initial state has a large gap or if the protocol is designed in such a way that the initial evolution is adiabatic

$$a_n(t) \simeq -i v_\lambda \frac{\langle n| \partial_\lambda \mathcal{H} |0\rangle}{(\epsilon_n - \epsilon_0)^2} \big|_{\lambda_f} \tag{E.16}$$

The generalized force along the μ-direction is therefore given by

$$\mathcal{F}_\mu = \langle \psi| - \partial_\mu \mathcal{H} |\psi\rangle \simeq \langle 0| - \partial_\mu \mathcal{H} |0\rangle + iC \tag{E.17}$$

where the first term simply gives a constant $\mathcal{F}_{0\mu}$, and the second term is

$$C = v_\lambda \sum_{n \neq 0} \frac{\langle 0| \partial_\mu \mathcal{H} |n\rangle \langle n| \partial_\lambda \mathcal{H} |0\rangle - \langle 0| \partial_\lambda \mathcal{H} |n\rangle \langle n| \partial_\mu \mathcal{H} |0\rangle}{(\epsilon_n - \epsilon_0)^2} \tag{E.18}$$

Now we prove that the second term is equivalent to the Berry curvature. We start from the first half. First, we can use the following relation.

$$\frac{\langle 0| \partial_\mu \mathcal{H} |n\rangle \langle n| \partial_\lambda \mathcal{H} |0\rangle}{(\epsilon_n - \epsilon_0)} = \langle 0| \partial_\mu |n\rangle \langle n| \partial_\lambda |0\rangle \tag{E.19}$$

Then, the integration by parts gives,

$$\langle 0| \partial_\mu |n\rangle \langle n| \partial_\lambda |0\rangle = \partial_\mu (\langle 0| |n\rangle \langle n| \partial_\lambda |0\rangle) - (\partial_\mu \langle 0|) |n\rangle \langle n| \partial_\lambda |0\rangle - \langle 0| n\rangle \partial_\mu (\langle n| \partial_\lambda |0\rangle) \tag{E.20}$$

By using an identity, $1 = \sum_n |n\rangle \langle n| = \sum_{n \neq 0} |n\rangle \langle n| + |0\rangle \langle 0|$, and the orthogonal condition $\langle n| 0\rangle = 0 (n \neq 0)$, the first part of C can be rewritten as

$$\sum_{n \neq 0} \langle 0| \partial_\mu |n\rangle \langle n| \partial_\lambda |0\rangle = -(\partial_\mu \langle 0|)(\partial_\lambda |0\rangle) + (\partial_\mu \langle 0|) |0\rangle \langle 0| \partial_\lambda |0\rangle \tag{E.21}$$

The second half of C is obtained by swapping μ and λ.

$$\sum_{n \neq 0} \langle 0| \partial_\lambda |n\rangle \langle n| \partial_\mu |0\rangle = -(\partial_\lambda \langle 0|)(\partial_\mu |0\rangle) + (\partial_\lambda \langle 0|) |0\rangle \langle 0| \partial_\mu |0\rangle \tag{E.22}$$

When we combine these two, we obtain the following result

$$\begin{aligned}
C &= (\partial_\mu \langle 0|)(\partial_\lambda |0\rangle) + (\partial_\mu \langle 0|) |0\rangle \langle 0| \partial_\lambda |0\rangle - (\partial_\lambda \langle 0|)(\partial_\mu |0\rangle) + (\partial_\lambda \langle 0|) |0\rangle \langle 0| \partial_\mu |0\rangle \\
&= \partial_\mu (\langle 0| \partial_\lambda |0\rangle) - \partial_\lambda (\langle 0| \partial_\mu |0\rangle) \\
&= \partial_\mu \mathcal{A}_\lambda - \partial_\lambda \mathcal{A}_\mu = \mathcal{B}_{\mu\lambda} \tag{E.23}
\end{aligned}$$

where $\mathcal{B}$ denotes . Finally, we obtain the Lorentz force equation that we wanted.

$$\mathcal{F}_\mu = \mathcal{F}_{0\mu} + v_\lambda \mathcal{B}_{\mu\lambda} \tag{E.24}$$

Bibliography

[1] I. Bloch. Ultracold quantum gases in optical lattices. *Nature Physics*, 1:23–30, 2005.

[2] M. Lewenstein, A. Sanpera, V. Ahufinger, B. Damski, A. Sen De, and U. Sen. Ultracold atomic gases in optical lattices: mimicking condensed matter physics and beyond. *Advances in Physics*, 56(2):243–379, 2007.

[3] D. Leibfried, R. Blatt, C. Monroe, and D. Wineland. Quantum dynamics of single trapped ions. *Reviews of Modern Physics*, 75(1):281, 2003.

[4] D. M. Meekhof, C. Monroe, B. E. King, W. M. Itano, and D. J. Wineland. Generation of nonclassical motional states of a trapped atom. *Physical Review Letters*, 76:1796, 1996.

[5] J. M. Martinis, S. Nam, J. Aumentado, and C. Urbina. Rabi oscillations in a large josephson-junction qubit. *Physical Review Letters*, 89:117901, 2002.

[6] K. W. Lehnert, K. Bladh, L. F. Spietz, D. Gunnarsson, D. I. Schuster, P. Delsing, and R. J. Schoelkopf. Measurement of the excited-state lifetime of a microelectronic circuit. *Physical Review Letters*, 90:027002, 2003.

[7] J. M. Elzerman, R. Hanson, L. H. Willems Van Bereven, B. Witkamp, L. M. Vandersypen, and L. P. Kouwenhoven. Single-shot read-out of an individual electron spin in a quantum dot. *Nature*, 430:431, 2004.

[8] M. Kroutvar, Y. Ducommun, D. Heiss, M. Bichler, D. Schuh, G. Abstreiter, and J. J. Finley. Optically programmable electron spin memory using semiconductor quantum dots. *Nature*, 432:81, 2004.

[9] L. C. L. Hollenberg, A. S. Dzurak, C. Wellard, A. R. Hamilton, D. J. Reilly, G. J. Milburn, and R. G. Clark. Charge-based quantum computing using single donors in semiconductors. *Physical Review B*, 69:113301, 2004.

[10] A Gruber, A Drbenstedt, C Tietz, L Fleury, J Wrachtrup, and C Von Borczyskowski. Scanning confocal optical microscopy and magnetic resonance on single defect centers. *Science*, 276(5321):2012–2014, 1997.

[11] R. J. Epstein, F. M. Mendoza, Y. K. Kato, and D. D. Awschalom. Anisotropic interactions of a single spin and dark-spin spectroscopy in diamond. *Nature Physics*, 1:94–98, 2005.

[12] L. Childress, M. V. Gurudev Dutt, J. M. Taylor, A. S. Zibrov, F. Jelezko, J. Wrachtrup, P. R. Hemmer, and M. D. Lukin. Coherent dynamics of coupled electron and nuclear spin qubits in diamond. *Science*, 314(5797):281–285, 2006.

[13] J. R. Maze, P. L. Stanwix, J. S. Hodges, S. Hong, J. M. Taylor, P. Cappellaro, L. Jiang, M. V. Gurudev Dutt, E. Togan, A. S. Zibrov, A. Yacoby, R. L. Walsworth, and M. D. Lukin. Nanoscale magnetic sensing with an individual electronic spin in diamond. *Nature*, 455:644–647, 2008.

[14] L. Childress, R. Walsworth, and M. Lukin. Atom-like crystal defects: From quantum computers to biological sensors. *Physics Today*, 67(10):38, 2014.

[15] J. M. Taylor, P. Cappellaro, L. Childress, L. Jiang, D. Budker, P. R. Hemmer, A. Yacoby, R. L. Walsworth, and M. D. Lukin. High-sensitivity diamond magnetometer with nanoscale resolution. *Nature Physics*, 4:810–816, 2008.

[16] F. Dolde, H. Fedder, M. W. Doherty, T. Nbauer, F. Rempp, G. Balasubramanian, T. Wolf, F. Reinhard, L. C. L. Hollenberg, F. Jelezko, and J. Wrachtrup. Electric-field sensing using single diamond spins. *Nature Physics*, 7:459–463, 2011.

[17] M. S. Grinolds, S. Hong, P. Maletinsky, L. Luan, M. D. Lukin, R. L. Walsworth, and A. Yacoby. Nanoscale magnetic imaging of a single electron spin under ambient conditions. *Nature Physics*, 9:215, 2013.

[18] D. Le Sage, K. Arai, D. R. Glenn, S. J. DeVience, L. M. Pham, L. Rahn-Lee, M. D. Lukin, A. Yacoby, A. Komeili, and R. L. Walsworth. Optical magnetic imaging of living cells. *Nature*, 496:486–489, 2013.

[19] L. Jiang, J. S. Hodges, J. R. Maze, P. Maurer, J. M. Taylor, D. G. Cory, P. R. Hemmer, R. L. Walsworth, A. Yacoby, A. S. Zibrov, and M. D. Lukin. Repetitive readout of a single electronic spin via quantum logic with nuclear spin ancillae. *Science*, 326:267, 2009.

[20] L. M. Pham, N. Bar-Gill, D. Le Sage, C. Belthangady, A. Stacey, M. Markham, D. J. Twitchen, M. D. Lukin, and R. L. Walsworth. Enhanced metrology using preferential orientation of nitrogen-vacancy centers in diamond. *Physical Review B*, 86:121202(R), 2012.

[21] G. Kucsko, P. C. Maurer, N. Y. Yao, M. Kubo, H. J. Noh, P. K. Lo, H. Park, and M. D. Lukin. Nanometre-scale thermometry in a living cell. *Nature*, 500:54–58, 2013.

[22] P. Neumann, N. Mizuochi, F. Rempp, P. Hemmer, H. Watanabe, S. Yamasaki, V. Jacques, T. Gaebel, F. Jelezko, and J. Wrachtrup. Multipartite entanglement among single spins in diamond. *Science*, 320(5881):1326–1329, 2008.

[23] F. Dolde, I. Jakobi, B. Naydenov, N. Zhao, S. Pezzagna, C. Trautmann, J. Meijer, P. Neumann, F. Jelezko, and J. Wrachtrup. Room-temperature entanglement between single defect spins in diamond. *Nature Physics*, 9:139143, 2013.

[24] B. Hensen, H. Bernien, A. E. Drau, A. Reiserer, N. Kalb, M. S. Blok, J. Ruitenberg, R. F. L. Vermeulen, R. N. Schouten, C. Abelln, W. Amaya, V. Pruneri, M. W. Mitchell, M. Markham, D. J. Twitchen, D. Elkouss, S. Wehner, T. H. Taminiau, and R. Hanson. Loophole-free bell inequality violation using electron spins separated by 1.3 kilometres. *Nature*, 526:682686, 2015.

[25] G. Davies and M. F. Hamer. Optical studies of the 1.945 ev vibronic band in diamond. *Proceedings of the Royal Society of London A*, 348(1653):285, 1976.

[26] D. J. Twitchen, J. M. Baker, M. E. Newton, and K. Johnston. Identification of cobalt on a lattice site in diamond. *Physical Review B*, 61:9, 2000.

[27] A. M. Edmonds, M. E. Newton, P. M. Martineau, D. J. Twitchen, and S. D. Williams. Electron paramagnetic resonance studies of silicon-related defects in diamond. *Physical Review B*, 77:245205, 2008.

[28] V. M. Acosta, E. Bauch, M. P. Ledbetter, A. Waxman, L.-S. Bouchard, and D. Budker. Temperature dependence of the nitrogen-vacancy magnetic resonance in diamond. *Physical Review Letters*, 104(7):070801, 2010.

[29] L. Robledo, H. Bernien, T. van der Sar, and R. Hanson. Spin dynamics in the optical cycle of single nitrogen-vacancy centres in diamond. *New Journal of Physics*, 13(2):025013, 2011.

[30] E. Togan, Y. Chu, A. S. Trifonov, L. Jiang, J. Maze, L. Childress, M. V. G. Dutt, A. S. Srensen, P. R. Hemmer, A. S. Zibrov, and M. D. Lukin. Quantum entanglement between an optical photon and a solid-state spin qubit. *Nature*, 466(7307):730734, 2010.

[31] L. Childress. *Coherent Manipulation of Single Quantum Systems in the Solid State*. PhD thesis, Harvard University, 2006.

[32] L. M. Pham. *Magnetic Field Sensing with Nitrogen-Vacancy Color Centers in Diamond*. PhD thesis, Harvard University, 2013.

[33] J.A. Weil and J.R. Bolton. *Electron Paramagnetic Resonance: Elementary Theory and Practical Applications*, chapter 6.2.1. Wiley, 2007.

[34] S. Felton, A. M. Edmonds, M. E. Newton, P. M. Martineau, D. Fisher, D. J. Twitchen, and J. M. Baker. Hyperfine interaction in the ground state of the negatively charged nitrogen vacancy center in diamond. *Physical Review B*, 79:075203, 2009.

[35] C. S. Shin, M. C. Butler, H-J. Wang, C. E. Avalos, S. J. Seltzer, R-B. Liu, A. Pines, and V. S. Bajaj. Optically detected nuclear quadrupolar interaction of ^{1}4n in nitrogen-vacancy centers in diamond. *Physical Review B*, 89:205202, 2014.

[36] S. Prawer and I. Aharonovich. *Quantum Information Processing with Diamond: Principles and Applications*, chapter 11.2.2. Elsevier Science, 2014.

[37] R. L. Walsworth, D. R. Glenn, and D. B. Bucher. Synchronized-readout for narrowband detection of time-varying electromagnetic fields using solid state spins, 2016. Application Number: 62/341,497.

[38] H. J. Mamin, M. Kim, M. H. Sherwood, C. T. Rettner, K. Ohno, D. D. Awschalom, and D. Rugar. Nanoscale nuclear magnetic resonance with a nitrogen-vacancy spin sensor. *Science*, 339(6119):557–560, 2013.

[39] T. Staudacher, F. Shi, S. Pezzagna, J. Meijer, J. Du, C. A. Meriles, F. Reinhard, and J. Wrachtrup. Nuclear magnetic resonance spectroscopy on a (5-nanometer)^3 sample volume. *Science*, 339(6119):561–563, 2013.

[40] S. J. DeViencea, L. M. Pham, I. Lovchinsky, A. O. Sushkov, N. Bar-Gill, C. Belthangady, F. Casola, M. Corbett, H. Zhang, M. Lukin, H. Park, A. Yacoby, and R. L. Walsworth. Nanoscale nmr spectroscopy and imaging of multiple nuclear species. *Nature Nanotechnology*, 10:129–134, 2015.

[41] P. C. Maurer, G. Kucsko, C. Latta, L. Jiang, N. Y. Yao, S. D. Bennett, F. Pastawski, D. Hunger, N. Chisholm, M. Markham, D. J. Twitchen, J. I. Cirac, and M. D. Lukin. Room-temperature quantum bit memory exceeding one second. *Science*, 336(6086):1283–1286, 2012.

[42] S. Zaiser, T. Rendler, I. Jakobi, T. Wolf, S. Lee, S. Wagner, V. Bergholm, T. Schulte-Herbrggen, P. Neumann, and J. Wrachtrup. Enhancing quantum sensing sensitivity by a quantum memory. *Nature Communications*, 7:12279, 2016.

[43] T. Rosskopf, J. Zopes, J. M. Boss, and C. L. Degen. A quantum spectrum analyzer enhanced by a nuclear spin memory. *npj Quantum Information*, 3:33, 2017.

[44] N. Aslam, M. Pfender, P. Neumann, R. Reuter, A. Zappe, F. Oliveira, A. Denisenko, H. Sumiya, S. Onoda, J. Isoya, and J. Wrachtrup. Nanoscale nuclear magnetic resonance with chemical resolution. *Science*, 10:1126, 2017.

[45] H. Y. Carr and E. M. Purcell. Effects of diffusion on free precession in nuclear magnetic resonance experiments. *Physical Review*, 94:630, 1954.

[46] S. Meiboom and D. Gill. Modified spinecho method for measuring nuclear relaxation times. *Review of Scientific Instruments*, 29:688, 1958.

[47] S. M. Alessio. *Digital signal processing and spectral analysis for scientists: concepts and applications.* Springer, 2016.

[48] M. W. Doherty, N. B. Manson, P. Delaney, F. Jelezko, J. Wrachtrup, and L. C. L. Hollenberg. The nitrogen-vacancy colour centre in diamond. *Physics Reports*, 528(1):1–45, 2013.

[49] N. Bloembergen, E. M. Purcell, and R. V. Pound. Relaxation effects in nuclear magnetic resonance absorption. *Physics Review*, 73:679, 1948.

[50] D. L. Olson, T. L. Peck, A. G. Webb, R. L. Magin, and J. V. Sweedler. High-resolution microcoil ^{1}h-nmr for mass-limited, nanoliter-volume samples. *Science*, 270:1967–1970, 1995.

[51] R. M. Fratila and A. H. Velders. Small-volume nuclear magnetic resonance spectroscopy. *Annual Review of Analytical Chemistry*, 4:227–249, 2011.

[52] H. Ryan, A. Smith, and M. Utz. Structural shimming for high-resolution nuclear magnetic resonance spectroscopy in lab-on-a-chip devices. *Lab Chip*, 14:1678, 2014.

[53] A. Laraoui, F. Dolde, C. Burk, F. Reinhard, J. Wrachtrup, and C. A. Meriles. High-resolution correlation spectroscopy of 13c spins near a nitrogen-vacancy centre in diamond. *Nature Communications*, 4:1651, 2013.

[54] B. L. Green, M. W. Dale, M. E. Newton, and D. Fisher. Electron paramagnetic resonance of the n_2v defect in ^{15}n-doped synthetic diamond. *Physical Review B*, 92:165204, 2015.

[55] B. L. Green, B. G. Breeze, and M. E. Newton. Electron paramagnetic resonance and photochromism of n_3v^0 in diamond. *Journal of Physics: Condensed Matter*, 29:22, 2017.

[56] K. Arai, C. Belthangady, H. Zhang, N. Bar-Gill, S. J. DeVience, P. Cappellaro, A. Yacoby, and R. L. Walsworth. Fourier magnetic imaging with nanoscale resolution and compressed sensing speed-up using electronic spins in diamond. *Nature Nanotechnology*, 10:859–864, 2015.

[57] H. Zhang, K. Arai, C. Belthangady, J.-C. Jaskula, and R. L. Walsworth. Selective addressing of solid-state spins at the nanoscale via magnetic resonance frequency encoding. *npj Quantum Information*, 3:31, 2017.

[58] R. M. Dickson, D. J. Norris, Y.-L. Tzeng, and W. E. Moerner. Three-dimensional imaging of single molecules solvated in pores of poly(acrylamide) gels. *Science*, 274:966–968, 1996.

[59] M. J. Shon and A. E. Cohen. Mass action at the single-molecule level. *Journal of the American Chemical Society*, 134:14618–14623, 2012.

[60] G. Kucsko, S. Choi, J. Choi, P. C. Maurer, H. Zhou, R. Landig, H. Sumiya, S. Onoda, J. Isoya, F. Jelezko, E. Demler, N. Y. Yao, and M. D. Lukin. Critical thermalization of a disordered dipolar spin system in diamond. *arXiv*, 1609:08216v2, 2017.

[61] S. Choi, J. Choi, R. Landig, G. Kucsko, H. Zhou, J. Isoya, F. Jelezko, S. Onoda, H. Sumiya, V. Khemani, C. Keyserlingk, N. Y. Yao, E. Demler, and M. D. Lukin. Observation of discrete time-crystalline order in a disordered dipolar many-body system. *Nature*, 543:221225, 2017.

[62] S. Inouye, M. R. Andrews, J. Stenger, H.-J. Miesner, D. M. Stamper-Kurn, and W. Ketterle. Observation of feshbach resonances in a boseeinstein condensate. *Nature*, 392:151–154, 1998.

[63] C. Chin, R. Grimm, P. Julienne, and E. Tiesinga. Feshbach resonances in ultracold gases. *Review of Modern Physics*, 82:1225, 2010.

[64] A. Abragam. *The Principles of Nuclear Magnetism*. International series of monographs on physics. Clarendon Press, 1961.

[65] J. N. Mundy. *Solid State : Nuclear Methods*, volume 21 of *Methods of Experimental Physics*, chapter 6.2.1.1. Academic Press, 1983.

[66] J. Li, M.P. Silveri, K.S. Kumar, J.-M. Pirkkalainen, A. Vepsalainen, W.C. Chien, J. Tuorila, M.A. Sillanpaa, P.J. Hakonen, E.V. Thuneberg, and G.S. Paraoanu. Motional averaging in a superconducting qubit. *Nature Communications*, 4:1420, 2013.

[67] T. Gaebel, M. Domhan, I. Popa, C. Wittmann, P. Neumann, F. Jelezko, J. R. Rabeau, N. Stavrias, A. D. Greentree, S. Prawer, J. Meijer, J. Twamley, P. R. Hemmer, and J. Wrachtrup. Room-temperature coherent coupling of single spins in diamond. *Nature Physics*, 2:408–413, 2006.

[68] B. A. Myers, A. Das, M. C. Dartiailh, K. Ohno, D. D. Awschalom, and A. C. Bleszynski Jayich. Probing surface noise with depth-calibrated spins in diamond. *Physical Review Letters*, 113:027602, 2014.

[69] L. M. Pham, S. J. DeVience, F. Casola, I. Lovchinsky, A. O. Sushkov, E. Bersin, J. Lee, E. Urbach, P. Cappellaro, H. Park, A. Yacoby, M. Lukin, and R. L. Walsworth. Nmr technique for determining the depth of shallow nitrogen-vacancy centers in diamond. *Physical Review B*, 93:045425, 2016.

[70] S. Choi, N. Y. Yao, and M. D. Lukin. Dynamical engineering of interactions in qudit ensembles. *Physical Review Letters*, 119:183603, 2017.

[71] G. de Lange, T. van der Sar, M. Blok, Z. Wang, V. Dobrovitski, and R. Hanson. Controlling the quantum dynamics of a mesoscopic spin bath in diamond. *Scientific Reports*, 2:382, 2012.

[72] E. Bauch, C. A. Hart, J. M. Schloss, M. J. Turner, J. F. Barry, P. Kehayias, and R. L. Walsworth. Ultralong dephasing times in solid-state spin ensembles via quantum control. *arXiv*, 1801, 2018.

[73] M. V. Berry. Quantal phase factors accompanying adiabatic changes. *Proceedings of the Royal Society A*, 392:45–57, 1984.

[74] F. Wilczek and A. Zee. Appearance of gauge structure in simple dynamical systems. *Physical Review Letters*, 52:21112114, 1984.

[75] J. H. Hannay. Angle variable holonomy in adiabatic excursion of an integrable hamiltonian. *Journal of Physics A: Mathematical and General*, 18:22130, 1985.

[76] D. J. Thouless, M. Kohmoto, M. P. Nightingale, and M. den Nijs. Quantized hall conductance in a two-dimensional periodic potential. *Physical Review Letters*, 49:405408, 1982.

[77] F. D. M. Haldane. Model for a quantum hall effect without landau levels: condensed-matter realization of the parity anomaly. *Physical Review Letters*, 61:420152018, 1988.

[78] Y. Zhang, Y.-W. Tan, H. L. Stormer, and P. Kim. Experimental observation of the quantum hall effect and berrys phase in graphene. *Nature*, 438:201, 2005.

[79] A. Tomita and R. Y. Chiao. Observation of berrys topological phase by use of an optical fiber. *Physical Review Letters*, 57:937, 1986.

[80] D. Suter, K. T. Mueller, and A. Pines. Study of the aharonov-anandan quantum phase by nmr interferometry. *Physical Review Letters*, 60:1218, 1988.

[81] P. J. Leek, J. M. Fink, A. Blais, R. Bianchetti, M. Goppl, J. M. Gambetta, D. I. Schuster, L. Frunzio, R. J. Schoelkopf, and A. Wallraff. Observation of berrys phase in a solid-state qubit. *Science*, 318:1889–1892, 2007.

[82] G. De Chiara and G. M. Palma. Berry phase for a spin 1/2 particle in a classical fluctuating field. *Physical Review Letters*, 91:090404, 2003.

[83] S. Filipp, J. Klepp, Y. Hasegawa, C. Plonka-Spehr, U. Schmidt, P. Geltenbort, and H. Rauch. Experimental demonstration of the stability of berrys phase for a spin-1/2 particle. *Physical Review Letters*, 102:030404, 2009.

[84] Y.-J. Lin, R. L. Compton, K. Jimnez-Garca, J. V. Porto, and I. B. Spielman. Synthetic magnetic fields for ultracold neutral atoms. *Nature*, 462:628632, 2009.

[85] G. Jotzu, M. Messer, R. Desbuquois, M. Lebrat, T. Uehlinger, D. Greif, and T. Esslinger. Experimental realization of the topological haldane model with ultracold fermions. *Nature*, 515:237240, 2014.

[86] P. Zanardi and M. Rosetti. Holonomic quantum computation. *Physics Letters A*, 264:94, 1999.

[87] J. A. Jones, V. Vedral, A. Ekert, and G. Castagnoli. Geometric quantum computation using nuclear magnetic resonance. *Nature*, 403:869, 2000.

[88] C. Zu, W.-B. Wang, L. He, W.-G. Zhang, C.-Y. Dai, F. Wang, and L.-M. Duan. Experimental realization of universal geometric quantum gates with solid-state spins. *Nature*, 514:7275, 2014.

[89] N. Bar-Gill, L.M. Pham, C. Belthangady, D. Le Sage, P. Cappellaro, J.R. Maze, M.D. Lukin, A. Yacoby, and R. Walsworth. Suppression of spin-bath dynamics for improved coherence of multi-spin-qubit systems. *Nature Communications*, 3:858, 2012.

[90] N. M. Nusran, M. U. Momeen, and M. V. G. Dutt. High-dynamic-range magnetometry with a single electronic spin in diamond. *Nature Nanotechnology*, 7:109–113, 2012.

[91] C. Bonato, M. S. Blok, H. T. Dinani, D. W. Berry, M. L. Markham, D. J. Twitchen, and R. Hanson. Optimized quantum sensing with a single electron spin using real-time adaptive measurements. *Nature Nanotechnology*, 11:247252, 2016.

[92] J. J . Bollinger, W. M. Itano, D. J. Wineland, and D. J. Heinzen. Optimal frequency measurements with maximally correlated states. *Physical Review A*, 54:R4649(R), 1996.

[93] V. Giovannetti, S. Lloyd, and L. Maccone. Quantum-enhanced measurements: beating the standard quantum limit. *Science*, 306:1330–1336, 2004.

[94] R. C. Weast. *CRC Handbook of Chemistry and Physics*, chapter 6.2.1.1. CRC Press, 1984.

[95] G. Balasubramanian, I. Y. Chan, R. Kolesov, M. Al-Hmoud, J. Tisler, C. Shin, C. Kim, A. Wojcik, P. R. Hemmer, A. Krueger, T. Hanke, A. Leitenstorfer, R. Bratschitsch, F. Jelezko, and J. Wrachtrup. Nanoscale imaging magnetometry with diamond spins under ambient conditions. *Nature*, 455:648651, 2008.

[96] J. P. Tetienne, T. Hingant, J. V. Kim, L. H. Diez, J. P. Adam, K. Garcia, J. F. Roch, S. Rohart, A. Thiaville, D. Ravelosona, and V. Jacques. Nanoscale imaging and control of domain-wall hopping with a nitrogen-vacancy center microscope. *Science*, 344:1366–1369, 2014.

[97] C. Du, T. van der Sar, T. X. Zhou, P. Upadhyaya, F. Casola, H. Zhang, M. C. Onbasli, C. A. Ross, R. L. Walsworth Y. Tserkovnyak, and A. Yacoby. Control and local measurement of the spin chemical potential in a magnetic insulator. *Science*, 357(6347):195–198, 2017.

[98] D. R. Glenn, K. Lee, H. Park, R. Weissleder, A. Yacoby, M. D Lukin, H. Lee, R. L. Walsworth, and C. B. Connolly. Single-cell magnetic imaging using a quantum diamond microscope. *Nature Methods*, 12:736–738, 2015.

[99] J. F. Barry, M. J. Turner, J. M. Schloss, D. R. Glenn, Y. Song, M. D. Lukin, H. Park, and R. L. Walsworth. Optical magnetic detection of single-neuron action potentials using quantum defects in diamond. *PNAS*, 113:14133–14138, 2016.

[100] R. R. Fu, B. P. Weiss, E. A. Lima, R. J. Harrison, X. Bai, S. J. Desch, D. S. Ebel, C. Suavet, H. Wang, D. Glenn, D. Le Sage, T. Kasama, R. L. Walsworth, and A. T. Kuan. Solar nebula magnetic fields recorded in the semarkona meteorite. *Science*, 346(6213):1089–1092, 2014.

[101] D. R. Glenn, R. R. Fu, P. Kehayias, D. Le Sage, E. A. Lima, B. P. Weiss, and R. L. Walsworth. Micrometer-scale magnetic imaging of geological samples using a quantum diamond microscope. *Geochemistry, Geophysics, Geosystems*, 18:doi:10.1002/2017GC006946, 2017.

[102] M. Knig, S. Wiedmann, C. Brne, A. Roth, H. Buhmann, L. W. Molenkamp, X.-L. Qi, and S.-C. Zhang. Micrometer-scale magnetic imaging of geological samples using a quantum diamond microscope. *Science*, 318:766, 2007.

[103] L. Fu, C. L. Kane, and E. J. Mele. Topological insulators in three dimensions. *Physical Review Letters*, 98:106803, 2007.

[104] Y. Hatsugai. Chern number and edge states in the integer quantum hall effect. *Physical Review Letters*, 71:3697, 1993.

[105] Q. Niu, D. J. Thouless, and Y. Wu. Quantized hall conductance as a topological invariant. *Physical Review B*, 31:3372, 1985.

[106] V. Gritsev and A. Polkovnikov. Dynamical quantum hall effect in the parameter space. *PNAS*, 109:6457, 2012.

[107] M. D. Schroer, M. H. Kolodrubetz, W. F. Kindel, M. Sandberg, J. Gao, M. R. Vissers, D. P. Pappas, A. Polkovnikov, and K. W. Lehnert. Measuring a topological transition in an artificial spin-1=2 system. *Physical Review Letters*, 113:050402, 2014.

[108] P. Roushan, C. Neill, Y. Chen, M. Kolodrubetz, C. Quintana, N. Leung, M. Fang, R. Barends, B. Campbell, Z. Chen, B. Chiaro, A. Dunsworth, E. Jeffrey, J. Kelly, A. Megrant, J. Mutus, P. J. J. OMalley, D. Sank, A. Vainsencher, J. Wenner, T. White, A. Polkovnikov, A. N. Cleland, and J. M. Martinis. Observation of topological transitions in interacting quantum circuits. *Nature*, 515:241–244, 2014.

[109] S. s. Chern. Characteristic classes of hermitian manifolds. *Annals of Mathematics*, 47:85, 1946.

[110] L. Landau. Zur theorie der energieubertragung. ii. *Physikalische Zeitschrift der Sowjetunion*, 2:46–51, 1932.

[111] C. Zener. Non-adiabatic crossing of energy levels. *Proceedings of the Royal Society of London A*, 137(6):696–702, 1932.

[112] F. Casola, T. van der Sar, , and A. Yacoby. Probing condensed matter physics with magnetometry based on nitrogen-vacancy centres in diamond. *Nature Review Materials*, 3:17088, 2018.

[113] H. Clevenson, M. E. Trusheim, C. Teale, T. Schroder, D. Braje, and D. Englund. Broadband magnetometry and temperature sensing with a light-trapping diamond waveguide. *Nature Physics*, 11:393–397, 2015.

[114] P. Kehayias, A. Jarmola, N. Mosavian, I. Fescenko, F. M. Benito, A. Laraoui, J. Smits, L. Bougas, D. Budker, A. Neumann, S. R. J. Brueck, and V. M. Acosta. Solution nuclear magnetic resonance spectroscopy on a nanostructured diamond chip. *Nature Communications*, 8:188, 2017.

[115] P. Cappellaro and M. D. Lukin. Quantum correlation in disordered spin systems: Applications to magnetic sensing. *Physical Review A*, 80:032311, 2009.

[116] S. Choi, N. Y. Yao, and M. D. Lukin. Quantum metrology based on strongly correlated matter. *arXiv*, 1801:00042, 2017.

[117] P. Weinberg, M. Bukov, L. D'Alessio, A. Polkovnikov, S. Vajna, and M. Kolodrubetz. Adiabatic perturbation theory and geometry of periodically-driven systems. *Physics Reports*, 688:1–36, 2017.

[118] D. J. Thouless. Quantization of particle transport. *Physical Review B*, 27:6083, 1983.

[119] T. Schroder, M. E. Trusheim, M. Walsh, L. Li, J. Zheng, M. Schukraft, A. Sipahigil, R. E. Evans, D. D. Sukachev, C. T. Nguyen, J. L. Pacheco, R. M. Camacho, E. S. Bielejec, M. D. Lukin, and D. Englund. Scalable focused ion beam creation of nearly lifetime-limited single quantum emitters in diamond nanostructures. *Nature Communications*, 8:15376, 2017.

[120] Y-C. Chen, P. S. Salter, S. Knauer, L. Weng, A. C. Frangeskou, C. J. Stephen, S. N. Ishmael, P. R. Dolan, S. Johnson, B. L. Green, G. W. Morley, M. E. Newton, J. G. Rarity, M. J. Booth, and J. M. Smith. Laser writing of coherent colour centres in diamond. *Nature Photonics*, 11:77–80, 2017.

[121] A.O. Sushkov, I. Lovchinsky, N. Chisholm, R.L. Walsworth, H. Park, and M.D. Lukin. Magnetic resonance detection of individual proton spins using quantum reporters. *Physical Review Letters*, 113:197601, 2014.